Università degli Studi di Padova
Dipartimento di Fisica ed Astronomia "G. Galilei"

Tesi di Laurea Magistrale in Fisica

Nano-Hole Arrays for plasmonic biosensors

Laureando:
Ionuț Gabriel Balașa

Relatore:
Prof. Giovanni Mattei

Anno Accademico 2014/2015

To my family

Contents

Introduction

In the last years, the study of the size-dependent properties of materials at nanometric scale attracted a lot of interest due to the innovative properties that they present, that are optical, magnetic, catalytic and mechanical properties. The research at nanometric scale became important in many sectors as nanophotonics, data-storage [1] and telecommunication, which need smaller, faster and more efficient devices [2].

Photonics is the discipline that studies the production, propagation and detection of electromagnetic radiation in the NIR-Vis-NUV range, while nanophotonics focuses on the behaviour and the interaction of the radiation at nanometric scale. In this framework, one of the most important fields is plasmonics which studies the interaction of electromagnetic radiation with the nanostructures, mainly made of noble metals, in order to control the light on scales below the $\lambda/2$ diffraction limit.

In this context, due to their unusual optical properties, nanomaterials gained interest in medical applications. Medical research and healthcare need innovative devices in the diagnostic field that allow to reveal very low concentrations of a specific compound, called analyte, and nanomaterials are very promising for the development of such biosensors, able to reveal concentrations down to the picomolar range [3].

Plasmonics research focused on the study of the optical properties by varying dimensions, morphology and composition of nanostructures in order to obtain best performances in the biosensing field, and this also represents the main purpose of the present work.

The physical phenomenon that gives innovative optical properties to noble-metal nanostructures is the excitation Surface Plasmon Polaritons (SPP). It consists in an electromagnetic wave which travels at the interface between a nanostructured metal and a dielectric. SPP involves on one side the coherent oscillation of the conduction electrons at the interface inside the metal, and on the other side the propagation of an electromagnetic wave along the surface, inside the dielectric [4].

The transduction mechanism relies on the Surface Plasmon Resonace (SPR) that represents the condition which yields the SPP excitation. Since the spectral position of the SPR depends on the dielectric medium at the interface, the binding of an analyte with prevously deposited suitable molecular receptors on the nanostructure is revealed as a change in the SPR condition due to the different dielectric properties of the environment (air or water) and the biological compound, which can be considered as a few nanometers thick dielectric layer on the plasmonic nanostructures. The presence of receptors that bind only

a selected analyte allows a high-specificity. Moreover, the enhanced sensitivity due to the plasmonic resonances can added a further advantage. and lable-free biosensing.

In the present work, Nano Holes Arrays (NHA) are designed and synthesized for biosensing purposes. They consist in a thin metallic film ($50 - 100$ nm) patterned with a hexagonal array of circular holes. Such a metallic nanostructure presents a remarkable optical property, the Extraordinary Optical Transmission (EOT), first reported by Ebbesen in 1998 [5]. Illuminating the NHA and considering the transmittance spectrum, it can be observed that, in corrispondence of specific wavelengths, the intensity of the transmitted light through the NHA is greater than the intensity that would pass through a single hole with an area equivalent to the sum of all the nanohole apertures.

Such nanostructures are produced by Nano Sphere Litography (NSL) [6], that is a cost-effective technique which allows to finely tune the morphology of the NHA and consists in employing a Self-Assembled Monolayer (SAM) of PolyStyrene (PS) nanospheres as a deposition mask.

By NSL low-cost biosensors can be produced and, moreover, the simple experimental setup for transmittance measurements allows a real-time sensing. Due to its many advanteges, NHA is a promising nanostructure for developing high-sensitivity biosensors with low limit of detection, that is the minimum concentration that a sensor can reveal. Moreover, such a device also fits well for miniaturization purposes as Lab on a chip devices [7].

NSL process is studied and optimized in this work in order to obtain a reproducible protocol for the production of large-area well ordered metallic NHA and the best morphological parameters are investigated both experimentally and by numerical simulation to get the optimal optical properties.

Sensing performances of the NHA are tested by evaluating its sensitivity to the change of the dielectric medium at the interface. For this purpose, in addition to experimental tests, simulations are carried out employing COMSOL Multiphysics® software. Biosensing tests are done functionalizing NHA with biological receptors that bind with a selected analyte. Specifically, we used a model system exploiting the interaction between Biotin and Streptavidin molecules, which have a high affinity, Biotin is used as a receptor and different concentrations of Streptavidin as analyte. Thus, the output signal at different concentration of analytes is investigated.

The present thesis is organized as follows:

Chapter 1 A theoretical description of the interaction between electromagnetic radiation and metallic nanostructures is presented.

Chapter 2 The fabrication protocol by NSL of metallic NHA is described.

Chapter 3 Different ways for employing nanostructures as optical biosensors are presented.

Chapter 4 Numerical simulations are carried out to design the optical properties and the sensing performances of the NHA.

Chapter 5 The produced NHA are characterized optically, by measuring transmittance spectra, and morphologically by AFM and SEM.

Chapter 6 Results from the biosensing tests are, finally, reported.

Chapter 1

Metallic Nanostructures and Electromagnetic Radiation

1.1 Interaction of electromagnetic radiation with matter

Plasmonics is a field of nanophotonics which studies how electromagnetic (EM) radiation can be confined within dimensions smaller than its wavelength. Interaction of electromagnetic fields with metals, which highly depends on frequency and electronic structure of the metal, can be described by Maxwell's equations, and optical properties of metals can be understood without reporting to quantum mechanics.

For low frequency radiation, as microwave or far-infrared, metals are very reflective and electromagnetic waves do not propagate through them. Only a negligible fraction of radiation penetrates into the metal to a depth called *skin depth*.

As frequency rises towards the visible part of the EM spectrum, field penetration in metals increases, dissipation becomes considerable and it results difficult to scale from low frequencies how metal works in visible range.

Finally, at ultraviolet frequencies (and in particular, below a characteristic frequency called plasma frequency, as it will be shown in the following), a metal acts as a dielectric and allows propagation of EM radiation. Refractive index and absorption depend on electronic band structure. For example, while alkali metals become transparent to UV radiation, noble metals, as gold and silver, have strong adsorption in UV range due to interband transition.

Optical and dispersive properties are described in a classical way via a *complex dielectric function* $\epsilon(\omega)$ which can be measured experimentally or calculated theoretically, using simple models as the *Drude model*.

The startpoint for the study of electromagnetic response of metals is given by the Maxwell's macroscopic equations

$$\nabla \cdot \mathbf{D} = \rho_{ext} \tag{1.1a}$$

$$\nabla \cdot \mathbf{B} = 0 \tag{1.1b}$$

$$\nabla \times \mathbf{E} = -\frac{\partial \mathbf{B}}{\partial t} \tag{1.1c}$$

$$\nabla \times \mathbf{H} = \mathbf{J_{ext}} + \frac{\partial \mathbf{D}}{\partial t} \tag{1.1d}$$

which link the four macroscopic fields, electric field $\mathbf{E}$, magnetic field $\mathbf{B}$, dielectric displacement $\mathbf{D}$ and magnetic induction $\mathbf{H}$, with the external charge density ρ_{ext} and external current density $\mathbf{J_{ext}}$. Two more fields are introduced, polarization $\mathbf{P}$ and magnetization $\mathbf{M}$, and they are linked to the others by

$$\mathbf{D} = \epsilon_0 \mathbf{E} + \mathbf{P} \tag{1.2a}$$

$$\mathbf{H} = \frac{1}{\mu_0}\mathbf{B} - \mathbf{M} \tag{1.2b}$$

Since only non magnetic media will be studied, the term $\mathbf{M}$ can be neglected and only polarization effects will be considered. As polarization $\mathbf{P}$ is related to internal charge density ρ_{int} by $\nabla \cdot \mathbf{P} = -\rho_{int}$, charge conservation $\nabla \cdot \mathbf{J} = -\frac{\partial \rho_{int}}{\partial t}$ imply that

$$\mathbf{J} = \frac{\partial \mathbf{P}}{\partial t} \tag{1.3}$$

At this point, if the medium is linear, isotropic and nonmagnetic, $\mathbf{D}$ and $\mathbf{H}$ are proportional to $\mathbf{E}$ and $\mathbf{B}$. Equations 1.2 can be expressed using relative electrical permittivity ϵ and magnetic permeability μ, which for nonmagnetic media is 1:

$$\mathbf{D} = \epsilon_0 \epsilon \mathbf{E} \tag{1.4a}$$

$$\mathbf{B} = \mu_0 \mu \mathbf{H} \tag{1.4b}$$

Moreover, for the same medium, there is another linear relationship, between internal current density $\mathbf{J}$ and electric field $\mathbf{E}$ where the conductivity σ is introduced

$$\mathbf{J} = \sigma \mathbf{E} \tag{1.5}$$

However equations 1.4a and 1.5 are correct for linear media that do not exhibit temporal or spatial dispersion. These assumptions are not satisfied by metals whose response strongly depends on frequency. Taking account of the non-locality in time and space linear $(\mathbf{r}, t)$ relationships are generalized as

$$\mathbf{D}(\mathbf{r}, t) = \epsilon_0 \int dt' \mathbf{dr}' \epsilon(\mathbf{r} - \mathbf{r}', t - t') \mathbf{E}(\mathbf{r}', t') \tag{1.6a}$$

$$\mathbf{J}(\mathbf{r}, t) = \int dt' \mathbf{dr}' \sigma(\mathbf{r} - \mathbf{r}', t - t') \mathbf{E}(\mathbf{r}', t') \tag{1.6b}$$

Equations 1.6 are simplified by taking their Fourier transformed in $(\mathbf{k}, \omega)$ domain, converting convolution to multiplication:

$$\mathbf{D}(\mathbf{k}, \omega) = \epsilon_0 \epsilon(\mathbf{k}, \omega) \mathbf{E}(\mathbf{k}, \omega) \tag{1.7a}$$

$$\mathbf{J}(\mathbf{k},\omega) = \sigma(\mathbf{k},\omega)\mathbf{E}(\mathbf{k},\omega). \tag{1.7b}$$

Using equations 1.2a, 1.3 and 1.7 a relationship is found between conductivity σ and relative permittivity ϵ (from now on called *dielectric function*):

$$\epsilon(\mathbf{k},\omega) = 1 + \frac{i\sigma(\mathbf{k},\omega)}{\epsilon_0\omega}. \tag{1.8}$$

Due to this intimate relationship electromagnetic phenomena can be described using either quantity. Historically, conductivity is preferably used at low frequencies while dielectric function is used at optical frequencies.

In this work, properties in NIR-Vis-UV range will be studied so from now on only dielectric function ϵ will be considered. In the next section, a simple model to calculate ϵ will be introduced.

In eq. 1.7 further simplification is done considering spatially local interaction. This is valid as long as the wavelength λ of the EM radiation is larger than other relevant dimensions, as unit cell size and mean free path of electrons. This condition is fullfiled up to the ultraviolet frequencies ($\lambda \lesssim 100nm$). Under this assumption dielectric function becomes $\epsilon(\mathbf{k} = \mathbf{0}, \omega) = \epsilon(\omega)$

In general ϵ is a complex function of the angular frequency ω, which is a real value, and can be expressed as $\epsilon(\omega) = \epsilon_1(\omega) + i\epsilon_2(\omega)$. However, via reflectivity measurements, complex refractive index $\tilde{n}(\omega) = n(\omega) + ik(\omega)$ of the medium can be determined. Taking into account that $\tilde{n}(\omega)$ is defined by

$$\tilde{n}(\omega) = \sqrt{\epsilon(\omega)}, \tag{1.9}$$

finally the dielectric function can be calculated.

The complex part of $\tilde{n}(\omega)$, k, is called the *extinction coefficient* and determines the optical adsorption of EM radiation propagating through a medium. It is proportional to the absorption coefficient α of Beer's exponential attenuation law in a medium ($I(x) = I_0 e^{-\alpha x}$) by

$$\alpha(\omega) = \frac{2k(\omega)\omega}{c} \tag{1.10}$$

1.1.1 Drude model

As pointed out previously, the dielectric function $\epsilon(\omega)$ tells most of the information about interaction between metal and EM radiation. A simple model to calculate ϵ for the frequency range of interest for the present work, i.e., VIS and NIR portion of the spectrum, is the Drude model of free electron gas. Here, a density n of free electrons is supposed to move against a fixed lattice of positive ions. Since electrons are supposed to be free particles, details of lattice potential and electron-electron interactions are neglected. Some aspects of band structure could be embedded in the electron mass by considering effective mass of the electron.

When a radiation impinges a metal, electrons move according to the external field until they collide with a positive ion. Collisions occur with a caracteristic frequency $\gamma = 1/\tau$,

where τ is the relaxation time of the free electron gas, and γ typically is of the order of 100 THz at room temperature.

Although these strong assumptions, this model gives good results in a wide range of frequencies, up to the interband transitions of the metal. While for alkali metals the model fits well up to the ultraviolet frequencies since interband transitions are in UV range, for noble metals these occur at optical wavelengths and validity is limited.

To take into account interband transitions, which lead to high absorption of radiation, contribution of bound electrons should be considered and this will be studied in section 1.1.2.

Considering only free electrons and a driving electric field $\mathbf{E}$ one obtains a simple equation of motion

$$m\ddot{\mathbf{x}} + m\gamma\dot{\mathbf{x}} = -e\mathbf{E}. \tag{1.11}$$

Assuming a harmonic dependence for the electric field $\mathbf{E}(t) = \mathbf{E_0}e^{-\imath\omega t}$, the steady state solution has the same harmonic dependence $\mathbf{x}(t) = \mathbf{x_0}e^{-\imath\omega t}$, where $\mathbf{x_0}$ is a complex value. Using $\mathbf{x}(t)$ in 1.11 leads to the solution

$$\mathbf{x}(t) = \frac{e}{m(\omega^2 + \imath\gamma\omega)}\mathbf{E}(t) \tag{1.12}$$

As $\mathbf{x}(t)$ is the displacement of a single electron, this gives a single electric dipole moment $\mathbf{p}(t) = -e\mathbf{x}(t)$. Macroscopic polarization P is obtained from contribution of all the n electrons in a unit of volume

$$\mathbf{P} = -ne\mathbf{x} = -\frac{ne^2}{m(\omega^2 + \imath\gamma\omega)}\mathbf{E} \tag{1.13}$$

Upon inserting eq. 1.13 into the eq. 1.2a the displacement vector $\mathbf{D}$ results:

$$\mathbf{D} = \epsilon_0\left(1 - \frac{\omega_p^2}{\omega^2 + \imath\gamma\omega}\right)\mathbf{E} \tag{1.14}$$

where the plasma frequency of the free electron gas $\omega_p^2 = \frac{ne^2}{\epsilon_0 m}$ was introduced. The quantity between the brackets above is the dielectric function from Drude model and separating real and imaginary part results

$$\epsilon(\omega) = 1 - \frac{\omega_p^2}{\omega^2 + \imath\gamma\omega} = \left(1 - \frac{\omega_p^2}{\omega^2 + \gamma^2}\right) + \imath\left(\frac{\omega_p^2\gamma}{\omega(\omega^2 + \gamma^2)}\right) = \epsilon_1(\omega) + \imath\epsilon_2(\omega). \tag{1.15}$$

For frequencies $\omega < \omega_p$ model gives good results. At higher frequencies such as $\omega \gg \omega_p$, equation 1.15 gives $\epsilon(\omega) \to 1$. For real metals and specially for noble metals this is false, as the d band electrons are close to the Fermi surface and they take to greater polarization. This effect can be included in equations above by adding the term $\mathbf{P}_\infty = \epsilon_0(\epsilon_\infty - 1)$ in eq. 1.2a so $\mathbf{P}$ now represents only the polarization due to free electrons. With this correction dielectric function becomes

$$\epsilon(\omega) = \left(\epsilon_\infty - \frac{\omega_p^2}{\omega^2 + \gamma^2}\right) + \imath\left(\frac{\omega_p^2\gamma}{\omega(\omega^2 + \gamma^2)}\right) \tag{1.16}$$

where $\epsilon_\infty \simeq 1 \div 10$ Validity of this model for noble metals is shown in Fig.1.1 where experimental data for real and imaginary part of $\epsilon(\omega)$ from Johnson and Christy [8] are compared with the dielectric function from Drude model (Eq.1.16). Model agrees with experimental measurements as long as interband transitions are not important. Specifically, interband transitions become relevant above 2 eV (600 nm) for copper and gold and above 4 eV (300 nm) for silver. Above those energies ϵ_2 increases and metals present high adsorption for such radiation.

Briefly, the Drudel model describes correctly optical response of metals up to the threshold of interband transitions and specifically for silver works down to UV wavelength (300 nm) while for gold and copper validity is limited down to (600 nm).

A big advantage of having an analitycal formula for dielectric function is that it can be easily included in numerical solvers for Maxwell's equations, such as the finite-difference time-domain (FDTD) scheme [9].

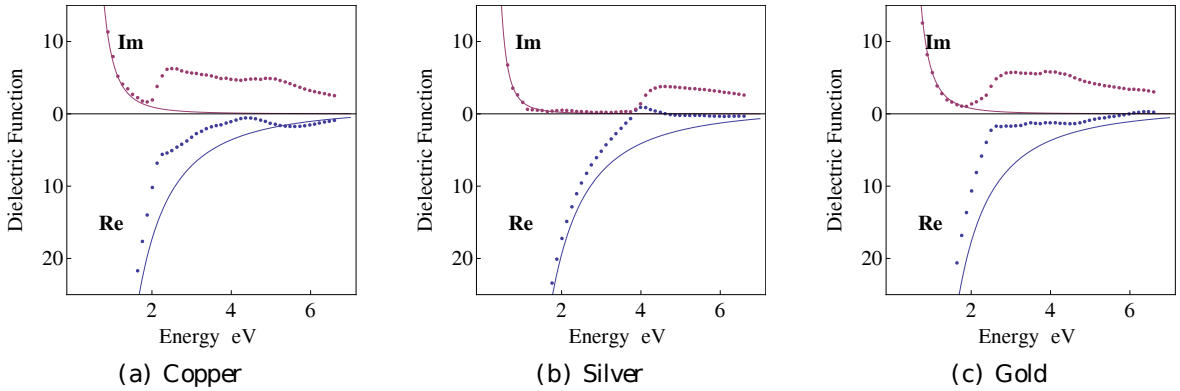

Figure 1.1: Solid line represents dielectric function $\epsilon(\omega)$ from Drude model fitted to experimental data from Johnson and Christy [8] (dotted line)

1.1.2 Lorentz-Drude model

Above the frequency thresholds incident radiation is such that bounded d electrons, below Fermi surface, are excited to higher bands yielding strong adsorption and competition between the two excitations of s and d electrons.

To take into account contribution of bounded electrons a term is added to the equation of motion 1.11:

$$m\ddot{\mathbf{x}} + m\gamma\dot{\mathbf{x}} + m\omega_0^2\mathbf{x} = -e\mathbf{E}. \tag{1.17}$$

Interband transition are therefore included considering the bounded electrons as oscillators with an own resonance frequency ω_0. This frequency corresponds to a particular interband transitions with $\hbar\omega_0$ energy. If more interband transitions are considered, there will be the same number of equations like Eq.1.11 to solve, each of them with its own resonance frequency.

	$Au(\epsilon_\infty = 1.1156, \sigma/\epsilon_0 = 1355.01s^{-1})$			$Ag(\epsilon_\infty = 1.4783, \sigma/\epsilon_0 = 3157.56s^{-1})$		
	A_i[eV]	B_i[eV^2]	C_i[eV^2]	A_i[eV]	B_i[eV^2]	C_i[eV^2]
$i=1$	$-8.577 \cdot 10^4$	$-1.156 \cdot 10^4$	$5.557 \cdot 10^7$	$-1.160 \cdot 10^5$	-3050	$3.634 \cdot 10^8$
$i=2$	-2.875	0.0	$2.079 \cdot 10^3$	-4.252	-0.8385	112.2
$i=3$	-997.6	-3090	$6.921 \cdot 10^5$	-0.4960	-13.85	1.815
$i=4$	-1.630	-4.409	26.15	-2.118	-10.23	14.31

Table 1.1: Coefficients of L4 model for Au and Ag

Each single equation leads to a Lorentz-oscillator term of the form

$$\frac{A_i}{\omega_i^2 - \omega^2 - \imath\gamma_i\omega}$$

that adds up to the dielectric function yet calculated for free-electrons [10]. Here ω is the radiation frequency while ω_i is the resonance frequency of the i-th interband transition.

Generally, if N interband transitions are considered, dielectric function results

$$\epsilon(\omega) = \epsilon_\infty - \frac{\omega_p^2}{\omega^2 + \imath\gamma\omega} + \sum_{i=1}^{N} \frac{A_i}{\omega_i^2 - \omega^2 - \imath\gamma_i\omega} \tag{1.18}$$

For example, taking into account 4 interband transitions, *L4* model is obtained. Reminding the relationship between ϵ and σ (Eq.1.8) and renaming coefficients, dielectric function becomes

$$\epsilon(\omega) = \epsilon_\infty - \frac{\imath\sigma}{\epsilon_0\omega} + \sum_{i=1}^{N} \frac{C_i}{\omega^2 + \imath A_i\omega + B_i}. \tag{1.19}$$

Coefficients for eq. 1.19 were calculated by Nordlander and Hao [11] and are shown in table 1.1. In figure 1.2 can be observed that *L4* analytical dielectric function $\epsilon(\omega)$ fits very well experimental data and it turns helpful for numerical calculations, due to the computationally simple formula for $\epsilon(\omega)$.

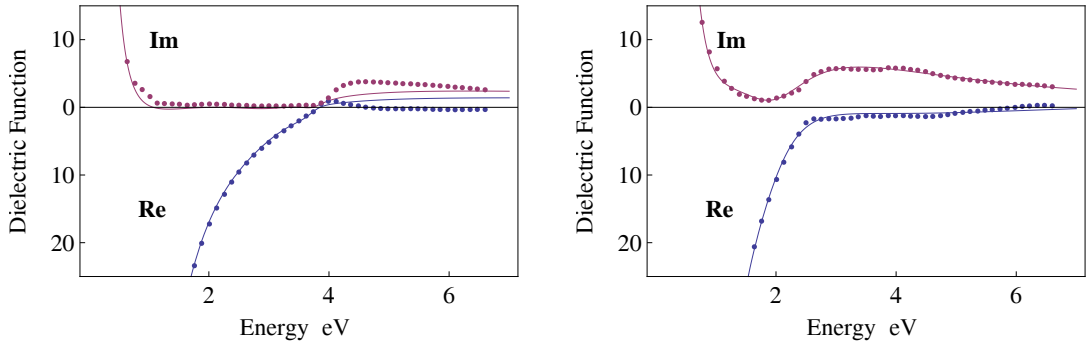

(a) Silver **(b)** Gold

Figure 1.2: Dielectric constant from *L4* model and experimental data from Johnson and Christy

1.2 Plasmon Polaritons

1.2.1 Volume Plasmons

Considering ϵ from free-electron model (eq. 1.15) and considering its high frequency limit ($\omega > \omega_p \gg \gamma$, therefore, neglecting interband contribution to $\epsilon(\omega)$), it is easy to show that metals are transparent to the radiation. Therefore $\epsilon(\omega)$ is predominantly real, as imaginary part becomes unimportant, and it results

$$\epsilon(\omega) \sim \epsilon_1(\omega) = 1 - \frac{\omega_p^2}{\omega^2}. \tag{1.20}$$

Reminding eq. 1.1c, 1.1d from Maxwell's equations, where $J_{ext} = 0$ is assumed, and combining them with the above dielectric function, a wave equation is found. Thus in this regime metal supports propagating waves whose dispersion relation results

$$\omega^2 = \omega_p^2 + k^2 c^2 \tag{1.21}$$

On one side, only transverse electromagnetic waves propagates through the plasma with the dispersion relation above. On the other side, electron sea presents longitudinal quanta oscillations against fixed ions with ω_p frequency. The quanta of these charge oscillations are called *volume plasmons* and, due to their longitudinal nature, they cannot couple with transverse EM waves. Thus, the only way to excite volume plasmons is by particle impact.

1.2.2 Surface Plasmon Polaritons

An other type of plasmon oscillation, that has a central role in this work, is Surface Plasmons (*SP*). It arises at an interface between a metal and a dielectric. In particular, if oscillations occur at extended interfaces they are named Surface Plasmon Polariton (*SPP*), otherwise, if they occur at the surface of three-dimensional confined nanoparticles, excitations are called Localized Surface Plasmons (*LSP*). Here *SPPs* will be widely described while *LSP* will be introduced in section 1.2.3.

Surface plasmon polaritons consist of electromagetic excitations propagating along the interface between a dielectric and a metal and are confined evanescently in the perpendicular direction. Such waves arise when incident EM radiation couples to the oscillation modes of conduction-electron plasma at the interface. Due to the confinement in sub-wavelength volumes at the interface, EM field enhancement can be obtained.

The startpoint to study physical properties of *SPP* is the wave equations obtained by combining eq. 1.1c and 1.1d from Maxwell's equations:

$$\nabla^2 \mathbf{E} - \frac{\epsilon}{c^2} \frac{\partial^2 \mathbf{E}}{\partial t^2} = 0, \tag{1.22}$$

where negligible variation of ϵ is assumed over distances of optical wavelengths. Considering, in all generality, a harmonic time dependence $\mathbf{E}(\mathbf{r}, t) = \mathbf{E}(\mathbf{r}) e^{-\imath\omega t}$, the wave equation results

$$\nabla^2 \mathbf{E} + k_0^2 \epsilon \mathbf{E} = 0, \tag{1.23}$$

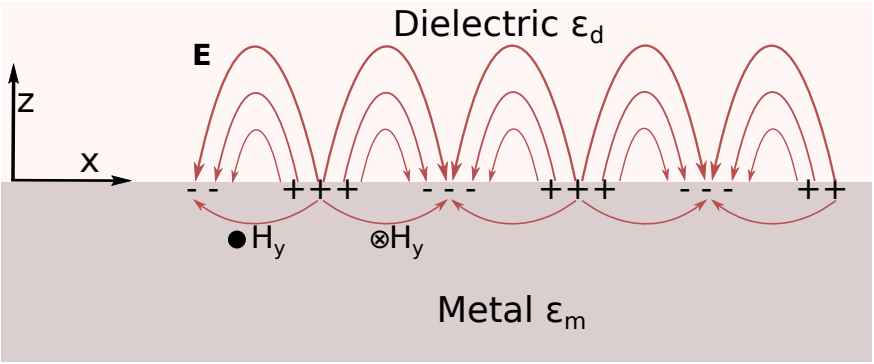

Figure 1.3: Geometry for SPP propagation at interface berween a metal and a dielectric. Electric and magnetic fields for the p-polarized SPP are also described.

where $k_0 = \frac{\omega}{c}$ is the wave vector of the propagating radiation in vacuum, and in this form it is known as the *Helmholtz equation*.

Assuming a semi-infinite media geometry as described in figure 1.3, waves travel along x-direction while ϵ depends only on z-direction. Moreover, plane interface is assumed between metal and dielectric, that coincides with $z = 0$.

Under this geometry assumptions, propagating waves at $z = 0$ interface along x-direction can be described as $\mathbf{E}(x, y, z) = \mathbf{E}(z)e^{i\beta x}$, where β, the *propagation constant*, is the component of the wave vector in direction of propagation. This yields a simplified form of eq. 1.23

$$\frac{\partial^2 \mathbf{E}(z)}{\partial z^2} + (k_0^2\epsilon - \beta^2)\mathbf{E}(z) = 0. \tag{1.24}$$

A similar equation can be found for the magnetic field $\mathbf{H}$. In order to solve these two equations and to get explicit expressions for the fields, boundary conditions are imposed at the interface $z = 0$.

Two sets of solutions with different polarization are found, according to the polarization of the incident radiation: transverse magnetic (TM) and transverse electric (TE). Once defined the scattering plane as the plane on which the incident and the reflected radiation lay, the TM wave has magnetic field $\mathbf{H}$ perpendicular to this plane while the TE wave has the electric field perpendicular to the scattering plane. It is simple to show that surface plasmon polaritons only exist for TM polarization, so solutions for the electric field will have propagating component along x-direction with β wave vector, null component along y-direction and evanescent component along z-direction.

For TM modes a dispersion relation is found, after imposing boundary conditions

$$\beta = k_0\sqrt{\frac{\epsilon_m\epsilon_d}{\epsilon_m + \epsilon_d}} \tag{1.25}$$

where ϵ_m and ϵ_d are respectively dielectric function of the metal and the dielectric. This relation is valid for both real and complex ϵ_m, or equivalently for metals without or with attenuation respectively.

Ideal conductor metal An explicit dispersion relation $\omega(\beta)$ can be found, for example, assuming that the metal has no attenuation and thus considering a purely real dielectric function from eq. 1.20 for ϵ_m. In figure 1.4 the dispersion relation $\omega(\beta)$ and both real and immaginary part of the wave vector β are plotted for two different interfaces air/metal and silica/metal. SPP excitations correspond to the part of the dispersion curve at the right side of the light line due to their bound nature. For air and silica real dielectric constants are considered respectively 1 and 2.25.

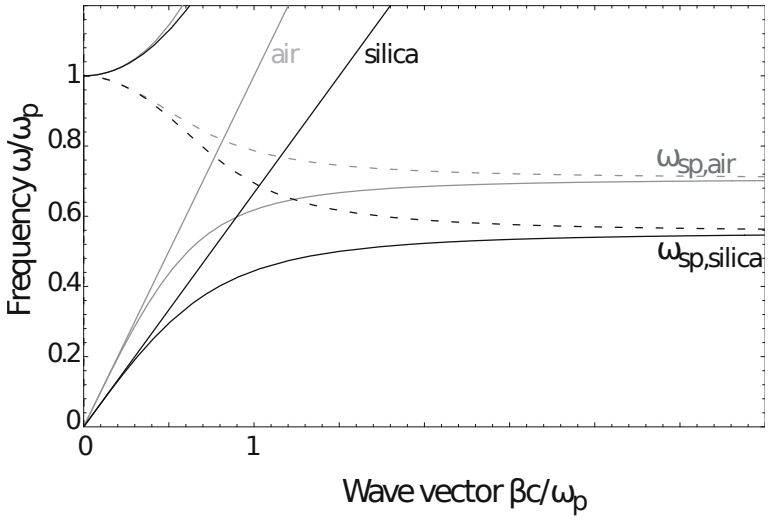

Figure 1.4: Dispersion relation at air/Drude metal and silica/Drude metal interfaces for dispersionless metals. Solid and dashed curves represent respectively $Re\{\beta\}$ and $Im\{\beta\}$ while straight lines represent light lines $\omega = kc/n$

For large wave vectors, frequency of SPPs tends to finite value, the *surface plasmon frequency* ω_{sp}. In fact, inserting eq. 1.20 in eq. 1.25, for large k it results

$$\omega_{sp} = \frac{\omega_p}{\sqrt{1+\epsilon_d}} \tag{1.26}$$

As ω approaches to ω_{sp}, wave vector tends to infinity and group velocity of oscillation $v_g = \frac{\partial\omega}{\partial k}$ tends to zero. In this case oscillation mode acquires electrostatic character and it is called *surface plasmon*. Therefore such mode is obtained when $\epsilon_m(\omega) + \epsilon_d = 0$.

Real metal at interface Above, the metal at the interface was assumed to be an ideal conductor (no dissipation). If real metal is then considered, both ϵ_m and β become complex quantities. In this case ω_{sp} is reached at a finite wave vector and excitation becomes a damped SPP oscillation with a propagation length $L = (2Im(\beta))^{-1}$ (typically between 10 and 100 µm). Additionally, this sets a lower limit for oscillation wavelength and for confinement length perpendiculary to the interface.

It is important to underline that SPP cannot be excited at an interface directly by incident electromagnetic radiation since the propagation constant β is always greater than the component of radiation wave vector k along the interface. Two different techniques for

coupling radiation with SPPs are (i) *prism coupling* and (ii)*grating coupling* and they will be described in section 1.3.

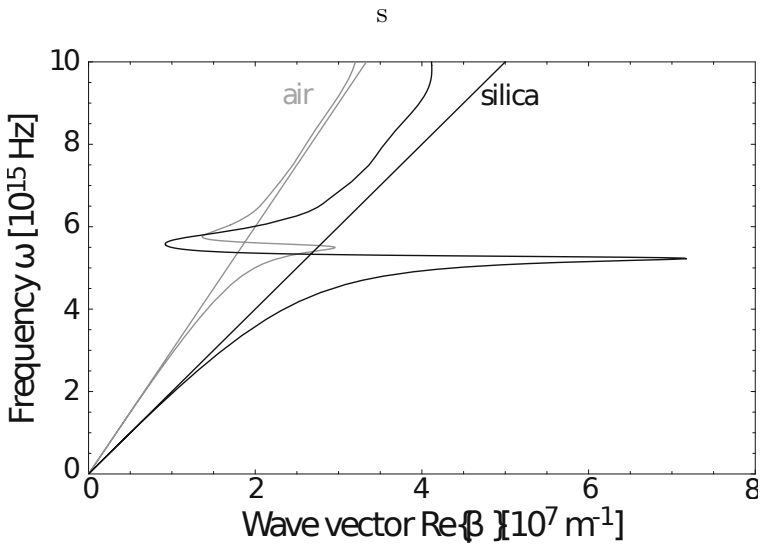

Figure 1.5: Dispersion relation at air/metal and silica/metal interfaces for real metals (silver in this case).

1.2.3 Localized Surface Plasmons

Before starting a more detailed discussion about excitation of SPPs, it is worth introducing briefly the second type of surface plasmons, that is *localized surface plasmon*. This second fundamental excitation is non-propagating and occurzs in presence of confined nanostructures, whose electrons can directly couple to the electromagnetic radiation. The curved surface of a particle with sub-wavelength size produces a restoring force on the electrons driven by the oscillating EM field, so that resonances can arise. This leads to field enhancement both inside the particle and outside in the adjacent sub-wavelength volume.

In contrast to SPPs which need coupling techniques, localized plasmon resonance can be directly excited by EM radiation thanks to the restoring force on the electrons, consequence of the curved surface. Moreover, resonance frequency depends on the shape and the size of metal particles, and there is no analytic model except for spherical or ellipsoidal particles.

For example, Mie theory, introduced by Gustav Mie in 1908[12], allows to study the scattering by a single non-interacting spherical particle by expanding solution in spherical multipole partial waves. At first approximation, if the particle size R is smaller than both radiation wavelength λ and distance between particles d, only the dipole term can be considered and the system may be approximated as a group of interating dipoles. Under these assumptions two different regime are found, depending on the distance between particle. On one hand, if $d \ll \lambda$ then near-field interaction with a dependence of d^{-3} dominates and strong field localizaton is observed in space between adjacent particles. On the other hand, if $d \gg \lambda$ there is larger particle separation so far-field dipolar coupling with dependence of d^{-1} dominates.

1.3 Excitation of Surface plasmons

As previously observed, in order to excite SPP special techniques for phase-matching are needed, since projection of wave vector of the radiation along the interface ($k_x = k \sin(\theta)$) is always smaller than the SPP propagation constant β.

1.3.1 Prism Coupling

A way to get phase-matching to SPPs is to put a thin metal layer between two insulators with different real dielectric constants. One is assumed to be air($\epsilon_1 = 1$) and the other is a dielectric material in the form of a prism with $\epsilon_2 > 1$.

If, inside the prism, the radiation impacts on the prism/metal interface with θ incidence angle and it is totally reflected, the metal will have an in-plane wave vector $k_x = k\sqrt{\epsilon_2}\sin(\theta)$ that is sufficient to excite a SPP at metal/air interface. Therefore, the excitation of a SPP is detected experimentally as a minimum in the reflected light because, in this case, most of the radiation remains confined at the interface instead of being reflected backwards.

In figure 1.6 both dispersion relations are ploted for air/metal and prism/metal interfaces, where a Drude metal is considered. Since light line in prism crosses the air/metal SPP dispersion relation, it implies that EM waves in prism are able to excite SPP modes at air/metal interface.

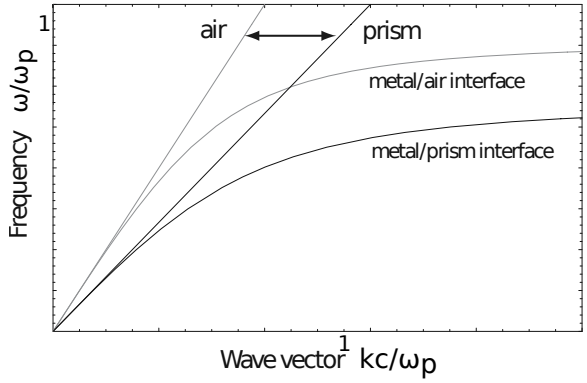

Figure 1.6: SPP dispersion and light lines for prism coupling. The accessible propagation constants for SPP are those between the two light lines.

Two common geometries are usually used to excite SPP modes. Both Kretschmann configuration and Otto configuration are illustrated in figure 1.7 and both are based on attenuated total internal reflection (ATR) at prism/metal interface. In Kretschmann geometry a thin metal layer is directly deposited on the glass prism whereas in Otto geometry metal layer and prism are separated by a thin air gap.

1.3.2 Grating Coupling

Another way to provide the missing wave vector in order to couple impinging photons and SPPs is patterning the metal surface with a lattice of grooves or holes. The ordered

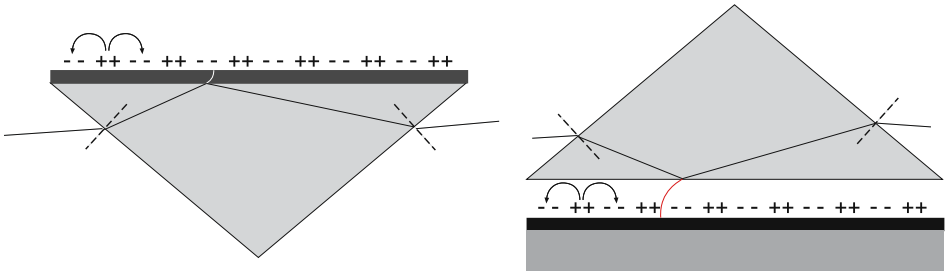

Figure 1.7: Prism coupling to SPPs via attenuated total internal reflection in Kretschmann (left) and Otto (right) configurations.

array of corrugations can be described by a primitive cell and basis vectors. This yields the presence of reciprocal lattice vectors, and these can provide the missing momentum needed for SPP excitation.

For a simple one-dimensional array of grooves with its periodicity a, illustrated in figure 1.8, SPP excitation arises whenever the following condition is satisfied

$$\beta = k\sin(\theta) + \frac{2\pi}{a}j. \tag{1.27}$$

In this equatiom $k\sin(\theta)$ is the in-plane component of incident light wavevector and $\frac{2\pi}{a}j$ is a wavevector from reciprocal lattice, where $j \in \mathbb{Z}$. Here $\mathbf{k}$ is considered parallel to the grating direction so incidence plan is perpendicular to the grooves.

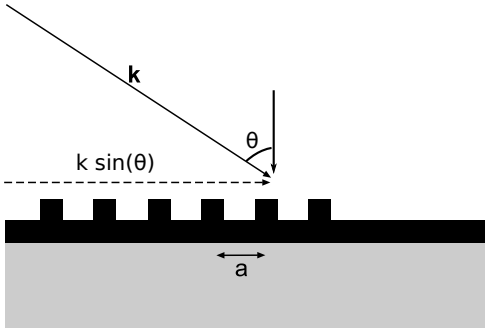

Figure 1.8: Grating coupling between light and SPPs.

If corrugations at interface are shallow, with depth of order of 10 nm, no significant changes occur to the SPP dispersion relation so eq. 1.25 can be used for β. As with prism coupling, excitation of SPPs is detected as a minimum in the reflected intensity. In the presence of a grating also the reverse process can take place. A SPP travelling along a surface can couple to the light and radiate if meets up a grating.

As the size of corrugations increases, the interface can no longer be treated as a small perturbation of the flat interface and dispersion relation 1.25 is no more accurate. Moreover, localized modes arise as the depth of the grooves grows. A further case will be treated in section 1.4, that is when grating lattice becomes an ordered array of holes through the metal film. Such system presents peculiar optical properties, like the extraordinary optical transmission (EOT), as showed below.

1.3.3 1D sinusoidal grating

Surface plasmons can be excited, for example, on a metallic surface patterned with a one-dimensional sinusoidal grating. Besides the coupling where $\mathbf{k_0}$ of the incident light is aligned with the grating direction, as depicted in figure 1.8, the plasmon excitation can occur even when the plane of incidence is azimuthally rotated with respect to the grating direction [13]. Such a configuration is called *conical mounting* and it is presented in figure 1.9. In this case the component of wave vector parallel to the sample surface, given by $k_T = k_0 \sin(\theta)$ where θ is the incidence angle, it is not parallel to the direction of the grating given by the reciprocal space vector $\mathbf{G} = \frac{2\pi}{\Lambda}\hat{\mathbf{G}}$ where Λ is the periodicity of the grating. In fact there is a nonzero azimuth angle ϕ between the two directions. Only the component of $\mathbf{G}$ normal to the scattering plane is transferred for the coupling, and thus two surface plasmons can be excited in directions nonparallel to the scattering plane [14]. The resonance condition can be found as follows, for both cases with $\beta < G$ and $\beta > G$:

$$\begin{cases} \beta_x = G\cos\phi - k_T = G\cos\phi - \frac{2\pi}{\lambda}\sin\theta \\ \beta_y = G\sin\phi \end{cases} \qquad \text{for } G > \beta \tag{1.28}$$

$$\begin{cases} \beta_x = \mp G\cos\phi - k_T = \mp G\cos\phi - \frac{2\pi}{\lambda}\sin\theta \\ \beta_y = \mp G\sin\phi \end{cases} \qquad \text{for } G < \beta \tag{1.29}$$

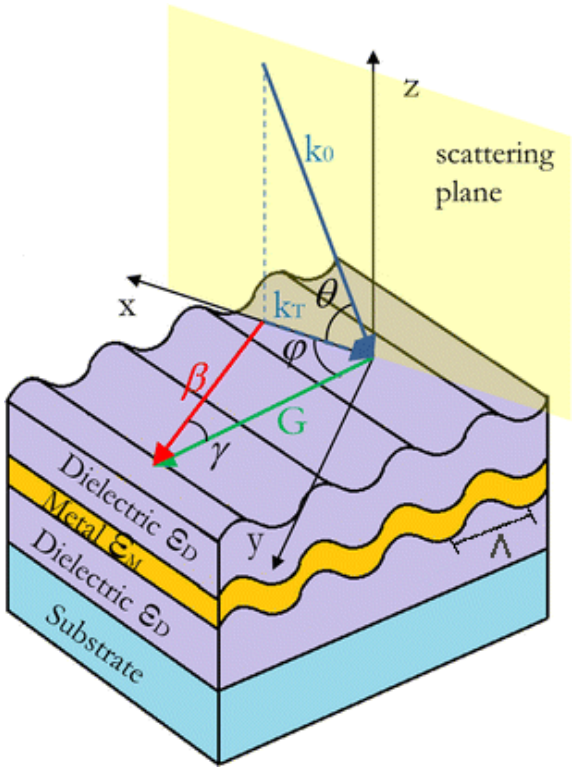

Figure 1.9: Scheme for SPP excitation in the conical mounting.

Measurements of the reflectance angular spectra can be done varying the incidence angle

θ once fixed a wavelength for the light source and an azimuth angle ϕ. The excitation of the two surface plasmons is revealed as two dips in such spectra. If the spectra are acquired for multiple wavelengths shifts of the reflectance dip are observed.

1.4 Nanohole array and extraordinary transmission

As this work will focus especially on nanoholes arrays in metal films, a thorough description of their plasmonic properties will be presented in this section. The presence of surface plasmon polariton give these nanostructures special optical properties, as *extraordinary optical transmission (EOT)*, first described by Ebbesen [5]. This phenomenon constists in the transmission through a metallic nanohole array with subwavelength size of more light than that which would pass through a hole with an area corresponding to the sum of the nanoholes areas. EOT arises and becomes relevant when hole's radius r is smaller than wavelength λ_0 the of incident radiation.

For apertures with $r \gg \lambda_0$ propagating modes of radiation are allowed so transmission coefficient T, given by the ratio of total transmitted intensity to the incident intensity on holes area, is similar to 1.

In case of sub-wavelength apertures Huygens-Fresnel principle can not be used and radiation does not propagate but it is transmitted by tunneling through the holes. Despite this, Bethe and Bouwkamp [15] provided an analytical solution for the transmission coefficient for a single hole T_{SH} of normally incident radiation through a single sub-wavelength circular hole in a perfectly conducting and opaque and infinitely thin screen:

$$T_{SH} = \frac{64}{27\pi^2}(kr)^4 \propto \left(\frac{r}{\lambda_0}\right)^4 \tag{1.30}$$

Relaxing the infinitely thin screen assumption and considering a finite thickness h, numerical simulations show that T_{SH} decreases exponentially with h. On the other side, if finite conductivity is taken into account, it is enough for h to be on the order of several skin depths to restore screen's opacity.

Eq. 1.30 shows that transmission should rapidly become zero as λ_0 gets greater than hole's dimension. Despite this, surface plasmon polaritons can enhance tranmission through such holes if a metal layer is patterned with a regular periodic lattice of holes [16]. Briefly, due to grating coupling, incident light excites SPP that travels through the hole then it is scattered in far field on the other side.

The presence of an ordered array yields a reciprocal space of wave vectors which helps radiation to couple with SPP. From eq. 1.27 it is easy to rewrite the condition, i.e., for a square lattice of holes with periodicity a:

$$\beta = k\sin(\theta) + nG_x + mG_y = k\sin(\theta) + (n+m)\frac{2\pi}{a} \tag{1.31}$$

Here k is the incident wavevector, G_x and G_y are basis wavevectors of the reciprocal lattice and n, m are Miller integer indexes which define scattering order, thus direction

of propagation of the excited SPP. Therefore, transmission maxima peaks can occur in presence of surface plasmon resonance when standing SPPs are formed on the surface (also called SPP-Bloch waves [17, 18]). It can be shown that such excitation arises, for normally incident radiation, whenever is fullfiled the condition

$$\lambda_{SPP}(n,m) = \frac{a}{\sqrt{n^2+m^2}}\sqrt{\frac{\epsilon_m\epsilon_d}{\epsilon_m+\epsilon_d}}. \tag{1.32}$$

Here, to get a first approximation, β from eq. 1.25 was assumed, where a flat infinite interface between metal and dielectric is considered. A rough approximation is done, just considering the periodicity of the structure in the null-aperture and, as a consequence, the predicted peak positions are at slightly shorter wavelengths than those observed experimentally.

Under the same assumption, a similar condition for the maxima can be found for an hexagonal hole array with periodicity a [19]:

$$\lambda_{SPP}(n,m) = \frac{a}{\sqrt{\frac{4}{3}(n^2+nm+m^2)}}\sqrt{\frac{\epsilon_m\epsilon_d}{\epsilon_m+\epsilon_d}}. \tag{1.33}$$

As nanohole array can not be treated as small perturbation of the flat interface, in order to get more precise relations than eq. 1.32, 1.33 a more accurate relation for the propagation constant β of SPPs would be necessary.

Moreover, these relations are valid for a single interface between two semi-infinite layers. As the nanohole array has two interfaces that can be in contact with different dielectrics, different transmission spectra with different positions of the peaks can be obtained depending which of the interfaces is illuminated by the incident radiation.

In presence of surface plasmon resonance, extraordinary transmission occurs. Let be defined a normalized transmission coefficient T_{norm} as the ratio of the transmitted intensity through the nanohole array T_{NHA} to the sum of the ordinary transmissions of single holes T_{SH}.

$$T_{norm} = \frac{T_{NHA}}{\sum_j T_{SHj}} \tag{1.34}$$

At the surface plasmon resonance maxima with $T_{norm} > 1$ can be found in the transmission spectrum and this means that more light than that which incides on the area of all the apertures is transmitted. This is possible because even the light impinging on opaque regions between the holes can be channeled and transmitted to the other side via propagating SPPs.

This *extraordinary transmission* property of nanoholes array was first demonstrated by Ebbesen and co-workers for a square array of circular holes in a thin silver film [5]. In figure 1.10a transmission spectrum of normally incident radiation on a 200 nm nm thick film of silver patterned with a nanohole array with 150 nm hole diameter and 900 nm periodicity. Several transmission peaks can be observed, two of which occur at wavelength greater than both hole diameter and array periodicity. This suggests that such transimission is not due to ordinary tunneling through holes but rather is mediated via SPPs.

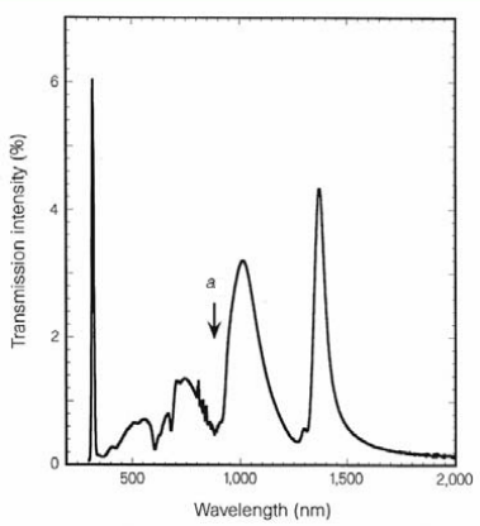

(a) Normal-incidence transmission spectrum for a 200 nm silver film with square array of holes of 150 nm diameter with $a = 900$ nm periodicity.

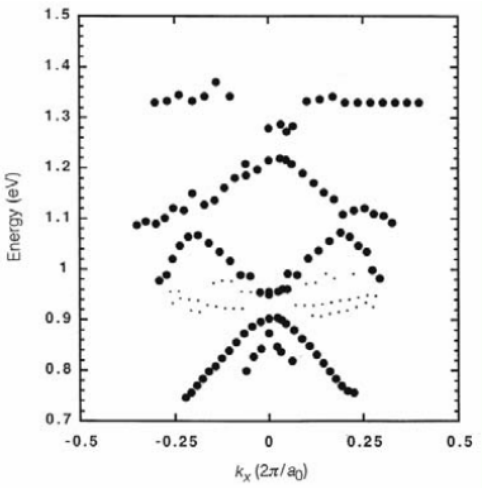

(b) Dispersion relation of grating-coupled SPPs along [10] direction extracted from the energy of transmission peaks as in fig. 1.10a

Figure 1.10: Plots copyrighted by Ebbesen et al.,1998[5]

An important advantage of the nanoholes is the simplicity with which spectral properties can be tuned. Despite the rough approximations used, it is clear from eq. 1.32, 1.33 that positions of peaks in the spectrum are directly proportional to the periodicity of the array.

Other geometrical parameters also influence the transmission spectra $T(\lambda)$, as described here after.

Thickness t If the thickness of the metal film is of the order of the skin depth δ, SPPs excited by incident radiation on front interface might couple and produce SPPs excitation on the other interface, when adjacent dielectric media are equal. However, in this work UV-Vis-NIR wavelengths will be studied and in this range skin depth is much smaller than film thickness, $\delta \sim 1 \div 5$ nm vs. $t \sim 100$ nm. Under this assumption there is no tranmission through the metal so it is all due the tunneling of SPPs into the holes.

Hole diameter d If d was larger enough to allow propagating modes transmission could be modulated via resonances of waveguide modes. However, when $d \leq \lambda/2$ the hole allows only tunneling modes for the incident light and this condition is fulfilled. In fact, in this work small diameters below 300 nm will be considered whereas resonance wavelengths will be greater than 600 nm. Therefore, transmission spectra is once again controlled by SPPs and their tunneling through the holes.

Hole symmetry Different transmission spectra are observed with square rather than circular holes [20]. While circular hole, due to its symmetry, acts similarly in response to incident light with different polarization, square holes produce different spectra

depending on polarization.

Geometrical parameters are chosen in order to point out extraordinary optical transimission due to the tunneling of SPP through the holes rather than other transmission mechanisms.

In addition to SPPs due to grating coupling, the penetration of the incident field inside the metal enables the strong localization of the field of localized surface plasmons on the rim of the each hole. In case of a single aperture in a flat film, presence of field hot-spots has two consequences that affect the transmission spectrum. On one hand, hole's effective diameter is increased as well as the cutoff wavelength, beyond which propagative modes are not allowed inside the hole. On other hand, the field-enhancement at the rim, whenever localized plasmons are excited, also increases the transmission. Nevertheless, a study of Degiron and Ebbesen [21] about role of localized modes in EOT through sub-wavelength nanohole arrays showed that they produce only minor changes in the transmission spectrum compared to the importance of propagating SPP.

At the end of this section, it must be stressed that the frequency-selective enhanced light transmission generates a lot of interest for use in different practical applications. One specific application, which represents the purpose of this work, is the sensing of the refractive index variations at the interface between nanohole array and adjacent dielectric for biosensing. It is based on the dependence of surface plasmon resonance upon dielectric constants of the metal and the surrounding medium, as showed in eq. 1.32, 1.33.

Chapter 2

Nano Hole Array fabrication

In this chapter the techniques used to produce nanoholes array will be presented. As showed in section 1.4 plasmonic properties of nanostructures strongly depends on both surrounding dielectric medium and geometrical parameters. On one side it is necessary to be able to simply tune dimensional parameters of nanohole arays during their synthesis. On the other side, for the purpose of this work, that is producing high-sensitivity high-specificity biosensors using nanohole arrays, is also needed a cost-effective way to produce such devices.

Firstly, will be presented some of the methods of nanofabrication that can be employed to create pattern of nanostructures on a surface. Secondly a in-depth presentation will be given of the technique that best fits the purpose of this work, *Nano Sphere Lithography (NSL)*, and about how it can be used to mass-produce well-ordered nanohole arrays in a cost-effective way.

Photolithography The most widely used techniques used for fabrication of nanostructures controlling geometrical parameters are lithograpic methods, which consist in drawing a pattern on a film using a mask. For example *photolithography* [22, 23] uses light to transfer a pattern or its negative from a photomask to a spin-coated layer of photoresist material. Then chemical etching steps provide to finally write the desired pattern on the film above the photoresist and then remove the latter one.

Due to its diffraction-limited resolution photolitography has not been widely applied to nanostructures fabrication. The minimum feature size that can be drawn is $\sim \lambda/2$, where λ is wavelength of the incident light, thus deep UV light has to be used to reach resolution down to 50 nm. To overcome the difraction limit of light X-ray lithography [24] is also used, allowing to reach better resolutions but involving high fabrication costs.

Electron Beam Lithography A method that allows to reach sub-10nm resolution is to use focused beam of electrons instead of photons. Electron Beam Lithography (EBL) [23] consists in drawing a pattern on a surface covered with an electron-sensitive material employing narrow e^- beams of tens keV without using any mask. Despite its excellent size control, low sample throughput and high cost make it unsuitable for mass-fabrication.

Focused Ion Beam Lithography Like EBL method, this consists in a maskless technique to create nanostructured patterns across a surface using narrow beams of accelerated particles. However, in this case no resist material is needed as the ion beam directly drills the material used for the nanostructures. Ions are much heavier than electrons and this give them a smaller wavelength so there is negligible diffraction. This method allows to reach resolutions down to a couple of nanometers but on the other side, as EBL method, it is unsuitable for mass-fabrication due to high-cost and low throughput. This method was employed by Ebbesen et al. [5] to drill directly nanohole arrays on thin layers of silver, thus showing Extraordinary Optical Transmission (cfr. section 1.4).

Nano Sphere Lithography (NSL) This is a powerfull fabrication technique to produce wide and well-ordered nanoparticle arrays in a high-throughput and cost-effective way and controlling finely shape, size and interparticle spacing of the nanostructures. Named firstly "natural lithography " and described by Deckman [25], this technique was then renamed Nano Sphere Lithography, developed and operationally described in a more systematic way by Van Duyne et al.[6, 26].

To produce any nanostructure by NSL, first a self-assembled two-dimensional mask is formed from size-monodisperse polystyrene (PS) nanospheres (NS) of diameter D, in the range 100 nm - 1 μm. Thus, a monolayered hexagonally close-packed pattern of spheres crystallizes on a substrate. Large well-ordered masks, of order of 1 cm^2, can be easily produced. However a variety of defects can arise due to nanospheres diameter polydispersity and the presence of vacancies, slip dislocations and polycrystalline domains. Therefore defect-free domain size is reduced in the 10-100 μm range[27]. Usually spheres are deposited on the substrate by spin-coating or drop-coating, but hereby another way of self-assembling will be used and described.

Once a mask is obtained a metallic film is deposited through the mask. In order to get the nanoholes array, before metallic deposition it is necessary an etching process that shrinks spheres diameter leaving unaltered the lattice and interparticle distances. If metal deposition is done without the etching process another nanostructure is achieved, i.e., an array of triangular prism nanoparticles.
A detailed description of NSL and Nano Hole Array fabrication will be now given.

2.1 Self-assembled monolayer of polystyrene nanospheres

2.1.1 Cleaning of substrates

Three type of substrates will be used, with an area of order of couple cm^2: Soda Lime Glass (SLG), highly-pure *HSQ 300* silica (SiO_2) and monocrystalline silicon (Si). In order to get high order and as few defects as possible, substrates surfaces should have no impurities. For this purpose all the substrates used, firstly, go through two cleaning processes.

The first, named *acid piranha*, consists in the treatment of substrates in a 3:1 solution

of sulfuric acid (H_2SO_4) and hydrogen peroxide (H_2O_2) for 1 hour at the temperature of 90°C. Since it is a strong oxidizing agent, this step removes most of the organic matter impurities from the surfaces and makes them highly hydrophilic.

After thoroughly rinsing the substrates with Milli-Q water (18.2 MΩ/cm resistivity),a *basic piranha* is carried out, which consists in a basic 3:1 solution of ammonium hydroxide (NH_4OH) and hydrogen peroxide. Substrates are treated in this solution for 20 minutes at the temperature of 90°C and it should further increase their hydrophilicity.

2.1.2 Mask self-assembling

The deposition of the nanospheres on the substrate is based on the work of Schatz [28]. Here polystyrene nanospheres with nominal diameter D of 522 nm are used for the mask assembly and a colloidal suspension of nanospheres in water and alcohol is first preparated. After fixing a SLG substrate on the arm of the motorized dipper shown in figure 2.1, a small amount of this solution is deposited on the substrate. As showed in the figure, the substrate with disordered nanospheres on is dipped into the Milli-Q water, and NSs start floating on the surface. Thus, a monolayer of NS is formed thanks to the meniscus between the alcoholic dispersion and the water.

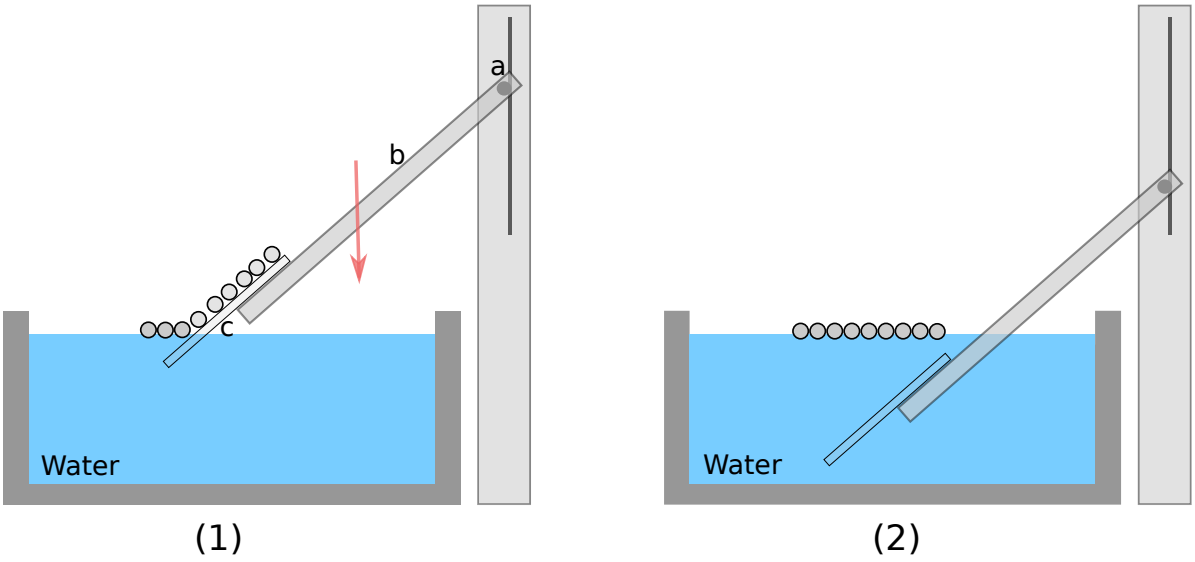

Figure 2.1: The device used for self-assembling mask consists of a rack and pinion system (a) driven by a small electric engine that allows to the T-shaped arm (b) to move vertically at two different speeds. At the end of the arm a SLG substrate (c) is fixed and NSs are deposided on. As the substrate is dipped, in (1), NSs separate from it and start floating on water surface. In (2) a well-ordered monolayer of NS has formed.

Once NS monolayer is formed on the surface, it can be collected with a Si or SiO_2 substrate. Figure 2.2 illustrates how mask is picked up. While the downward step is done automatically the collection step is manual. The desired substrate is dipped with a tweezer by hand, underneath the mask, then it is pulled out slowly, thus collecting the monolayer.

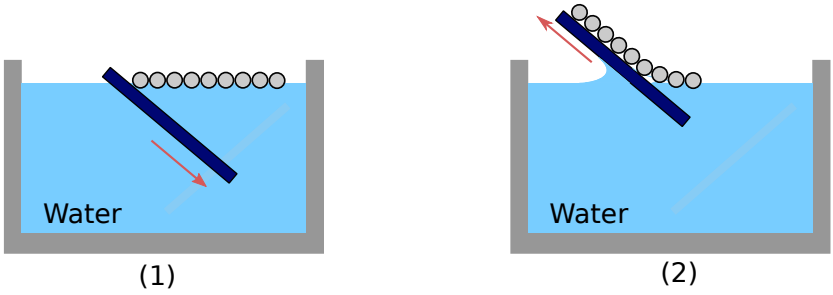

Figure 2.2: Collecting step is here showed. A second substrate is used to manually pick up the monolayer by first dipping it in the water then slowly pulling it out together with the NS mask.

The samples are then dried at room temperature. As the solvent evaporates, the nanospheres, which are free to move on the surface of substrate, are driven by capillary forces that draw them together and thus a hexagonally close-packed pattern is formed. Figure 2.4 shows two images of masks of PS nanospheres of 522 nm diameter, one AFM and one SEM image.

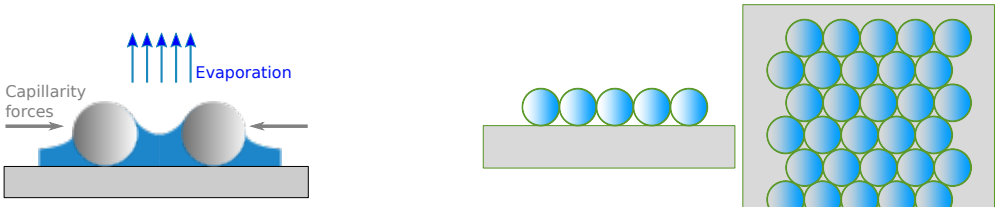

(a) Drying step, while capillarity forces drive the monolayer to a close-packed pattern.

(b)

Figure 2.3: Self-assembled monolayer of PS nanospheres

Nano Triangle Array At this point, if metal is deposited on such mask a honeycomb array of triangularly shaped nanoparticles can be created. In fact during deposition metal reaches the substrate only in interstices between spheres and thus, removing the mask, triangular nanoprisms are produced (figure 2.5). It can be shown that interparticle distance d between triangles is linked to the nanospheres diameter by

$$d = \frac{1}{\sqrt{3}} D. \tag{2.1}$$

Moreover, it can be pointed out a relationship between lateral in-plane dimension of the nanotriangle (a) and NS's diameter [26]:

$$a = \frac{3}{2}\left(\sqrt{3} - 1 - \frac{1}{\sqrt{3}}\right) D \approx 0.233D \approx \frac{1}{4}D \tag{2.2}$$

This firstly stresses how geometrical dimensions of the desired nanostructure can be simply tuned thanks to NSL technique.

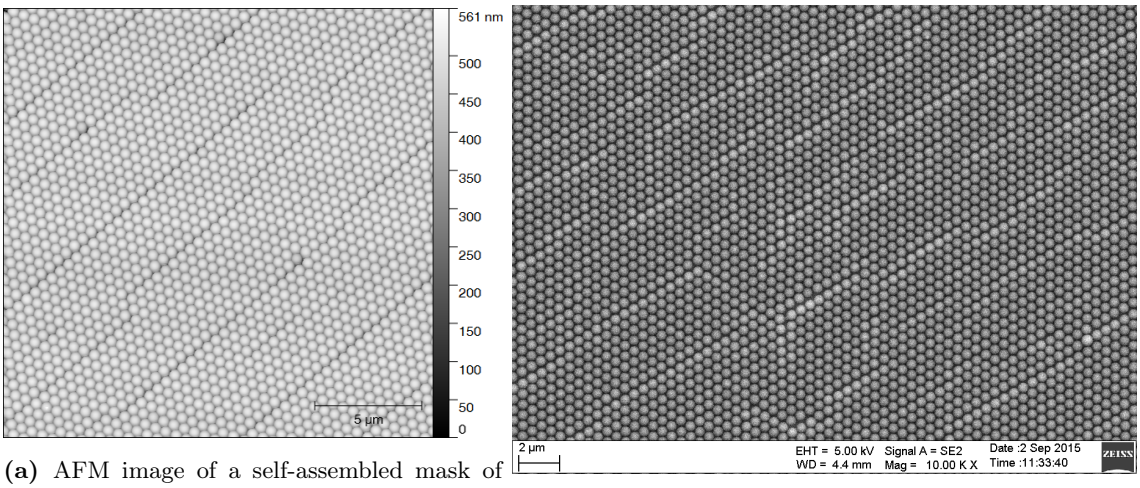

(a) AFM image of a self-assembled mask of nanospheres

(b) SEM image of a self-assembled mask of nanospheres

Figure 2.4: Self-assembled mask of PS nanospheres of 522nm diameter

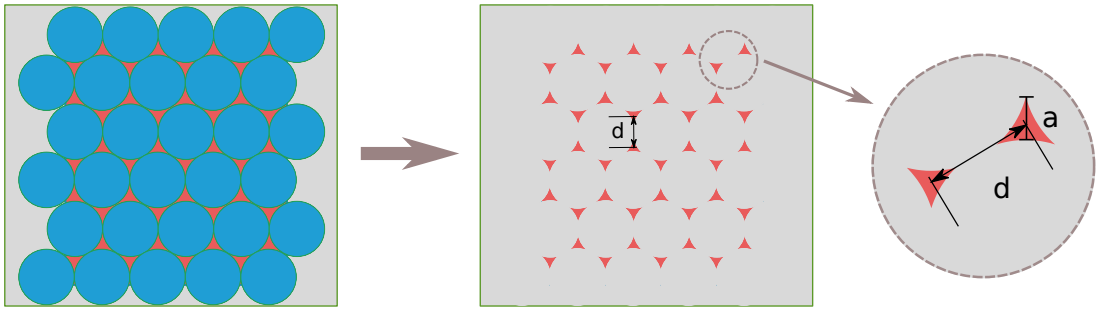

Figure 2.5: Nano Triangle Array (NTA) from NSL method. First metal is deposided (left) then mask is removed (right).

2.2 Reactive Ion Etching

2.2.1 Description of the RIE process

In order to produce nanohole arrays using NS masks they have to go through another process, that shrinks polystyrene nanospheres leaving unchanged the lattice structure and thus creating the negative mask for the nanohole. Such process should be able to erode the nanospheres reducing their diameter in a gradual way with a controlled rate without altering periodicity of the initial lattice and thus create an ordered non-close-packed NS array. Reactive Ion Etching (RIE) [29] is the process that best fit this purpose . It consist in a dry ion-assisted chemical etching process which uses a chemically reactive plasma to remove material deposited on a substrate. High-energy ions from the plasma, generated under low pressure, hit the sample surface and react with it.

A typical RIE system consists of a cylindrical vacuum chamber, with a wafer plate to hold substrates situated in the bottom part of the chamber. The plate is electrically isolated from the rest of the chamber, which is usually grounded. Input valve for the gases used for the etching is situated in the top of the chamber while products from etching exit

to the vacuum pump through an inlet situated in the bottom. Etching process is strongly influenced by the type and the amount of the gases employed, and their choice depends on what material has to be etched.

First vacuum is created in the chamber and pressure is typically maintained in a range between 10^{-3}-10^{-1} mbar. As the gas flows into the chamber, a plasma is created by the application of a radio-frequency (RF) electromagnetic field to the plate. The ionizing field is tipically set to a frequency of 13.56 MHz and it is applied at power of a few tens Watts. After the ignition the plate acquires a negative charge and positive ions are driven towards the substrate by the electrostatic field thus generated. On one side, colliding ions can chemically react with the material of the samples, erode it and finally volatile byproducts are desorbed. On the other side, an ion with low chemical reactivity can sputter, and thus physically etch, parts of the material by transfering kinetic energy. All these products diffuse away from the sample and are collected by the vacuum pump. The different steps are illustrated in figure 2.6.

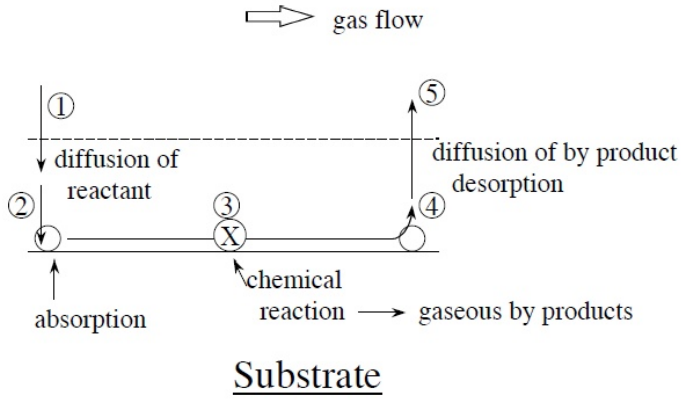

Figure 2.6: Schematic representation of RIE process

Since reactive ions collide perpendicularly the sample, driven by the electric field, the process has a very anisotropic profile and the material is etched mainly in a vertical direction.

Etching process depends on many parameters, such as chamber pressure, gas flows and RF power and choice of these parameters are to be optimized.

2.2.2 RIE on PS nanospheres mask

RIE process is largely used for the production of nanohole arrays by NSL[30, 31]. Here a mixture of two gases is employed: oxygen (O_2) is the chemical reactant while Argon (Ar), which is chemically inert, is used for physical etching. Parameters have been studied empirically and optimal values were found in order to make the etching process stable and reproducible. Two different regimes of etching are possible at low-pressure and at high pressure, as showed in figure 2.7. The low-pressure etching has less gas flow and ions can easily difuse towards the sample driven vertically by the electric field. Thus an anisotropic

Pressure	$9 \cdot 10^{-3}$mbar
O_2 flux	3.7 sccm
Ar flux	1.2 sccm
Bias	199 V
Power	10 W

Table 2.1: Optimal parameters for low-pressure RIE process used in the present work.

erosion on vertical direction is performed. On the other side, a higher gas flow leads to a more isotropic etching of the spheres.

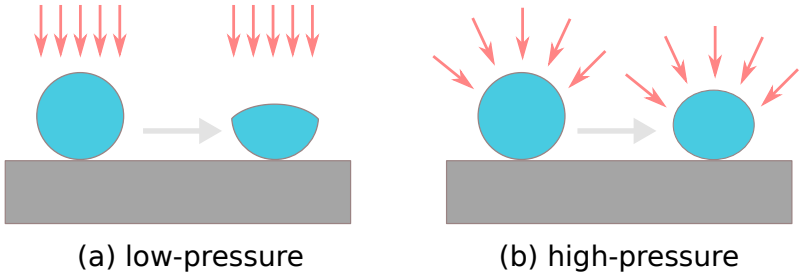

Figure 2.7: The two types of RIE etching.

For production of masks for nanohole arrays low-pressure etching will be used with parameters from table 2.1.

Once fixed these parameters, etching time is the free one that allows to finely control the diameter of spheres, and so the diameter of the nanoholes. For this purpose tests were carried out for different etching time and masks were analized with Scanning Electron Microscopy (SEM) to get average diameter. Using such data it was possible to draw a calibration between etching time and final diameter. Attention must be paid to avoid collapse of nanospheres, caused by excessive etching, by restricting the RIE process to a final diameter greater than half of NS initial diameter.

In figure 2.8 are showed masks that went through RIE process with different times.

2.3 Metal deposition and mask removal

Once an etched mask is created, nanohole arrays are finally obtained by depositing a thin film of metal via sputtering. This process consist in the physical removal of material from a target (here, a metallic target) by the collision of inert atoms (e.g Argon). Atoms from an ionized gas strike the metallic target eroding it and atoms from it are ejected in all directions due to the transfer of kinetic energy to target atoms [32]. The last ones reach the sample through diffusion in the previously evacuated chamber and there start to grow by depositing the desired metallic layer.

Since sputtering source has finite dimension, emission of target atoms can not be considered neither spherically nor uniformly distributed. A large fraction of sputtered atoms

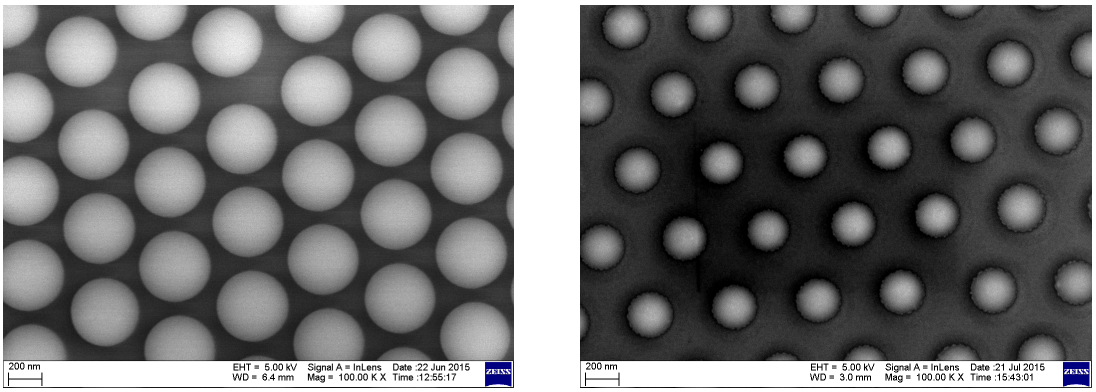

(a) Etching time: 6 minutes

(b) Etching time: 12 minutes

Figure 2.8: Non-closed-packed NS arrays after going through etching processes with different times

have directions of diffusion not perpendicular to the sample and thus shadow effects can arise in deposition through the mask. For a flat deposition, a uniform source is needed and to overcome this problem the sample is put near the target.

2.3.1 Magnetron sputtering

In this work Magnetron Sputtering is used for deposition of metal. A Magnetron Sputtering system consists essentially of a vacuum chamber containing the target and a sample holder, both connected in the same electrical circuit. A high negative DC voltage is applied to the target holder, which is the cathode, while the sample holder is grounded, representing the anode. Once vacuum is created (pressure $\approx 3 \cdot 10^{-6}$mbar), gas flows inside the chamber through an inlet reaching higher pressures of work on order of 10^{-3}mbar. Here Argon was used to create the plasma for target erosion, because it is inert and doesnt react either with the target or with the growing layer. The high electric field ignites the plasma ionizing the Argon atoms and drives them towards the cathode where metallic target is situated. In addition to the electric field, a magnetic field is turned on using magnetrons situated inside the target holder. Such field increases plasma density and confines it in a region near the metallic target, thus speeding up the erosion process and improving sputtering efficiency.

A scheme of Magnetron Sputtering system is presented in figure 2.9. Neutral atoms sputtered from metallic target aren't trapped by electric and magnetic fields but they difuse and collide with other atoms in the atmosphere. Collision rate of diffusig sputtered atoms in strongly dependent on the chamber pressure given by the gas flow. On one hand, collision rate decreases in case of lower pressures making the sputtering less efficient since there are less ionized atoms to hit the target. On the other hand, higher pressures increase both the erosion and the collision rates leading to a less efficient deposition on the sample since sputtered atoms are deflected and few of them reach it. For these reasons pressure of work is usually of order of $10^{-2} - 10^{-1}$mbar.

Figure 2.9 shows a single-target sputtering system. The one used in this work has three target holders and each of them can ignite and confine its own plasma. Therefore, at most three elements can be deposited in the same process. On one hand, metal alloys can be deposited by ingniting plasmas and co-sputtering multiple metals at the same time. On the other, multi-layer deposition is possible by sputtering consecutively different metals.

As in the case of the RIE process, first were found optimal parameters for the power and the voltage applied to each target and the pressure of the chamber. Then, the only free parameter is sputtering time and calibration were done to find deposition rate for each target.

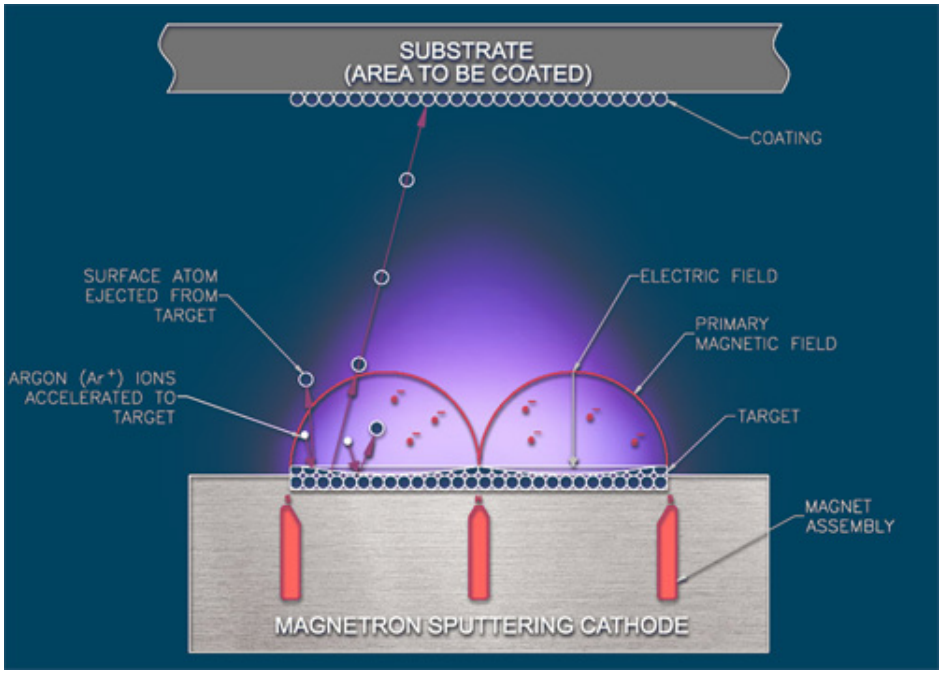

Figure 2.9: Magnetron Sputtering system.

2.3.2 Deposition for NHA and mask removal

Here, multi-layered depositions are performed to get the nanohole arrays. First a 5nm thin layer of titanium (Ti) is deposited in order to enhance the adhesion of the metallic film on the substrate. Then a silver layer and a final gold layer are added. Silver has excellent plasmonic properties but it oxidises, whereas gold doesn't, but has less excellent properties. Therefore a thin film of gold (5-10 nm) is deposited over the silver one (50-100 nm) to protect it from oxidation.

Attention must be paid to the total thickness of the metallic film. This has to be large enough to become opaque for the impinging radiation, thus avoinding the standard transmission through metallic film and favouring EOT through the holes.

Once a proper deposition is done, nanohole arrays are finally obtained by removing NS mask. This step is done by immersing the samples in toluene, which dissolves the

PS nanospheres, and sonicating it for two minutes. Figure 2.10 shows a nanohole array obtained after mask removal.

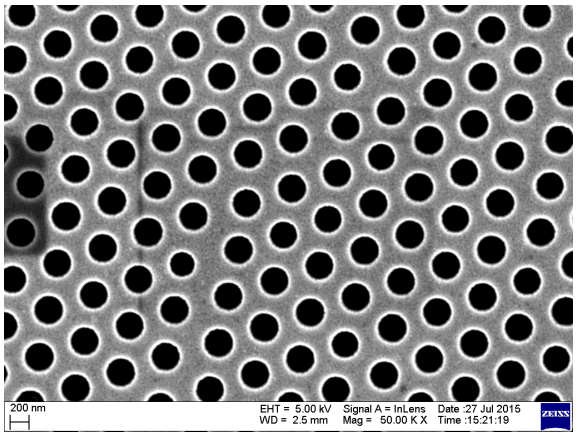

(a) SEM image of a NHA

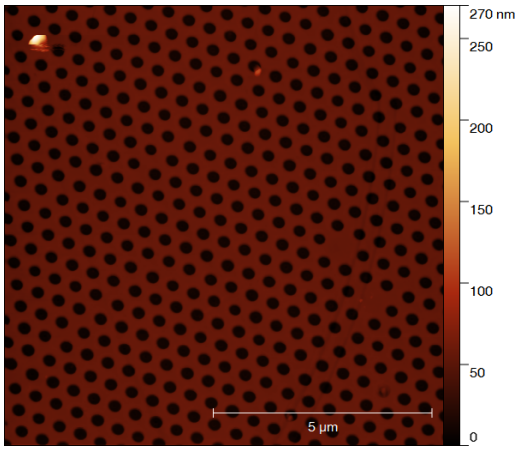

(b) AFM image of a NHA

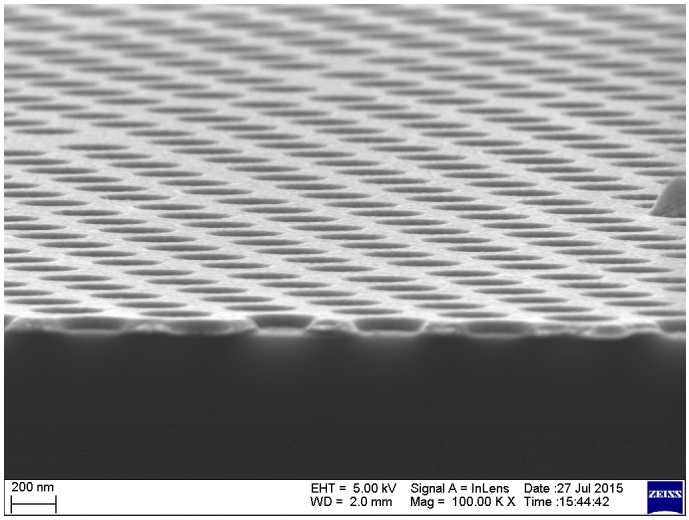

(c) SEM cross-section image of a NHA

Figure 2.10: A nanohole array after mask removal. Mask from 522 nm PS nanospheres was etched for 12 min and then 5 nm of Ti, 45 nm of Ag and 10 nm of Au were deposited.

Therefore, a metallic nanohole array deposited on the chosen substrate is obtained and it is now possible to study its morphology and optical properties. Figure 2.11 summarizes the nanofabrication steps to produce a NHA, from the self-assembly of close-packed mask to the metallic nanohole array.

Once again it must be stressed how simply geometrical parameters can be tuned thanks to NSL.The morphology of an hexagonal nanohole array is fully described by three parameters, the periodicity a, the hole diameter d and the metal film thickness t, which can be finely tuned.

- Periodicity a of the hexagonal array is equal to the initial diameter D of the polystyrene nanospheres used to create the mask.
- Hole diameter d is tuned varying the etching time in the RIE step.

- Thickness t is tuned by changing the metal deposition time.

For d and t calibrations have to be done first, to arrive at a relationship between the time and, respectively, the hole diameter and the thickness.

As pointed out in section 1.4 the plasmonic properties of nanohole arrays are strongly dependent on their morphology. Therefore these properties can be simply tailored for specific purposes. In the next chapter will be showed how such plasmonic properties can be used in order to develop biosensors.

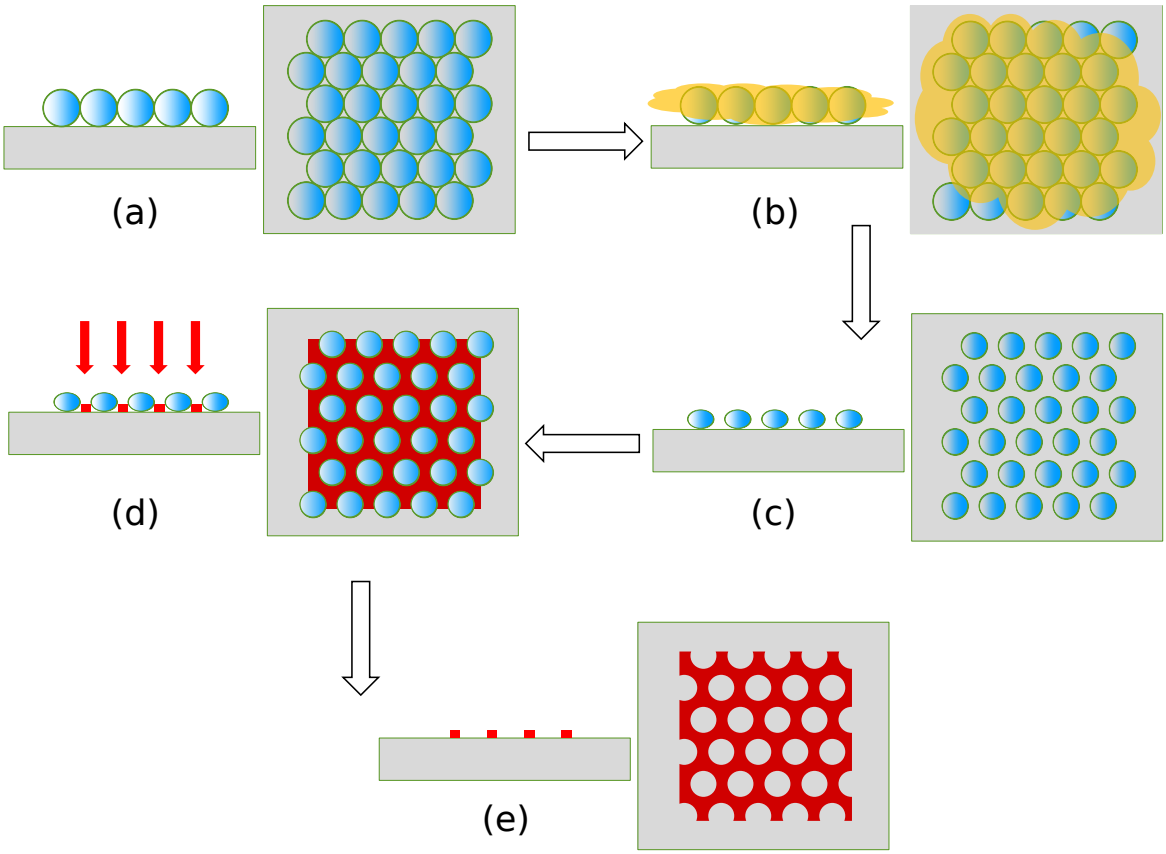

Figure 2.11: Steps for the production of NHA are here summarized. (a)A close-packed mask of PS nanospheres is self-assembled on a substrate. (b)RIE process shrinks the spheres and (c) an hexagonal non-close-packed mask is obtained. (d) Metal is deposided on the substrate through the mask, which is then removed. (e)After the mask removal a metalic nanohole array is obtained.

Chapter 3

Biosensing with nanostructures

A biosensor is a device that can reveal a specific biological compound, called analyte. It fundamentally consists of a biological recognition layer designed to selectivelybind with the analyte and a physical transducer which translates the biochemical interaction with the analyte into a signal that can be more easily measured and quantified [33]. Biological receptors, for example, could be made by enzymes, antibodies, antigens or nucleic acids, which are chosen to specifically interact with the desired analyte thus giving specificity to the device.

The purpose of a biosensor is to produce a physical signal, either electrical or optical, which is proportional to the concentration of the analyte.

Nowadays, plasmonic devices have gained increasing interest both in enhancing the signal from surface-enhanced spectroscopic methods [34] and in sensing as optical transducers [3]. In the last case, the plasmon spectroscopy gained reputation as an high-sensitive method for detecting molecules of both biological and chemical interest. An advantage of plasmonic biosensors over other optical ones is that the analyte does not require to be labelled with an optically-active marker in order to reveal binding events [35].

Therefore plasmonic biosensors are devices with high-sensitivity, high-specificity and laber-free detection for monitoring biomolecular interactions in real time and in the next sections a thorough description will be given.

3.1 Principle of SPR sensing

The application of surface plasmon resonance (SPR) for biosensing was demostrated in 1983 by Liedberg et al. [36] and since then a growing interest produced a wide use of SPR-based biosensors in many domains as biology and medical diagnostics[37].

The promising potential of SPR sensors lies in the very high sensitivity of the surface plasmons excited at a metal-dielectric interface to a change in the refractive index of the adjacent dielectric. Reminding the dispersion relation in eq. 1.25 for the propagation constant β of plasmons and the relationship between refractive index of the dielectric medium n_d and its dielectric constant ϵ_d given by $n_d = \sqrt{\epsilon_d}$, it is clear how a local variation

of n_d yields a change of plasmonic properties.

In fact, a Δn variation in the dielectric constant means a variation of ϵ_d in eq. 1.25 and this subsequently alters the resonance condition between surface plasmons and the interacting optical wave. Depending on which characteristic of the light interacting with plasmons is measured, SPR sensors can be categorized as sensors with angular, wavelength, intensity or phase modulation [38].

Angular modulation In SPR sensors with angular modulation, a monochromatic light wave with a variable angle of incidence is used to excite a surface plasmon. Angular spectra of reflected light are measured at multiple angles of incidence and excitation of surface plasmons is observed as a dip in such a spectrum. The strongest coupling occurs at the minimum in the spectrum, and it corresponds to the angle of resonance. Therefore, when the refractive index changes the resonance angle varies accordingly, and it is measured and used as the sensor output. Prism-coupling SPR sensors relies mainly on this modulation and they will be described in the section 3.2.

Wavelength modulation Here a polychromatic optical source is employed. The plasmon excitation is observed as a dip in wavelength spectra of reflected light. Thus, wavelength resonance is measured as the sensor output. This scheme fits well with nanohole array sensors, described in section 3.3.

Intensity modulation In such SPR sensors, both the angle of incidence and wavelength are fixed, and the intensity of reflected light wave serves as a measurement of coupling between light and surface plasmons.

Phase modulation As for the intensity modulation, angle of incidence and wavelength are fixed. Here phase shift of the light wave is measured as output.

Among these different modulation schemes, the angular and the wavelength modulations are most frequently used in SPR sensors due to their high resolution and relatively simple experimental setup.

In order to obtain a biosensor, in addition to a SPR device which reveals refractive index variations, previously called transducer, it is necessary also a selective biorecognition element, a receptor which specifically interacts with the selected analyte. Biorecognition elements consist of probe molecules fixed on the surface of the SPR device during a step called fuctionalization. Thus the analyte, usually in liquid solution in contact with the interface of SPR sensor, binds with the bio-receptors increasing the refractive index at the interface (organic compounds have bulk refractive index $n \sim 1.5$, higher than ~ 1.33 of water or air ~ 1).

In addition to receptor-analyte binding, it could occur non-specific bindings of other compounds to the sensor interface, thus generating a false signal output. In order to avoid non-specific bidings also a protection coating is deposited to the sensor surface. New surface fuctionalization strategies were developed in order to provide to the SPR sensor both the bio-receptors for a selected analyte and the protection against non-specific binding [39].

Such a device is called an *affinity biosensor*, and its overall performance depends on both the optical characteristics of the SPR sensor and the performance of the surface functionalization.

Optical performance of SPR sensors is mainly described by their sensitivity and resolution.

Sensitivity Sensor sensitivity S is defined by the ratio of the change of the sensor output dY to the change of refractive index of the sensed medium dn

$$S = \frac{dY}{dn}. \tag{3.1}$$

dY depends on which modulation is employed and represents, for example, the shift of angle or wavelength resonance while dn is RIU (Refractive Index Unit). Sensor sensitivity can also be evaluated in terms of a figure of merit (FOM), taking into account the width of the resonance. Thus, FOM is defined by

$$\text{FOM} = \frac{S}{\text{FWHM}} \tag{3.2}$$

where FWHM is the full width at half maximum of the resonance.

Definition in eq. 3.1 is called bulk sensitivity. A more accurate definition of the sensitivity takes into account the fact that the changing in the refractive index occurs only within a layer of the dielectric much thinner than the penetration depth of the surface plasmon.

Resolution Sensor resolution is defined as the smallest change in the bulk refractive index that can be detected as a change in the sensor output. It is mainly determined by the noise in the sensor instrumentation.

Limit of detection While resolution refers to a bulk change, limit of detectio (LOD) is defined as the smallest surface concentration of the analyte that can be detected by the biosensor. Tests can be done with different concentrations of analyte and variations of the signal output can be plotted. From such a graph it is then possible to find the limit of detection.

In the next section two types of SPR sensors will be presented: firstly, a prism-based sensor with angular modulation and secondly nanohole array sensor with wavelength modulation.

3.2 Sensors based on prism couplers

Prism-based sensor is the most commonly used in SPR sensing tecnology for real-time monitoring of biological interaction [40]. It mainly consists of a high refractive index glass prism with a thin film of gold ($\sim$ 50 nm) deposited on its base. Thus, a Kretschman configuration is obtained and surface plasmons can be excited at the interface between gold and the surrounding dielectric, as described in section 1.3.1.

A commercial sensor based on such scheme is, for example, Biacore© which is commonly used for sensing antibodies, antigens, DNA and other analytes [41]. Figure 3.1 presents the working scheme for such biosensor. Bio-receptors are immobilized on the gold interface of the sensor and a solution of analyes flows in contact with this surface.

A TM-polarized monochromatic illuminates the prism and thus the interface prism-metal with a specific incidence angle and a dip is observed in the angular spectrum of reflected light, corresponding to the plasmonic resonance.

Further, functionalization and then analytes binding yield shifts of the minimum in the spectrum towards higher angles and it can be measured from the angular spectra, as seen in figure 3.2. It can be observed that refractive index increases until saturation and this occurs either when all receptors binded with analytes or, viceversa, when all the analytes binded with receptors.

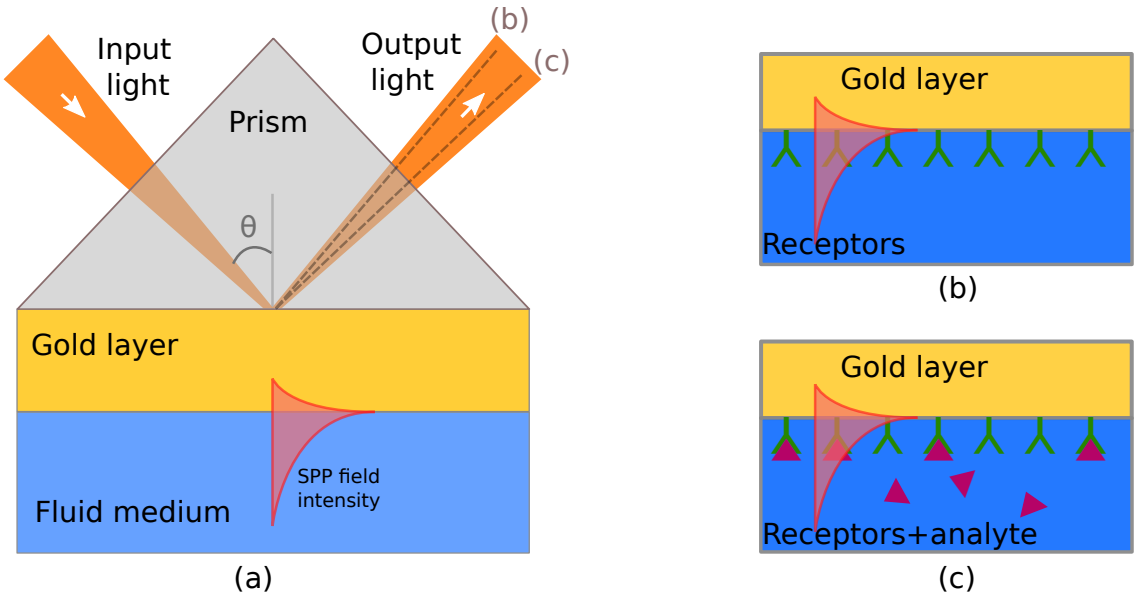

Figure 3.1: (a) Excitation of surface plasmons by Kretschman prism-coupling method. (b)Functionalization of the surface with bio-receptors. (c)Binding of receptors with selected analyte. Dashed lines in figure (a) correspond to the angular position of the minimum respectively in the configurations (b) and (c), in order to stress their shift.

Using commercial prism-coupling biosensors it is possible to monitor angular variation of order of 0.01° thus revealing low-concentration analyte down to a limit of detection of order of 10 pM with sensivitities down to $10^{-7} RIU^{-1}$ [42].

Angle-modulated SPR biosensors can also used to develop miniaturized portable biosensor, integrating all electro-optical components in a monolithic platmorm. Firstly conceived by Texas Instruments in the mid-1990s [43], compact and portable SPR sensor platforms were then developed [44] yielding the ability of a real-time high-sensitivity sensing.

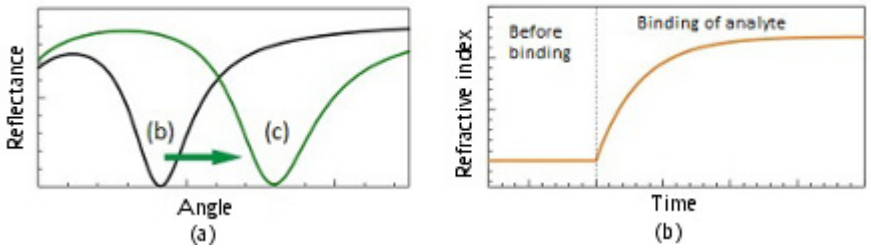

Figure 3.2: (a)Angular spectra for the configurations (b) and (c) from figure 3.1. Shift of the resonance angle can thus be measured. (b)Change of refractive index in time. During the flat part there are no binding events since there is no analyte. When analyte flows, refractive increases until saturation.

3.3 Nanohole arrays

3.3.1 Transmission and reflection mode for nanohole array sensors

Thin metallic films patterned with a nanohole array also support surface plasmons excitation due grating coupling, as described in section 1.4, and the resonance condition for plasmon excitation depends on refractive index of the surrounding medium. Therefore even nanohole arrays can be used as refractometric sensors, utilizing the same detection principle as in the prism-coupling SPR sensors [45]. The main advantage of such a grating-coupling sensor is that it can be both interrogated in reflection or transmission mode and, moreover, geometric characteristics of the structure can be tailored to control the characteristics of the plasmons.

The same interrogating setup of the prism-coupled sensor can be used for reflection mode measurements with NHA sensor. Angular interrogation measurements with monochromatic light could be done to observe the shift of minimum reflectance angle. Nevertheless, in most cases, periodic plasmonic structures are illuminated with white light at fixed angle (mostly normal incidence) and wavelength interrogation is done by measuring transmission spectrum.

Using nanohole arrays in trasmission allows the extraordinary optical transmission (EOT) phenomenon at particular wavelengths, and this is revealed as a maximum peak in the transmittance spectrum [46]. As analyte molecules are adsorpted on the surface of the nanohole array, changing the refractive index at the surface and thus altering the resonance condition, transmission peak wavelength should redshift and so analyte-receptor binding events are revealed. The very first report on biosensing with nanohole arraye was the refractometric detection of protein adsorption by Brolo et al. [47].

In figure 3.3 a scheme of the experimental setup and of the measuremets for a NHA-based sensor are outlined. The arrangement in figure 3.3a consists of a white light beam that illuminates the functionalized NHA with a fixed angle of incidence θ. Wavelength interrogation can be done in two ways. Firstly, reflected light could be detected and the dip in wavelength spectrum, that correspond to the plasmon excitation, could be

monitored. Also wavelength spectra for the transmitted light could be measured and in this case EOT peak wavelength could be used as output signal to observe binding events. In figure 3.3b measurement strategy are shown. From transmission spectra redshifts of EOT peak wavelength is observed, as analytes bind to receptors. In addition it is shown that with the same setup it is possible also to perform intensity interrogation. In this case, a monochromatic light beam is used and changing in the transmitted intensity is monitored. The size of the transmittance represents the strength of coupling between light, so observing a fixed wavelength above the resonance λ, as in the figure, binding events are revealed as an increase of the transmitted light.

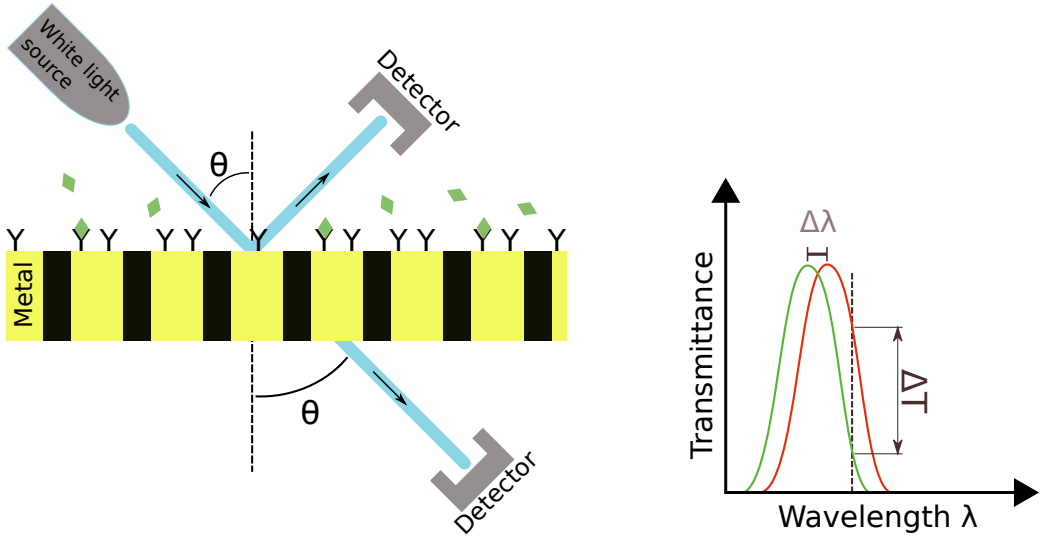

(a) Scheme of the experimental setup used for NHA-based sensor, where angle θ is fixed.

(b) Schematic of transmission measurements.

Figure 3.3: Scheme for NHA sensor

In contrast to commercial prism-based SPR, which needs an accurate control of the incidence angle, optical setup for NHA-based sensor becomes simpler if zero-order transmission, that is normal incidence on the surface of the NHA, is interrogated. Due to the simple optical setup, which consists of a source of white light normally incident to the NHA collinear to a spectophotometer, this is the most common setup which is suitable for miniaturization. Development of integrated biosensors in laboratory-on-chip device was showed by De Leebeeck et al. [48], integrating NHA arrays in microfluidic devices.

Figure 3.4 presents the setup for a sensing device used by Gordon et al. [46]. Solutions are delivered to the sensor interface by microfluidic channels, then white light from halogen source impinges normally the sensor and it is collected on the other side by a collinear fiber optics. Thus transmission spectra can be measured and peak shifts can be monitored.

Many label-free sensors using nanohole arrays were then developed to point out that they represents an efficient alternative to the standard prism-coupling SPR sensors, reaching comparable performances. Two examples of employment of nanohole arrays in two important domains, medicine and public health are presented here.

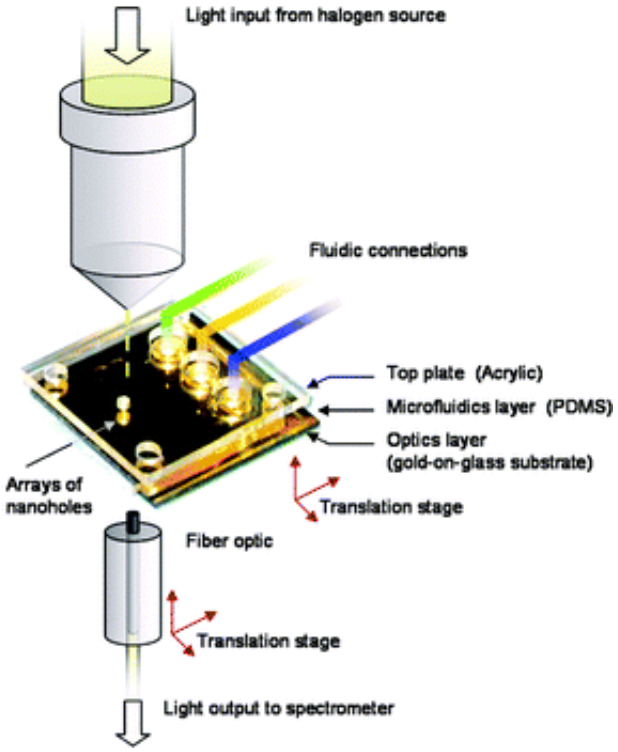

Figure 3.4: Experimental setup for the sensing device. Microchannels drive the solution to the interface and then transmission spectra are measured and EOT peak is monitored. [46].

S. Cho et al [49] demonstrated the detection of malaria pathogen in a whole blood lysate through antibody-antigen interactions at a nanohole array surface. Wavelength modulation and transmission measurements were employed and a refractive index sensitivity of 378nm/RIU was found. A nanohole array with 200 nm hole diameter, 300 nm periodicity and 100 nm thicknes was used, delivering to its surface pure water with different concentrations of glucose and rinsing after each measurement. Since refractive index of glucose solution has a well-known equation [50], sensivity was then calculated and performances comparable to prism-coupling sensor were obtained.

J. Briscoe et al. [51] developed a nanohole sensor to reveal the presence of microcystin-leucine-arginine (MC-LR), a hepatotoxin released by cyanobacteriae which pollutes the water. Transmission mode was used and the EOT resonance peak was tuned to 720 nm by fabricating a nanohole array with 500 nm periodicity, 250 nm hole diameter and 100 nm thickness. Sensing measurements were done through intensity interrogation mode at a fixed wavelength (710 nm) and thus a 10 pM/L limit of detection is demonstrated, better than commercial prism-coupling SPR sensor which showed for MC-LR a limit of detection of 73 ± 8 pM/L[52].

3.3.2 Flow-through nanohole sensing

Most of NHA synthesis techniques creates a nanohole array on a transparent substrate for an employment in sensing, and analyte solution is flown on the interface between NHA

and surrounding medium. Thus, the binding kinetics of an analyte to a functionalized sensor surface is determined by diffusive transport to the surface. As several techniques to create free-standing nanohole arrays were reported [7], this offers the advantage that the flow of analyte solution could be directed through the sensor surface. Analyte is then forced to flow very close to the recognition elements and this enhances the efficiency of binding with receptors [53]. However it is harder to achieve high flow rates due to the high fluidic resistance in nanoscaled channels and enhancement in signal will only occur for analyte-receptor interactions that do not reach the equilibrium (i.e. equal binding and unbiding rates) during a certain time. Once the equilibrium is enstablished there is no need to deliver more sample solution to the sensing surface. Research of Eftekhari et al. pointed out a refractive sensivity of 324 nm/RIU flowing glucose solutions through a 500 nm periodicity nanohole array [54], similar to the sensivity of equivalent flow-over nanohole array sensor.

3.3.3 Nanohole-enhanced spectroscopy

In addition to refractometric detection other optical sensing techniques are also possible employing plasmonic nanoholes array, such as molecular spectroscopy.

Raman spectroscopy is a vibrational spectroscopic method that has the inherent ability to distinguish between molecules with great similarity. It relies on Raman scattering, that is the inelastic scattering of a photon from a molecule. When a photon is absorbed by a molecule, usually Rayleigh scattering takes place and photon is re-emitted elastically with the same energy. If photon has proper frequency it can interact with the vibrational modes and then it can be re-emitted with an energy shifted up or down. These energy shifts give information about vibrational modes and thus can be considered as fingerprints of the molecule itself. Due to the low cross-section of Raman scattering compared to the elastic one high laser powers and long acquisition times are usually required to achieve high quality Raman spectra.

Higher intensity Raman signals and lower detection limits can be achieved using Surface Enhanced Raman Spectroscopy (SERS) [55]. To this aim, the electromagnetic field of surface plasmon, which are tightly confined to the surface of the nanostructure, results suitable to increase the intensity of Raman signal from molecules near to the interface. If resonance wavelength is close to the wavelengths of both incident light and Raman signal, high enhancement is gained. Since nanohole array geometry can be tailored to get EOT peak at the desired wavelength, they represent a promising platform for SERS [56, 30].

Figure 3.5 shows the use of nanohole arrays as a substrate for the Raman scattering of oxazine 720 molecule in transmission mode. Measurements using arrays of different periodicities were done and it was pointed out that best Raman signal is acquired as plasmonic resonance approaches the vibrational modes.

The distinct advantages of SERS, such as low detection limit, real-time response, both qualitative and quantitative analysis capabilities, a high degree of specificity, and simultaneous multi-component detection, make it applicable in identifcation and characterization

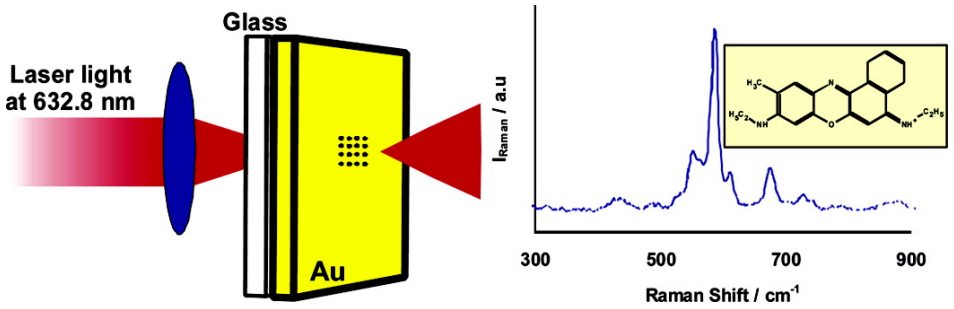

Figure 3.5: Optical arrangement and signal output for enhanced-Raman spectroscopy of oxazine 720 molecule [56].

of pharmaceuticals, bacteria, and other molecular species [55]. Moreover SERS biosensors are used to reveal pathogens that are connected to different tumors and Alzheimer's or Parkinson's diseases [57].

3.4 1D grating-coupling sensors

Another valid alternative to the prism-coupling sensor is represented by one dimensional gratings that provide the missing wavevector to obtain plasmon resonance. Multiple type of gratings can be used for this purpose and in section 1.3.3 sinusoidal grating was briefly introduced and coupling conditions were showed. In figure 3.6 profile of metal layer are drawn for a sinosoidal grating (a), and for a digital one.

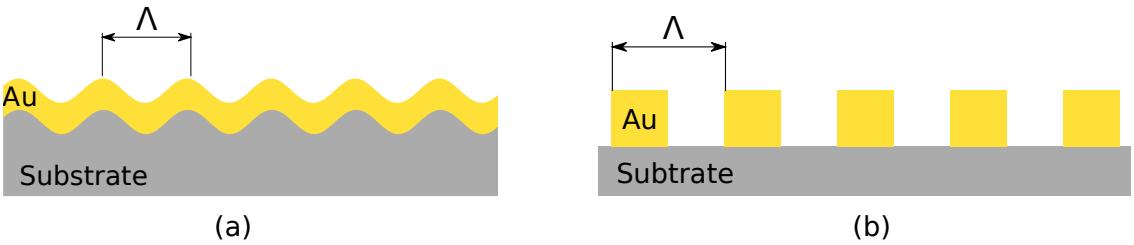

Figure 3.6: (a) Sinosoidal grating with Λ periodicity. (b)Digital (also called lamellar) grating. It can present EOT phenomenon since plasmon can be excited on the top surface of the metal wires and re-emitted on the other side.

Both structures here depicted can be employed, similary to the nanoholes, for sensing purposes, once their interface is functionalized with specific bio-receptors.

A label-free high-sensitivity biosensor was obtained recently with a gold sinusoidal grating for the detection of some of the mutations responsible for Cystic Fibrosis [58]. Interaction between DNA target and complementary DNA receptor are monitored using reflectivity measurements by ellipsometry at a fixed nonzero azimuth angle α between grating vector and incidence plane. Two dips in reflectance spectrum are observed in this case, corresponding to the plasmon excitation. While for null azimuth case TM polarization is optimal, with a nonzero azimuth polarization must be optimized in order to get deeper minima in the spectrum and thus better signal output. The measured sensitivity of such

a sensor is of order of 600 - 800°/RIU, higher than the one obtained with prism-coupling sensor (50 - 150°/RIU).

A digital grating was employed to develop a sensor for the detection of self-assembled monolayer of thiols [59]. Such a nanostructure presents extraordinary optical transmission phenomenon, like nanohole arrays, and so interrogation is done through transmission mode. Accurately aligned light beam incides normally on the grating, with a certain polarization, and zero-order transmission spectra are measured by photodiodes on the other side.

Chapter 4

Results: Numerical Simulations

To design and model the nanostructures synthesized in this work numerical simulations were carried out using COMSOL Multiphysics® software in order to predict the properties of the nanohole array. Thus, the near-field electromagnetic response and the far-field transmission of such NHA were simulated by finite element (FEM) analysis in the frequency domain.

First, the morphology of the NHA was investigated and transmittance spectra were simulated with different geometrical parameters. The environment consisted of air ($n_{air} = 1$) above the nanostructure and silica ($n_{SiO_2} = 1.45$) as a substrate. Two free parameters were investigated, the thickness of the Ag layer t_{Ag} and the hole radius R, while periodicity and thicknesses of the Ti and Au layer were fixed, respectively, to 522 nm, 5 nm and 10 nm. Thus, the optimal parameters were found and then they were employed both for simulations and experimental work.

The incident electric field was polarized along the <1,0> lattice direction, but also a <1,1> polarized electric field was simulated in order to check if polarization can affect the optical properties. Moreover a check-test was done by replacing titanium layer with a chromium one for the adhesion and, finally, the bulk and local sensitivity of the NHA was evaluated.

The bulk dielectric constant $\epsilon(\omega)$ of the metals were measured by ellipsometry on thin films and then used for the simulations.

4.1 Far field transmission spectra

4.1.1 Morphology investigation

Transmittance spectra were simulated first fixing the radius R to 145 nm, with different silver layer thicknesses, 45 nm, 90 nm and 135 nm. Then, different radii, 120 nm, 145 nm and 170 nm were simulated with the silver layer fixed to 45 nm. The simulated spectra are presented in figure 4.1. It can be observed that higher metallic layer yields a narrow peak but EOT peak intensity is reduced. Since higher transmission is needed, Ag layer thickness was fixed to 45 nm. Once fixed t_{Ag},it can be observed that EOT peak intensity

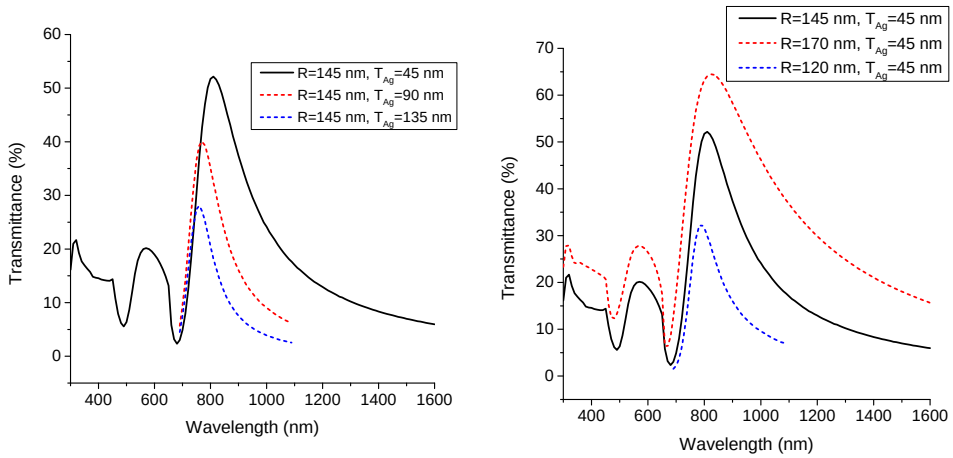

(a) Different t_{Ag} with fixed R.

(b) Different R with fixed t_{Ag}.

Figure 4.1: Spectra with different morphological parameters. Solid lines represents the optimal parameters

increases for larger hole diameters but it also broadens. On the other side holes with smaller diameter yield a better-defined peak but the transmittance is reduced. Therefore, the halfway diameter was chosen and so a 45 nm thick Ag layer and a 145 nm hole radius were used in the subsequent simulations.

4.1.2 Adhesion layer

Once morphology was fixed, transmittance, reflectance and absorption for a NHA with Cr and Ti adhesion layer were calculated and presented in figure 4.2. The transmittance and the reflectance are calculated considering the ratio between the intensity of, respectively, the light that passed through the NHA in far-field and the light that has been reflected backward, and the intensity of the incident radiation. On the other hand the absorption is calculated as the internal losses of the electric field in the metallic film. There are no significant differences between the optical properties of the two NHAs.

In figure 4.3a, the simulated transmittances of the NHA with different adhesion layers are compared to an experimental spectrum with Ti layer and main characteristics of the EOT peak are presented in table 4.1.

Sample	Centroid(nm)	FWHM (nm)	λ_{max}(nm)	T_{max}	λ_{min}
Exp-Ti	966	416	919	55.6	698
Ti	865	270	830	49.4	690
Cr	867	250	840	50.3	690

Table 4.1: Characteristics of simulated and experimental spectra for the <1,0> EOT peak.

It is clear that there is no significat difference between the two simulated spectra and therefore the use of Cr or Ti for the adhesion layer leads to unimportant consequences. Both

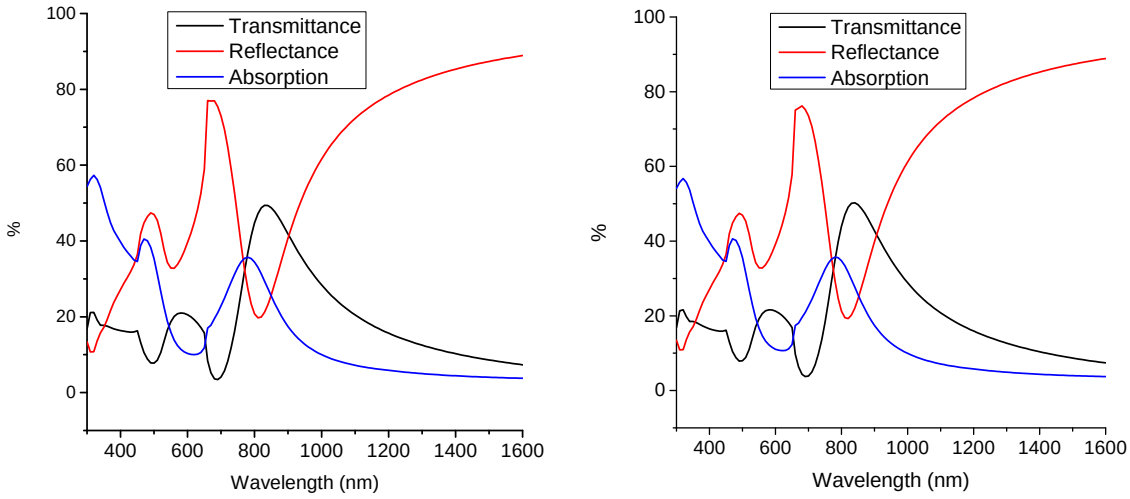

(a) Ti adhesion layer

(b) Cr adhesion layer

Figure 4.2: Simulated transmittance, reflectance and absorption of a NHA with different adesion layer between the substrate and the Ag film.

simulated peaks are slightly shifted to lower wavelengths with respect to the experimental one. On the other hand, this simulation well reproduces the experimental transmittance and this is stressed also by the fact that the minima of transmittance occur at about the same wavelengths, as shown in table 4.1. Therefore, for the subsequent simulations, as far in the experimental work, Ti adhesion layer was used.

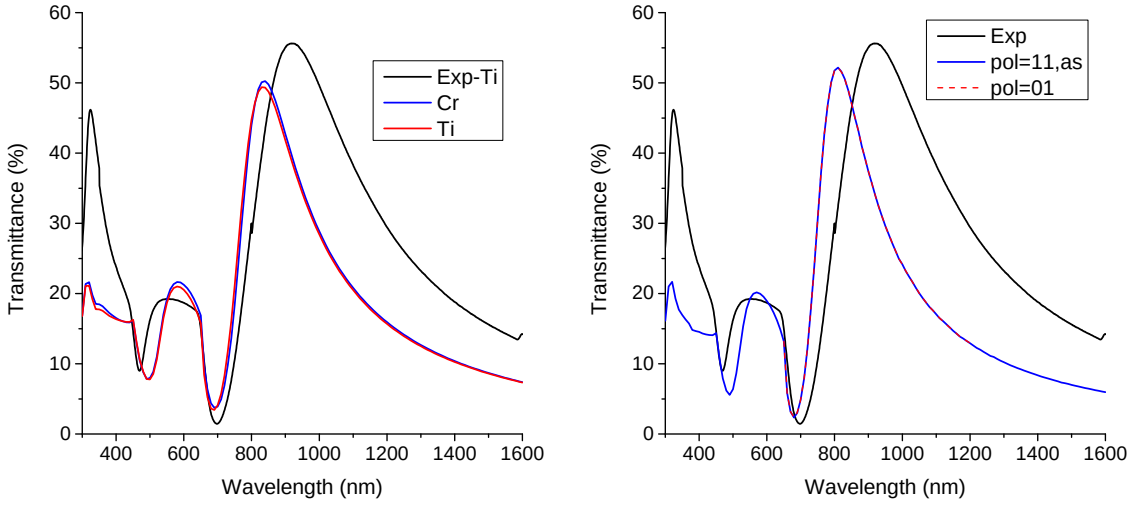

(a) Comparison between experimental transmittance and the simulated ones with Ti and Cr as adesion layers.

(b) Experimental transmittance measured vs. simulated transmittances of the electric field with <1,0> and <1,1> polarizations.

Figure 4.3

4.1.3 Polarization

The dependence of the transmittance on the polarization of the incident radiation was checked by carrying out simulations using two different polarizations, along <1,0> and <1,1> lattice directions. As shown in figure 4.3b there is no difference between the two simulated curves and, therefore, different polarizations do not produce any change in the optical transmittance of a nanohole array. This allows to employ in the experimental work non-polarized light. For further simulations, the incident electric field was considered polarized along the <1,0> direction, that is with a null component along y-axis and a non-null along x-axis.

4.2 Near-field response

There are two components of the electric fields that are non-null in the near-field for x-polarization, the incident E_x and E_z field that is excited due to plasmon resonance.

Figures 4.4 and 4.5 present the transmission through the hole of E_x field for two specific wavelengths, λ_{max} that is the EOT peak and λ_{min} that corresponds to the minimum transmittance. The yellow lines represent the flux of the Poynting vector, that is the energy flux density of the plane-wave electric field that impinges the hole.

In case of the extraordinary transmission, it is clear from the figure how field lines don't extinguish within the hole but they curve and pass through it. On the other side, after a short distance ($\sim 300nm$), the plane wave of the electric field is quickly reconstructed and it propagates in far-field. On contrary, in case of the minimum transmittance, most

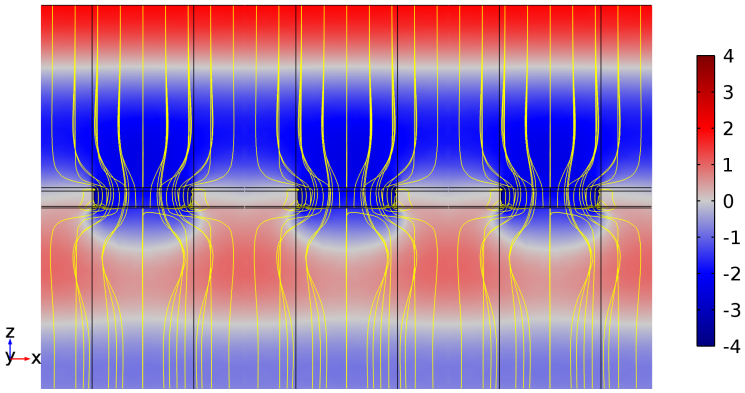

Figure 4.4: Transmission of E_x through a nanohole at λ_{max} wavelength of <1,0> EOT peak.

of the flux lines of the Poynting vector pass through the hole but extinguish quickly at the output interface. Therefore a very low intensity field is transmitted in far-field.

A field E_z is generated due to plasmonic resonance on both, top and bottom, interfaces. In figure the 4.6a field E_z at the top interface (NHA/Air) is plotted and a similar field, but with inverted signs, are found on the bottom interface. It is clear that localization of the field occurs at the rim of the holes, thus enhancing the transmission in far-field of the field E_x. While incident field E_x is set to 1 V/m, a near-field enhancement is observed

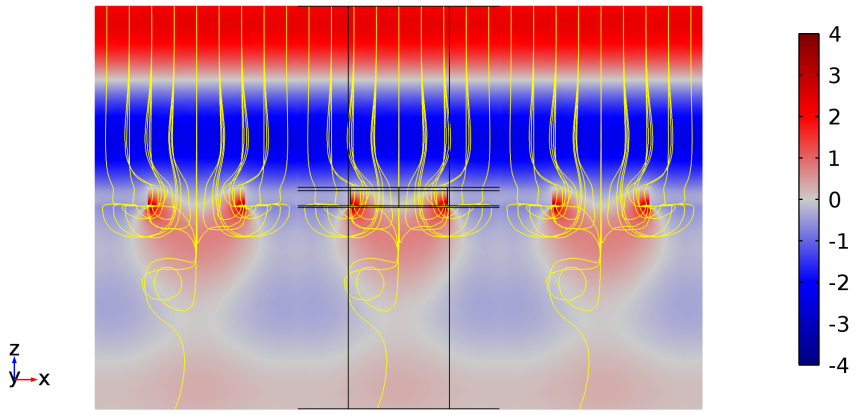

Figure 4.5: Transmission of E_x through a nanohole the λ_{min} wavelength.

since modulus of E_z at the NHA interface rises up to 5 V/m in the hotspots. In figure 4.6 the field E_z is plotted against the distance z from the interface, both for top and bottom sides. The two curves are then fitted with an exponential decay function so the two decays lengths (δ_{air} and δ_{SiO_2}) are found, that represent the height at which electric field is a $1/e$ fraction of the field at 0 distance.

$$\delta_{SiO_2} = (53 \pm 3)nm \qquad \delta_{air} = (38 \pm 2)nm \tag{4.1}$$

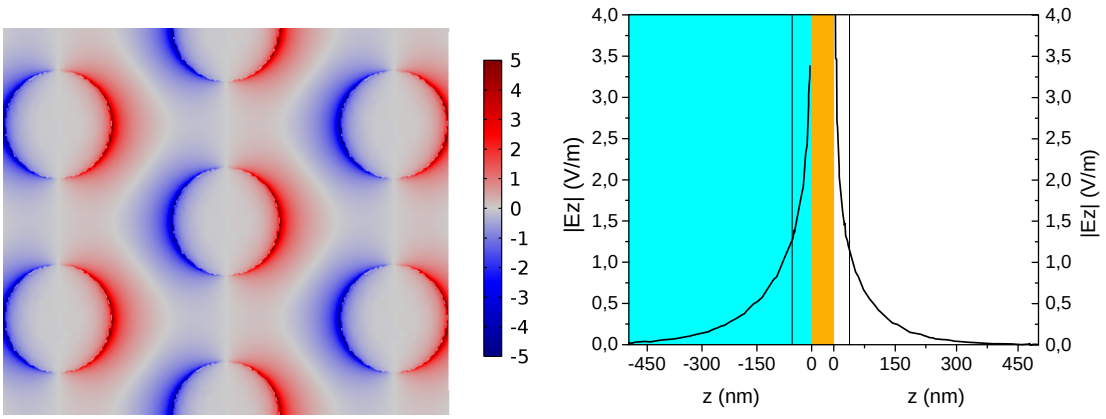

(a) Colour plot of E_z component of the outer surface of the NHA from a top-view.

(b) E_z decays as distance from interface increases. The vertical lines point out the decay lengths δ of E_z.

Figure 4.6: E_z field plots

So far, the electromagnetic fields external to the metallic NHA were described. In figure 4.7 internal electric behaviour is depicted by showing the flux of the current density of electrons inside the metal, at the top interface. Arrows points out that density current is not localized arround a single hole, but there are current lines that link adjacent holes.

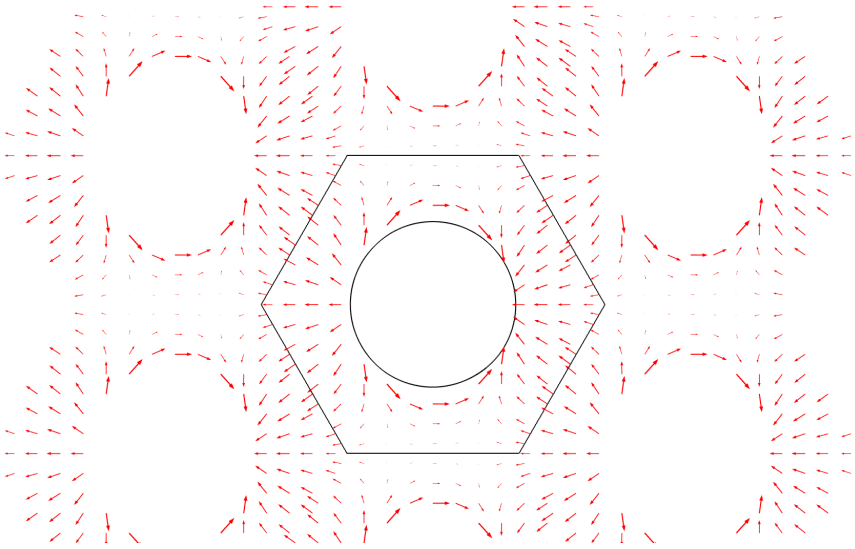

Figure 4.7: The current density lines at the top interface of the metal.

4.3 NHA sensitivity simulation

4.3.1 Bulk sensitivity

In order to evaluate the bulk sensitivity of the NHA as optical biosensor by simulation, the environment on the nanostructure is modified, replacing the air above the NHA with water, that is an 1.33 refractive index instead of 1. The two transmission spectra are presented in figure 4.8.

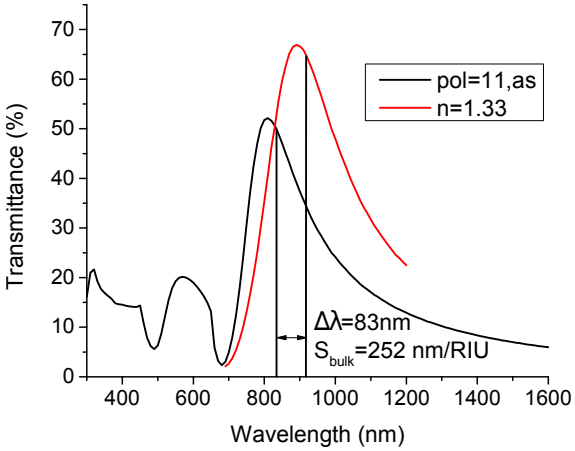

Figure 4.8: EOT peak with 1 and 1.33 refractive index media at top interface.

n	Centroid (nm)	λ_{max}(nm)
1	834	810
1.33	917	890

Table 4.2: Centroid and maximum wavelengths for bulk sensitivity.

After evaluating the shift of the centroid due to the refractive index (RIU) variation, the bulk sensitivity of NHA can be calculated and compared to the experimental one from section 6.2.1.

$$S_{bulk} = \frac{\Delta\lambda_{centroid}}{\Delta n} = 252\text{nm/RIU} \tag{4.2}$$

4.3.2 Local sensitivity

In order to evaluate the local sensitivity, i.e., the sensitivity to dielectric changes on thin layers at the NHA surface (cfr. section for a detailed description 6.2.2), simulations were carried out considering an additional layer of silica (n=1.45) of increasing thickness deposited on the NHA interface. Therefore, transmission spectra of the NHA with an additional layer of silica of 13, 26 and 39 nm thickness were simulated. In order to take into account the different deposition rates for vertical and horizontal directions (cfr. section 5.4.2), the silica layer added on the lateral surface of nanoholes was considered to be 1/3 of the one added on the top surface. The centroid of the EOT peaks are reported in the table 4.3. In figure 4.9 the centroid position are plotted against the thickness t and a linear fit with $y = m \cdot x + q$ yields:

$$q = 778 \pm 1nm \qquad m = 1.05 \pm 0.04$$

m represents the local sensitivity in presence of silica. The curve should follow an exponentially saturating function whose characteristic length scale is the near-field decay length from equation 4.1. Since the decay lengths are longer than the thicknesses of the dielectric layer, exponential curve can be linearized in this case and thus a linear fit can be done. The local sensitivity of the NHA is found by dividing by the variation of the refractive index between air and silica (1.45 - 1 = 0.45 RIU).

$$S_{loc} = 2.33 \pm 0.07 \text{ RIU}^{-1}$$

t_{SiO_2} (nm)	Centroid x_0 (nm)
0	777 ± 1
13	793 ± 1
26	805 ± 1
39	818 ± 1

Table 4.3: Centroids with different layers of SiO_2.

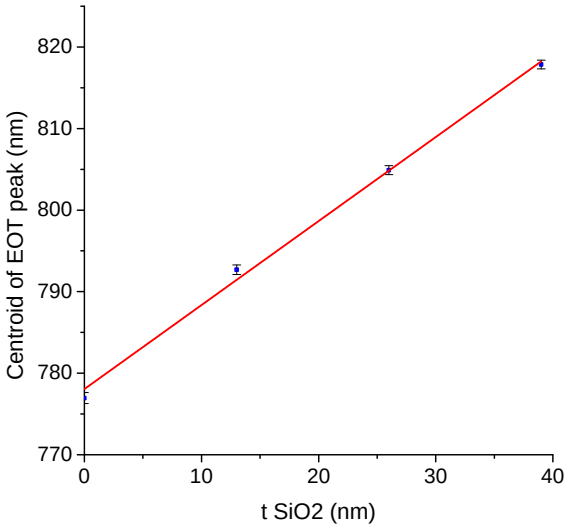

Figure 4.9: Centroid shifts as layer of silica rises.

Chapter 5

Results: Synthesis and characterization of nanohole arrays

5.1 Self-assembled masks

5.1.1 Synthesis

For the nanosphere lithography method, polystyrene nanoparticles from Microparticles GmbH were used, specifically, monodisperse nanospheres of diameter of 522±12 nm in acqueous solution. First a solution 1:1 of nanoparticle suspension and isopropyl alcohol (2-propanol) from Sigma Aldrich was prepared.

As described in the section 2.1 the mask synthesis can be mainly split in two steps, the immersion and the picking up of the mask. The substrates employed in this work were slabs of Soda Lime Glass (SLG), hyper-pure silica glass HSQ 300 or monocrystalline silicon wafer with <100> lattice orientation. SLG slabs were used only for the immersion while silicon and silica glass were employed as substrates for the self-assembled mask during the picking up.

Substrates were cut and placed in a carousel support made of teflon that holds them in vertical position in order to expose all the surface to the cleaning solution and to avoid overlapping of the samples during this step. First an acid piranha solution is prepared with 90ml of sulfuric acid (H_2SO_4) and 30ml of hydrogen peroxide (H_2O_2). The carousel and the substrates are immersed and left in solution for one hour at a temperature of 90°C on a heating plate. Then substrates are pulled out and thoroughly rinsed with Milli-Q water. A second carousel is used to immerse substrates in a basic piranha solution prepared with 90ml of ammonium hydroxide (NH_4OH) and 30ml of hydrogen peroxide for 20 minutes at a temperature of 90°C. Hereafter the substrates are rinsed with Milli-Q water and then, once dried with air flow, they are ready for the self-assembly process.

The motorized dipper used for the immersion, schematically depicted in figure 2.1, is shown in figure 5.1. The SLG substrate is fixed to the end of the T-shaped arm. The baker is filled with Milli-Q water and a small amount of solution of nanospheres, previously prepared, is dropped on top of the SLG substrate so the solution spreads over

all the surface. Using the remote-controlled arm, substrate is dipped into the water and nanoparticles form a floating close-packed mask on the surface. It is picked up, then, using a Si or SiO_2 substrate, held by tweezers and it is let to dry.

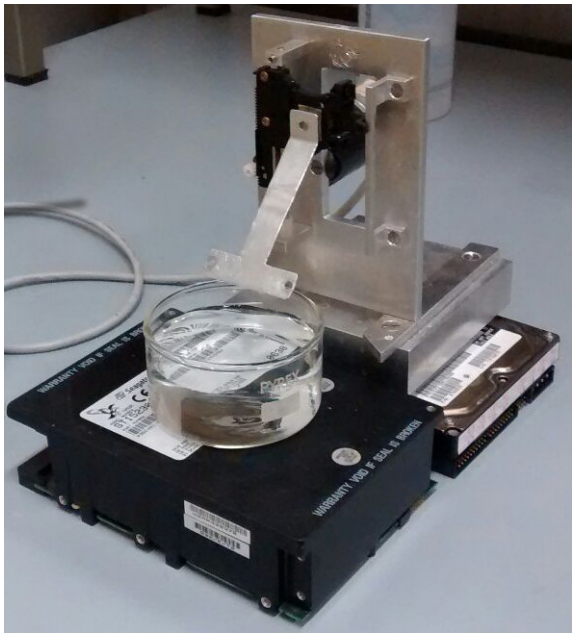

Figure 5.1: The mechanism employed for the self assembly.

This is a delicate process on which depends the quality of the final nanohole array sample. Multiple test were done to optimize production of well-ordered monolayer arrays of PS nanospheres. Different parameters were varied to get a reproducible protocol for nanosphere self-assembly:

Nanospheres solution Different concentrations of 522nm PS nanospheres in 2-propanol were tested, as 1:1, 1:2 and 3:4, and 1:1 solution produced best results. No ordered mask were formed with the other solutions.

Amount of solution on the substrate Using a micropipette, different volumes of solution were dropped on the SLG substrate, in a range from 10μL to 50μL. The largest masks were produced with 20μL. Using less solution, no mask were formed.

Water temperature Another important parameter is the water temperature in the baker. Using cold water (4°C), small masks formed, while using water at room temperature (20°C) larger masks were achieved but any perturbations easily ruined them. Filling the baker with half cold and half warm water (i.e., at about 12°C), larger masks were formed.

Mechanical perturbations Attention must be paid not to hit the support of the motorized dipper, since any small perturbation could ruin the floating mask.

Drying Once the mask is carrefully collected on the desired substrate, it is let to dry in vertical position, since better order was observed rather than horizontal drying.

5.1.2 Characterization

In order to check the quality of the masks, two types of measurements were done, optical and morphological. Optical measurements were done using a *Jasco V-670 UV-VIS-NIR* spectrophotometer, by illuminating the sample with normally incident non polarized light. Morphological characterizations were done by Atomic Force Microscopy (AFM) employing *NT-MDT Solver PRO-M* microscope and by Scanning Electron Microscopy using *Zeiss SIGMA HD SEM-FEG* microscope. The absorbance spectra of the PS nanospheres masks were acquired, as in figure 5.2. The absorbance A is linked to the transmittance T (in percent) by the following relationship:

$$A = 100(2 - log_{10}(T)) \tag{5.1}$$

where both quantities are expressed in percent. In the NIR range (specifically for $\lambda \gtrsim$ 700 nm) the mask is almost transparent to the radiation ($A \lesssim 1\%$), but the absorbance increases quickly as λ decreases. The spectra present a sharp peak at about 650 nm, and its width is linked with the overall degree of order of the mask. Therefore a narrow peak suggests a well-ordered mask.

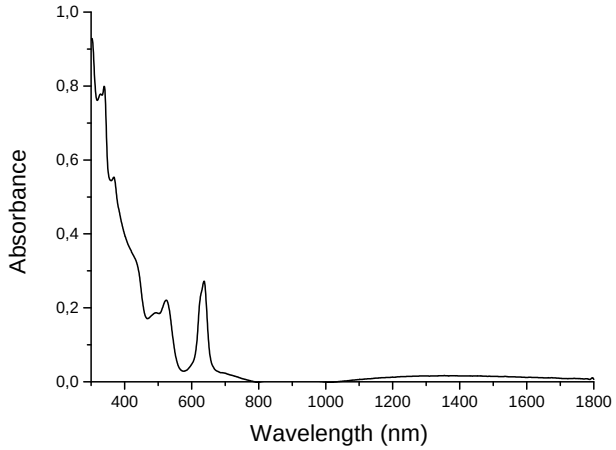

Figure 5.2: Absorbance spectrum of a 522 nm PS nanospheres monolayer mask on silica.

More specific details about the morphology of the mask, but focused on a small area of the sample, were acquired by SEM and AFM microscopies. Figure 5.3 shows a SEM image of a mask produced by PS nanospheres of diameter of 522 nm.

Figure 5.4 shows an AFM image of a mask, and its Fast Fourirer Transform (FFT) calculated by Gwyddion software. The presence of a hexagonal lattice of spots in the FFT image, representing the reciprocal lattice, suggests a well ordered array in the direct space.

These images show that the self-assembly of PS nanospheres allows to produce well-ordered monolayers.

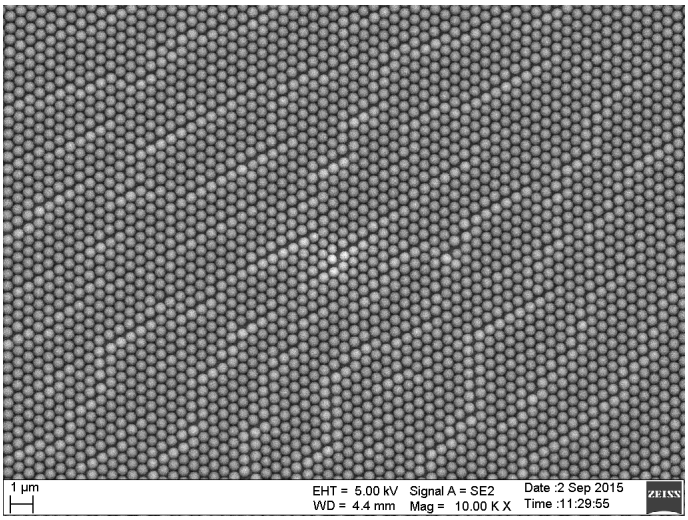

Figure 5.3: SEM image of a typical PS nanosphere mask

5.2 Reactive Ion Etching

While the periodicity of the nanohole array is determined by the nanosphere diameter, during this step the hole diameter is chosen by etching the polystyrene nanoparticles in a reactive atmosphere of O_2 and Ar mixture, as described in detail in section 2.2. The optimal technical parameters were found to be work a pressure of $9 \cdot 10^{-3}$ mbar a a ratio between oxygen and argon fluxes of about 3.1 (cfr. table 2.1), so the etching time is the only free parameter. Different RIE times were tested and a time calibration was done in order to control the etching rate, with the constraint that a nanosphere collapses if etched below approximately half of its initial diameter.

Four runs were performed for the calibration, at four different times: 6, 9, 12 and 15 min, respectively. The etched masks were observed bye FE-SEM and the average diameter for each etching time was calculated by analyzing the images with the ImageJ software.

Etching time (min)	Diameter (nm)	Etched diameter (nm)
0	522 ± 12	0
6	423 ± 5	99±13
9	360 ± 4	162±13
12	248 ± 8	274±14
12	268 ± 10	254±16
15	173 ± 11	349±16

Table 5.1: Diameter of PS nanospheres after RIE process.

A plot of the etched diameter against RIE time is presented in figure 5.5, and the data were fitted by a parabolic function $y(x) = bx + cx^2$. Parameters from the calibration fit are presented in the table 5.2. A narrow hole would reduce ordinary transmission so EOT phenomenon would be increased. On the other hand a long etching time could damage the

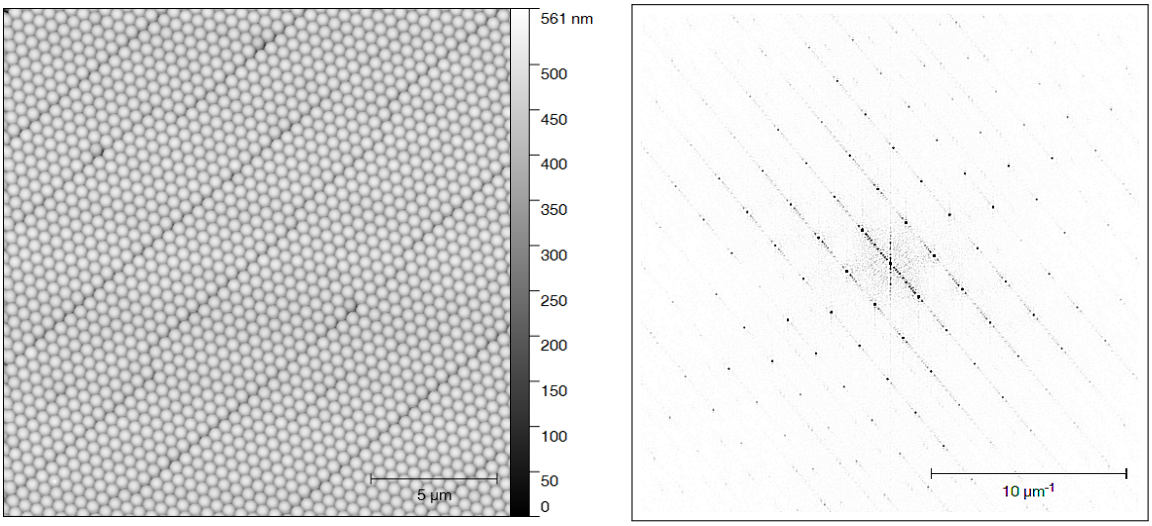

(a) AFM image of PS nanospheres mask.

(b) FFT image from the AFM image.

Figure 5.4: Images from AFM microscopy of PS nanospheres array.

nanosphere and make them to collapse. Moreover, for higher etching times, the surface roughness of the PS spheres increases, as can be observed in figure 5.6e, and this could compromise the final quality of the nanohole array.

b	$11.8 \pm 3.2 \text{nm/min}$
c	$0.80 \pm 0.22 \text{nm/min}^2$

Table 5.2: The parameters from the parabolic fit on data in figure 5.5.

Therefore an etching time of 12 minutes was chosen for the production of the masks employed for the synthesis of nanohole arrays, so the final diameter d of the etched spheres, and then of the nanoholes, was a little larger than half of the initial diameter D of the nanospheres ($d \gtrsim D/2$).

5.3 Metal deposition

In this step, the height of the NHA is tuned, that is the thickness t of the metallic film which is deposited through the masks. The NHA produced in the present work consisted of a three layers, Ti ($\sim$ 5-10 nm), Ag ($\sim$ 50-100 nm) and Au ($\sim$ 10-20 nm), deposited in sequence by Magnetron Sputtering. The employed sputtering system, described in section 2.3, has three sources (1 DC and 2 RF) and each can sputter one element. Thanks to an electronic-controlled rotating plate in the sputtering chamber, the sample holder could be fixed and rotated. This allows to put the sample holder in front of each source and then deposit one at a time the metals maintaining the vacuum in the chamber and increasing the collimation of the sputtered atoms with respect to the PS mask.
Therefore the deposition step, once the sources are ignited, is controlled by a script that

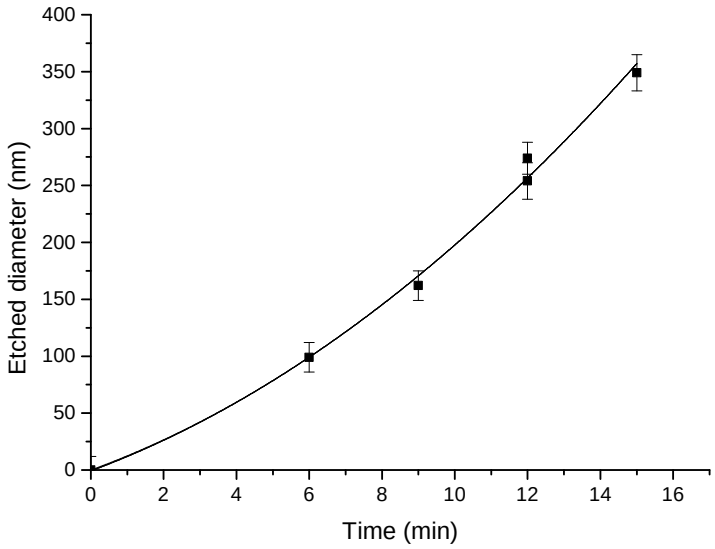

Figure 5.5: Plot of etched diameter against etching time. A point (0,0) was added to stress that diameter before the etching was 522±12. Parameters of the parabolic function are in table 5.2

moves the samples in front of the sources and sputters the metals in a computer-controlled sequence.

First the chamber is evatuated to a pressure below $3 \cdot 10^{-6}$ mbar then Argon flows in, increasing the working pressure up to $5 \cdot 10^{-3}$ mbar. The power of each source is set to the values reported in table 5.3.

Target DC	Target RF new	Target RF old
Ag	Ti	Au
20 W	50 W	20 W

Table 5.3: Power set for each sputtering source.

With these parameters the deposition rates for each metal were preliminarily calibrated obtaining 0.1 nm/s for Ti, 0.5 nm/s for Ag and 0.25 nm/s for Au respectively. Whem depositing more than one sample per proecss. When depositing more than one sample per process, the final film thicknesses were measured as a function of the substrate position on the sample holder. Indeed, since the source of sputtered ions from the target has a particular shape, that is a plasma ring eroding the target, the uniformity of the depositions has to be checked.

5.3.1 Source uniformity test

In order to check the uniformity of the source, 22 samples of silicon were cleaned by sonicating them first in acetone then in ethanol bath and then fixed on the sample holder.

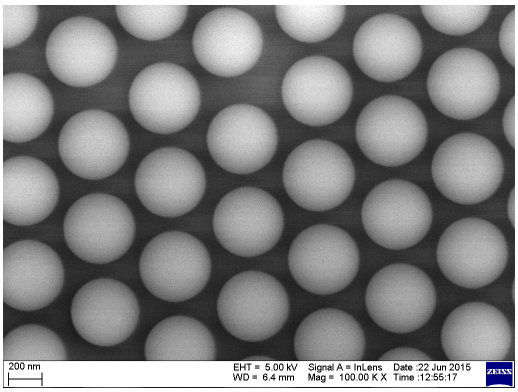

(a) RIE - 6 minutes

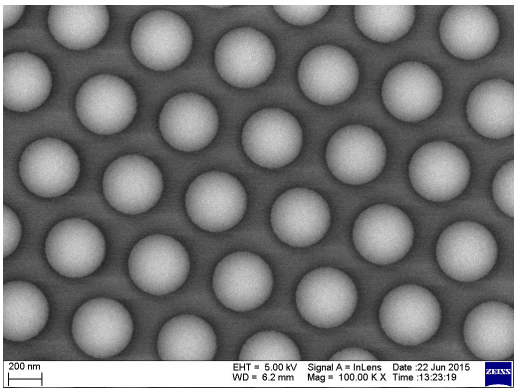

(b) RIE - 9 minutes

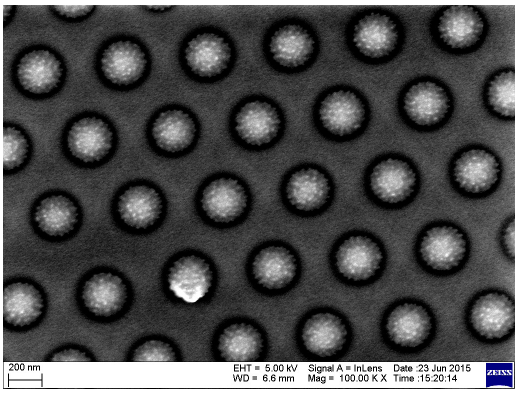

(c) RIE - 12 minutes

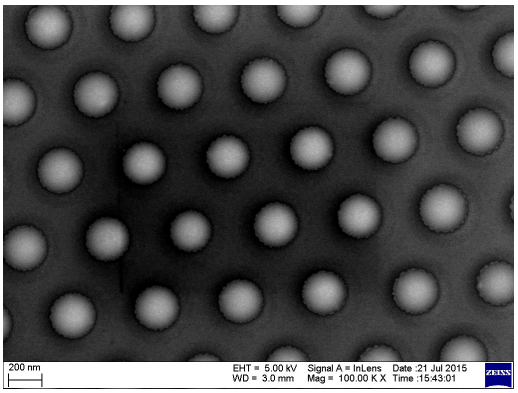

(d) RIE - 12 minutes bis

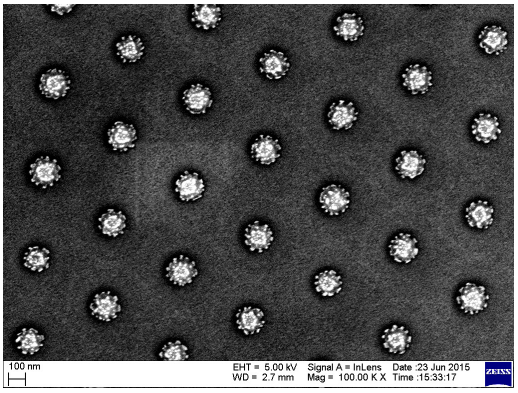

(e) RIE - 15 minutes

Figure 5.6: SEM images of polystyrene nanospheres mask after different RIE processes.

All the samples were signed by a marker in order to create an array and then their positions were measured. The sputtering time for each element was set in order to obtain a film with a nominal total thickness of 60 nm as follows:

After the deposition, the samples are cleaned in ethanol so the marker signs and metal above them were washed away leaving a groove. Its depth represents the thickness of

Ti	Ag	Au
50 s ≃ 5 nm	90 s ≃ 45 nm	40 s ≃ 10 nm

metallic film and AFM measurements of all the 22 samples were done and the thicknesses were then calculated by employing the Gwyddion software.

Using the height of each point and its coordinates on the sample holder, the map in figure 5.7a is obtained and it shows that the deposition is not uniform over the area of the plate. In figure 5.7b this is shown more clearly by a colour plot over the plate area. A hot spot is observed in the center of the probing area, where the height of the metallic film reaches 77 nm. Almost circular levels surround the maximum and the thickness decreases as the distance from the maximum rises. At the edge of the probing area the thinnest films are reported, with thicknesses down to 43 nm. Due to the difference between the heights of the film in different positions of the sample holder, the substrates were carefully positioned to obtain the best uniformity.

In order to produce nanostructures with same morphological characteristics, that is in a reproducible way, once the power of each source and the deposition time for each element are fixed, one should place the samples along the contour lines observed in figure 5.7b. Thus, films with the same thickness are deposited on different samples located in different positions on the plate.

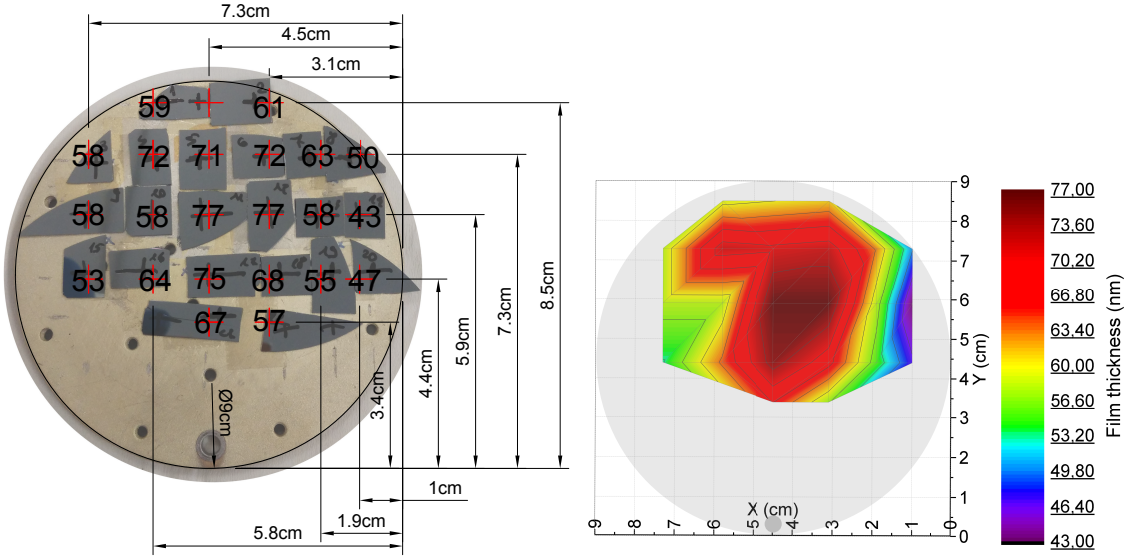

(a) A map of the film thicknesses on samples located in different positions on the sample holder.

(b) A colour plot of the map from fig.5.7a where also contour lines are shown.

Figure 5.7

5.3.2 Deposition for NHA

Different depositions were done through the masks to produce the investigated NHA. Attention must be paid to the height of the metallic film. The film must be thick enough

to be as opaque as possible for radiation in the range of interest (Vis-NIR), but too thick films could prevent mask removal, due to the clamping effect on the nanospheres or even the formation of a continuous film-over-nanospheres (FON) structure.

Two types of depositions were done, in order to produce either a 60 nm or a 70 nm thick film, with the following time parameters.

70 nm deposition			60 nm deposition		
Ti	Ag	Au	Ti	Ag	Au
50 s $\simeq$ 5 nm	100 s $\simeq$ 50 nm	60 s $\simeq$ 15 nm	50 s $\simeq$ 5 nm	90 s $\simeq$ 45 nm	40 s $\simeq$ 10 nm

Table 5.4: Time parameters for metal deposition.

Transmission spectra of both films were measured and they are shown in figure 5.8. Even if below 500 nm there is a considerable difference between the two transmissions, in the range of interest of this work ($\lambda > 800$nm) transmittances are both similar and below 2%.

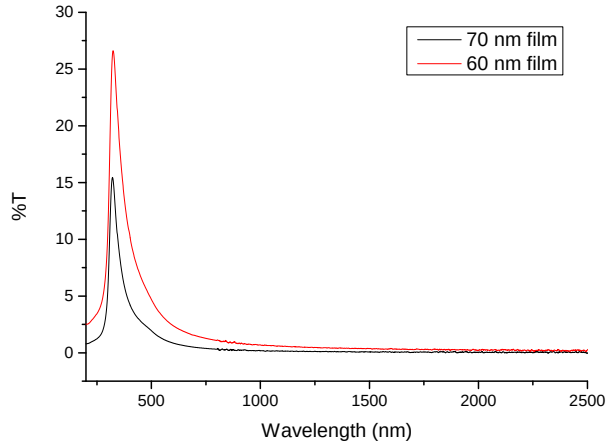

Figure 5.8: Transmission spectra of 60 nm and 70 nm metallic films

NHA samples were produced by depositing a 60 nm metallic film through a 12 minutes RIE-etched mask. The mask of PS nanospheres was then removed by sonicating the samples for 2 minutes in toluene bath. Such a metallic NHA sample is shown in figure 5.9.

Another test was done by depositing a 70 nm film on a 13 minutes RIE-etched mask. Such a film prevented the mask removal since PS nanospheres of the mask were trapped underneath the metal making it difficult, if not impossible, to remove the mask by toluene bathing. Figures 5.10 shows trapped PS nanospheres whose removal resulted impossible even by a 12 h toluene bathing.

5.4 NHA characterization

Multiple NHA samples were then produced by sputtering a 60 nm film (5 nm Ti, 45 nm Ag and 10 nm Au) on a 12 minutes RIE-etched mask on Si or SiO_2 substrates followed

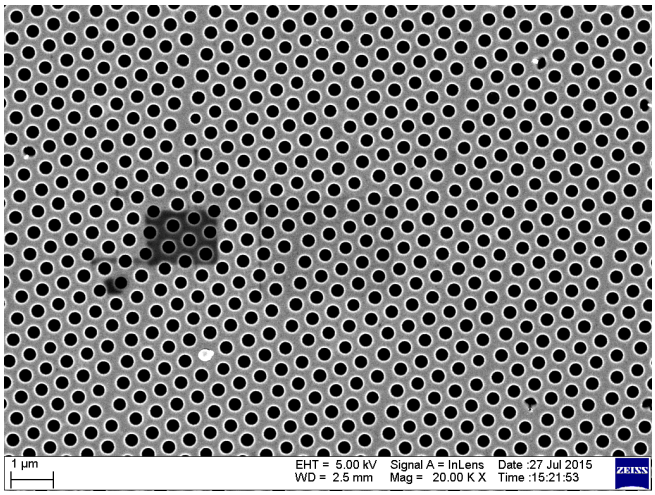

Figure 5.9: SEM image of NHA. 60 nm film was deposited through a 12 minutes etched mask.

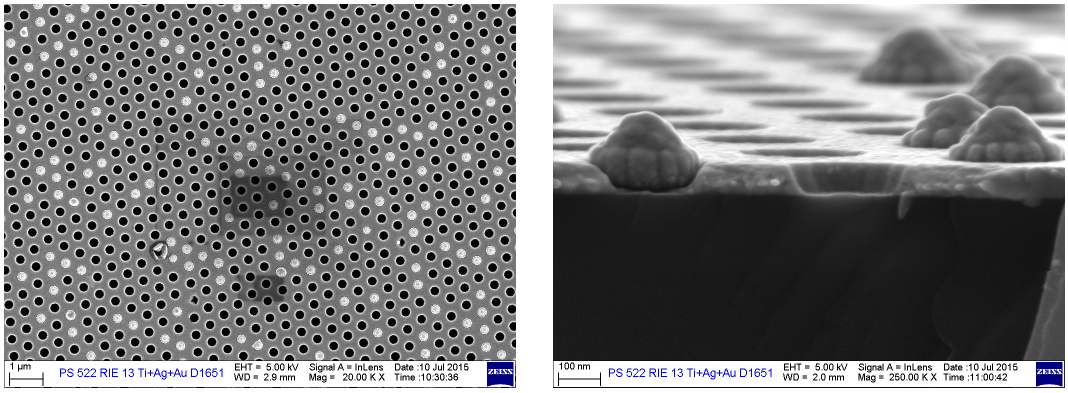

(a) **(b)**

Figure 5.10: (a) NHA with trapped PS nanosphere. 70 nm film was deposited on a 13 minutes RIE-etched mask. (b) Cross section image of the sample.

by a final NS removal by a toluene bath.

5.4.1 NHA spots for biosensing test

For biosensing purposes small spots of NHA should be functionalized, so the metal had to be deposited only on localized areas. Holes of diameter of 2 mm were drilled on small rectangular copper plates and these were used as masks for the selected-area deposition by placing them over the samples. Thereby the metal was deposited only on 2 mm diameter circular spots as can be observed in figure 5.11b.

Figure 5.11a shows a typical arrangement of the samples in a deposition run: the disposition of the substrates on the sample holder aproximatively follows the contour lines from figure 5.7b. The samples from 1 to 5 are PS nanosphere masks on SiO_2 and two metallic NHA spots were deposited on each one. The 6th substrate is a PS mask on Si, used for SEM measurements, and the 7th is a bare SiO_2 slab, used for film thickness and

film transmission measurements.

(a) Typical disposition of substrates during a sputtering run. In sequence, 5 nm of Ti, 45 nm of Ag and 10 nm of Au were deposited.

(b) Deposition of circular NHA spots.

First, transmission spectrum of the 60 nm film was measured, as reported in figure 5.8. Then film thickness was checked, and by AFM measurements of the 7th sample a 58.3 ± 1.2 nm height was found, confirming the sputtering map from figure 5.7b.

The NHA structures were morphologically characterized both by AFM and SEM microscopies. The NHA sample deposited on silicon substrate, was used for the SEM measurements, which allowed to evaluate both the diameter and the height of the holes. The figure 5.12a shows a top-view image of the NHA. The average hole diameter was then calculated using ImageJ software and it resulted 284 ± 5nm, in agreement with the average diameter of PS nanosphere of the 12 minutes etched mask. In figure 5.12b an in-plane view and cross-view of the NHA sample are presented. From the in-plane image, the thickness of metallic film can be evaluated and it resulted 63 ± 5 nm, in agreement with the positioning map for the sputtering.

EOT measurements From depositions NHA spots were available for biosensing tests. First, optical transmission spectra in $300 - 2500$nm range were acquired using a Jasco V-670 Spectrophotometer in order to observe the Extraordinary Optical Transmission (EOT) phenomenon. The EOT peak of each spot, corresponding to the <1,0> SPP Bloch-wave excitation, is observed in the NIR range. To define the position of a peak, its centroid can be used, that corresponds to the center of mass of the peak. The wavelength of the centroid of the EOT curve in such a spectrum is given by

$$\lambda_{centroid} = \frac{\sum_i \lambda_i (T_i - T_{th})}{\sum_i (T_i - T_{th})} \tag{5.2}$$

where T_i is the transmittance at the wavelength λ_i, T_{th} is a threshold value of transmittance chosen between the peak minimum and the maximum, and only λ_i such that $T_i > T_{th}$ are

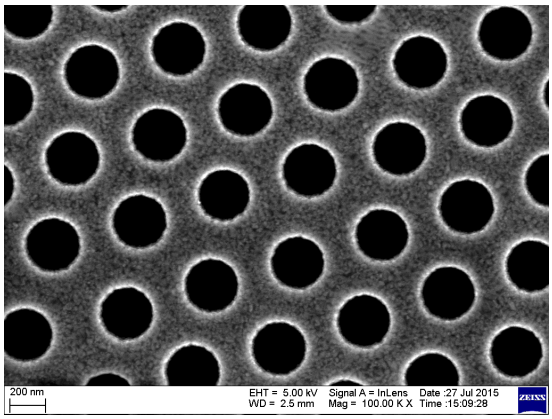

(a) Top-view SEM image. A $\mathbf{284 \pm 5}$ **nm** average diameter is measured.

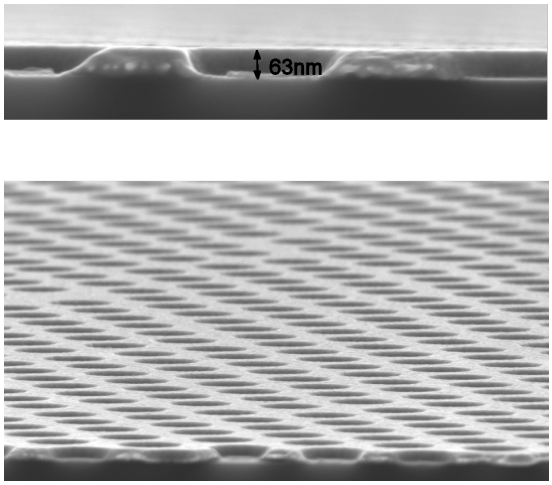

(b) In-plane view and cross-view SEM images.

Figure 5.12: SEM images of NHA sample on silicon substrate (n.6 in fig. 5.11a)

considered in the evaluation of $\lambda_{centroid}$. Centroids are measured in a range from 939 nm to 1031 nm and an average centroid at 977 nm is with a semidispersion of 46 nm is calculated. Similarly, wavelengths λ_{max} are measured in a range from 902 to 961 nm and a 926 mean with a 30 nm semidispersion is calculated.

Another tool to analyze the EOT peak relies on the Fano-type interpretation of the EOT phenomenon [60, 61]. The function from equation 5.3 can be used to fit the EOT peaks, where x_0 represents the wavelength position of the resonance peak. Both the centroid and the Fano-type fit were used and compared during the analyzis.

Figure 5.13 shows a normalized transmittance spectrum of a NHA measured by the spectrophotometer and also the fit with the Fano-type function from equation 5.3 is plotted.

$$y(x) = y_0 + A \cdot \frac{\left(q + \left(\frac{1}{x} - \frac{1}{x_0}\right) \cdot \sigma\right)^2}{\left(1 + \left(\frac{1}{x} - \frac{1}{x_0}\right) \cdot \sigma\right)^2} \tag{5.3}$$

Normalized transmittance tells how much light passes through the NHA with respect to the light that would pass through a single hole, in an opaque screen, with an area equivalent to the sum of all the single apertures. Therefore, the normalized transmission is calculated as the ratio of the measured one to the filling factor f of the NHA.

$$f = \frac{\text{Holes area}}{\text{NHA Area}} = \left(\frac{d}{a_0}\right)^2 \frac{2\pi}{\sqrt{3}} \approx 0.28 \tag{5.4}$$

where d is the hole diameter and a_0 is the periodicity of the array. It means that, neglecting plasmonic properties, 28% of the incident light would be transmitted. Dividing the transmittance spectrum by f, the plot from figure 5.13 is obtained. Transmittances above 100% can be observed and this stresses that an extraordinary transmission occurs through the NHA. Table 5.5 summarizes the characteristics of the EOT peaks and the fit parameters.

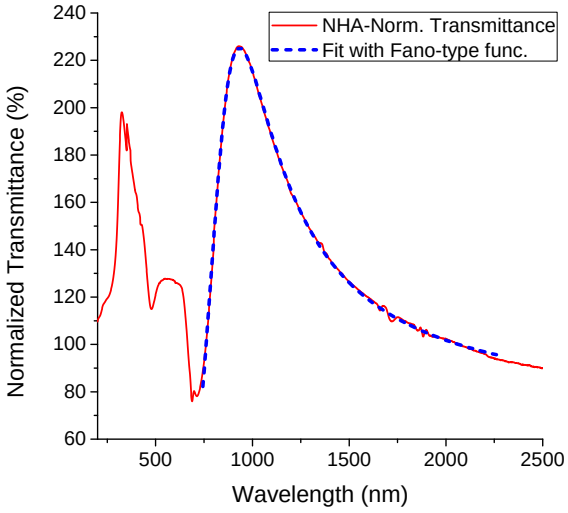

Figure 5.13: Normalized transmittance spectrum of a NHA. The fit with a Fano-type function is shown.

Avg. centroid	977 ± 46 nm
Avg. λ_{max}	926 ± 30 nm
y_0	2.2 ± 0.5
A	26.2 ± 0.2
q	-2.74 ± 0.01
x_0	855.7 ± 0.5
σ	3724 ± 6

Table 5.5: EOT peak characteristics.

5.4.2 Deposition of silica layer

Also large NHA samples were produced, without employing the copper plate mask. Such a NHA sample was then used for the local sensitivity test, presented in section 6.2.2. They were both characterized with AFM and SEM microscopies, and two images are presented in figure 5.14. Thus, the average diameter of the holes was measured from the SEM image and the thickness of the metallic film was measured using AFM images of both the NHA sample and a probing sample.

Hole diameter (nm)	Thickness$_{NHA}$	Thickness$_{Probe}$
326 ± 7 nm	62 ± 2 nm	65 ± 2 nm

For the local sensitivity tests, increasing silica layers were deposited up to a 36 nm thick one. In figure 5.15 the NHA with a 36 nm of silica layer deposited on is shown.

Two different detectors of the SEM microscope were used to acquire the image. On the left the secondary electrons image is presented while on the right there is the back-scattered electrons image. The first one is given by low-energy electrons that originate within few nanometers of the sample surface, so it reveals the presence of the silica layer. The second one consists of high-energy electrons which back-scatter when impinge on the metallic NHA, so this image does not reveal the presence of silica.

Analyzing such SEM images, internal diameter with and without the silica layer can be measured. The diameter of the hole with silica is measured to be 302 ± 7 nm while, neglecting the silica, a 327 ± 8 nm diameter is calculated. Thus, it is found that on the internal surface of the hole a 12.5 nm thick layer is deposited. This points out that deposition rate of the sputtering are different for vertical and horizontal directions and, in this case, the layer deposited on vertical surface was $\sim 1/3$ of the horizontal one.

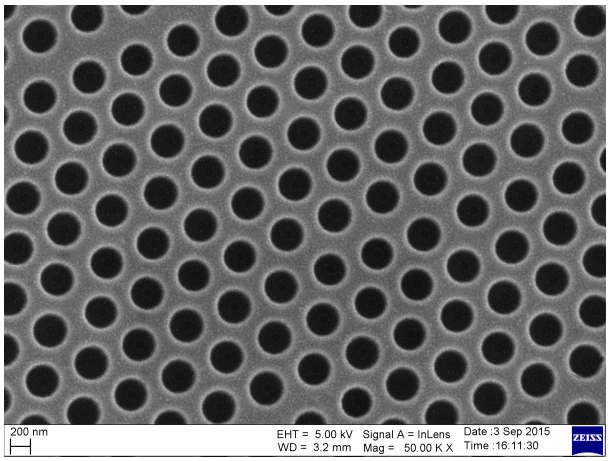

(a) SEM image. **326 ± 7 nm** average diameter was measured.

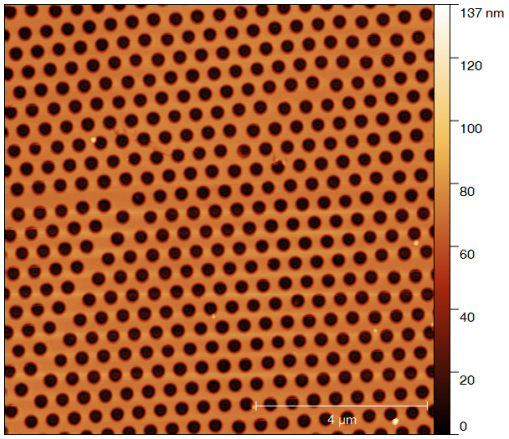

(b) AFM image. **62 ± 2 nm** height of the hole was measured.

Figure 5.14: A NHA used for silica deposition.

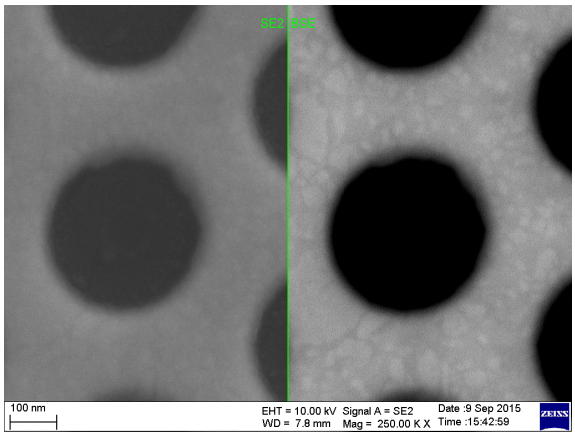

Figure 5.15: NHA + 36 nm SiO_2 layer. SEM image of the same hole with different detectors. The internal diameter is found to be 302 ± 7 nm

Chapter 6

Results: Biosensing tests

6.1 Functionalization protocol

In order to produce a biosensing device, bio-receptors that specifically bind with a selected analyte must be deposited on the metallic NHA spots. The functionalization protocols used in the present work to obtain a sensing interface are here described.

At first, the samples are incubated for 24 h in a thiols solution, 1 mM, of 1-Octanethiol (1-OCT):11-Mercaptoundecanoic acid (11-MUA) in 3:2 ratio in ethanol. Thus a protective monolayer of thiols over the nanohole array is self-assembled. Since a single thiol occupies an area of 0.214 nm^2 [62], the number of thiols that are expected to bind on the metallic interface of the NHA spot can be calculated considering the metallic surface. For a 2 mm diameter spot of NHA with the geometrical parameters described in the previous chapters the exposed metallic surface is of order of $3.44 \cdot 10^{12} nm^2$ so the expected overall number of the thiols is about $16 \cdot 10^{12}$ molecules.

Figure 6.1 shows the two thiols. Both have a terminating HS group that allows the thiols to covalently bind to the gold surface during the self-assembling of the thiolated monolayer. At the other end 11-MUA presents a -COOH group that allows it to bind with amino-terminated (bio)molecules. The end of the 1-OCT is inert to biological interactions and its role is to protect the NHA surface from aspecific bindings and to space 11-MUA thiols out. Samples are then rinsed with ethanol and dried by N_2 flow.

The second step is the coupling of the biomolecular receptor (Biotin-PEO_2-Amine) to the thiolated surface using a 1-Ethyl-3-[3- dimethylaminopropyl]carbodiimide hydrochloride (EDC) cross-linking agent. The EDC activates the carboxyl groups (-COOH) of 11-MUA to bind to the NH_2 groups of the Biotin-PEO_2-Amine, forming an amide bond

Figure 6.1: The two thiols employed in this work.

between the receptor and the thiols layer.

For this functionalization, a solution 1 mM of Biotin-PEO_2-Amine with 10 mM of EDC in 10 mM of phosphate buffered saline (PBS) was prepared. Droplets of a volume of $20\mu L$ were deposited on the thiolated NHA samples and after 3 hours they were rinsed with PBS 10 mM and water in order to remove unbound molecules. A $20\mu L$ volume of 1 mM Biotin solution contains about $1.2 \cdot 10^{16}$ molecules of the protein, orders of magnitude greater than the expected number of 11-MUA thiols on the NHA surface ($\sim 10^{12}$) and, therefore, all the 11-MUA thiols should link to one Biotin.

Finally, for the sensing test of binding events between receptor and analyte, solutions of Streptavidin (SA) at different concentrations ($10^{-15} - 10^{-5} M$) in PBS 10 mM were prepared. Droplets of 10 μL of each solution were deposited on different NHA spots. After 2 hours, samples were rinsed with PBS and water and dried by N_2 flow. To test the robustness of the NHA sensor, two additional sensing tests were done: a check-test using PBS solution and one using BSA protein solution to test the specificity, both of which should not produce any signal output.

1-Octanethiol, 11-Mercaptoundecanoic acid, ethanol, PBS, EDC, Streptavidin and BSA (Albumin from bovine serum) were purchased from Sigma Aldrich while, Biotin-PEO_2-Amine, was purchased from Thermo Scientific.

Functionalization steps are depicted in figure 6.2. At each step described above, optical transmission spectra of each sample were acquired and spectral shifts in wavelength domain were monitored as the output signal.

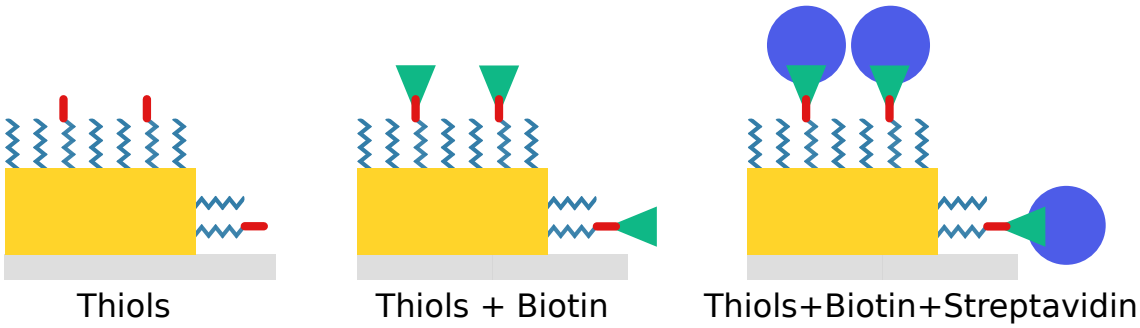

Figure 6.2: Functionalization steps of NHA

6.2 Sensitivity of the NHA

6.2.1 Bulk sensitivity

The sensitivity of the NHA, that is in this case how much EOT peak red-shifts as the refractive index changes at the interface, was firstly investigated. Specifically, the bulk sensitivity S_{bulk} was measured by depositing a thick layer of NOA-61 (thickness $\sim$ 1 mm, refractive index $n_{NOA} = 1.527$) and measuring the transmittance spectrum before and after the deposition. It is called bulk sensitivity because the thickness of the dielectric layer is

much greater than the decay length of the plasmonic electric field (1 mm vs. hundreds of nm). Thus, the plasmon excitation senses this as a change of all the dielectric medium above the NHA that is, indeed, a bulk variation.

The transmittance spectra before and after the deposition of the NOA layer are presented in figure 6.3 and results of the peak analysis are reported in table 6.1

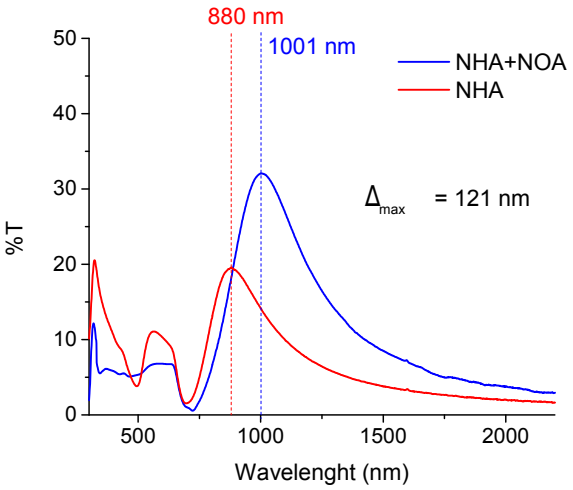

Figure 6.3: The NHA transmittance before and after the deposition of a thick NOA layer.

	NHA	NHA+NOA
Centroid(nm)	909	1033
FWHM(nm)	296	383
λ_{max}	880	1001
$\%T_{max}$	19.6	32.1
x_0 (nm)	839.4	978.1

Table 6.1: Peak analysis of NHA and NHA+NOA measurements.

Finally, bulk sensitivity S_{bulk} can be calculated as

$$S_{bulk}^{centroid} = \frac{\Delta\lambda_{centroid}}{n_{NOA} - n_{air}} = 235\,\text{nm} \cdot \text{RIU}^{-1}. \tag{6.1}$$

S_{bulk} can be also calculated using x_0 peak position from Fano-type fit and a better sensitivity is found

$$S_{bulk}^{x_0} = \frac{\Delta x_0}{n_{NOA} - n_{air}} = 262\,\text{nm} \cdot \text{RIU}^{-1}. \tag{6.2}$$

In section 4.3.1, the bulk sensitivity is evaluated by simulations and it resulted $252\,\text{nm} \cdot \text{RIU}^{-1}$, i.e., in good agreement with the experimental one.

6.2.2 Local sensitivity

Since the biorecognition event for small molecules involves the modification of a thin (∼few nm) layer at the NHA surface it is important to measure the local sensitivity of a NHA. It represents how much EOT peak shifts as the thickness of a dielectrical coating increases. While for the bulk sensitivity a large layer of NOA was deposited, for the local sensitivity thin layers of silica were deposited by magnetron sputtering. The master equation for defining the sensitivities is the equation describing the shift of EOT peak in response of changes in the refractive index on the surface of the NHA [63, 3]

$$\Delta\lambda_{peak}(d_a) = \lambda_{peak}(d_a) - \lambda_{peak}(0) = S_{bulk}\Delta n \left[1 - \exp\left(-\frac{2d_a}{l_d}\right)\right]. \tag{6.3}$$

$\Delta\lambda_{peak}(d_a)$ is the shift of the EOT peak when a d_a thick layer of analyte is deposited over the NHA surface. S_{bulk} is the bulk sensitivity, $\Delta n = n_a - n_e$ is the refractive index change with n_a and n_e the refractive index of, respectively, the analyte and the environment (i.e., air with $n_e = 1$) and l_d is the effective decay length of the local field (i.e., from eq. 4.1 $\sim 55\,\text{nm}$). The definition of the bulk sensitivity from equation 6.1 is obtained in the limit $d_a \gg l_d$ where

$$\Delta\lambda_{peak}(\infty) = S_{bulk}\Delta n. \tag{6.4}$$

On the other hand, the local sensitivity S_0 is defined by

$$S_0 \equiv \frac{1}{\Delta n}\left.\frac{\partial\lambda_{peak}}{\partial d_a}\right|_{d_a=0} \tag{6.5}$$

In the limit of $d_a < l_d$, exponential may be approximated with a first-order series and, thus, a linear function is obtained.

$$\lambda_{peak}(d_a) \approx \lambda_{peak}(0) + S_{bulk}\Delta n\left[1 - \left(1 - \frac{2d_a}{l_d}\right)\right] = \lambda_{peak}(0) + \left(\frac{2S_{bulk}\Delta n}{l_d}\right)\cdot d_a \tag{6.6}$$

Therefore, in order to evaluate the local sensitivity, layers of silica with thickness lower than l_d were deposited so the linear approximation could be used. For these measurements, three depositions of silica were done in sequence on a NHA sample, and transmittance spectra of two specific areas (called top and bottom areas) were acquired after each deposition. The total thickness at each step was measured by AFM microscopy using probe samples of silicon during the depositions. Therefore, the transmittance of NHA with an incremental silica layer of 0, 13, 24 and 36 nm thicknesses were measured and are presented in figure 6.4. The EOT peaks analysis is reported in table 6.2 and then the centroid positions are plotted against the thickness of the silica layers in figure 6.5.

It can be observed that the transmittance at the λ_{max} increases as thicker silica layers are deposited and it is due to the fact that a better plasmonic coupling occurs when there is the same dielectric medium at the two interfaces of the NHA.

	bottom-measurements				top-measurements			
t	Centroid	FWMH	λ_{max}	x_0	Centroid	FWMH	λ_{max}	x_0
(nm)	(nm)	(nm)	(nm)	(nm)	(nm)	(nm)	(nm)	(nm)
0	1021	499	965	909 ± 1	1017	495	966	903 ± 1
13	1030	502	978	926 ± 1	1030	501	975	924 ± 1
24	1047	518	990	948 ± 1	1042	508	993	944 ± 1
36	1060	527	1004	968 ± 1	1056	522	1002	965 ± 1

Table 6.2: EOT peak analysis for increasing silica layer coating.

Since the thicknesses of silica layers are smaller that the decay length of the local field l_d, the approximation from eq. 6.6 can be used. A linear function $y = m \cdot x + q$ is then used to fit the data and, thus, from eq. 6.5 the local sensitivity S_0 can be calculated using

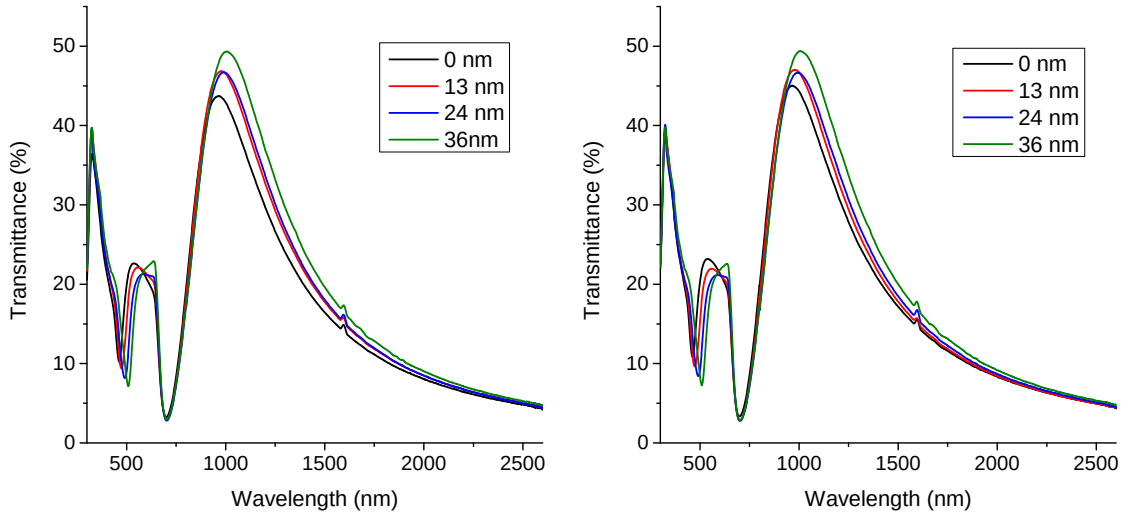

(a) Peak shifts for top measurements.

(b) Peak shifts for bottom measurements.

Figure 6.4: EOT peak shifts due to increasing silica layer deposition.

the slopes m reported in table 6.3 as

$$S_0 = \frac{m}{n_{SiO_2} - n_{air}}. \tag{6.7}$$

The sensitivity for each area and a weighted mean are calculated for both centroid and Fano-type analysis, and are presented in table 6.4.

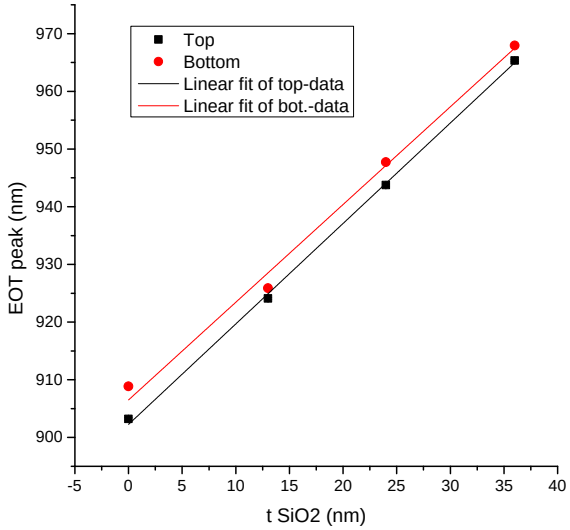

Figure 6.5: Linear fit of EOT peak shifts against silica layer thickness.

	Intercept q (nm)	Slope m
From Fano-type analyzis		
top	902 ± 1	1.74 ± 0.04
bot.	907 ± 2	1.69 ± 0.09
From centroid analyzis		
top	1017 ± 1	1.08 ± 0.03
bot.	1019 ± 3	1.12 ± 0.11

Table 6.3: Linear fit results for the local sensitivity.

6.3 Biosensing test

For the biosensing tests, NHA spots were used and transmittance spectra were measured at each step of the functionalization protocol in order to monitor the position of the EOT

Analysis	Top-area	Bottom-area	Weighted mean
Centroids	2.40 ± 0.07 RIU^{-1}	2.49 ± 0.24 RIU^{-1}	2.41 ± 0.08 RIU^{-1}
Fano x_0	3.87 ± 0.08 RIU^{-1}	3.76 ± 0.23 RIU^{-1}	3.82 ± 0.11 RIU^{-1}

Table 6.4: Local sensitivities results.

peaks. Since functionalization with thiols and biotin is identical for all the samples, similar EOT peak shifts should be observed between bare NHA and thiolated NHA and between thiolated NHA and biotin functionalized NHA. The subsequent analysis of the EOT peaks was done by both centroid method and Fano-type fit.

Hereafter droplets (volume $5\mu L$) with different concentrations of the streptavidin analyte were deposited over the NHA. Concentrations in a range of $10^{-15}M - 1.67 \cdot 10^{-5}$ were used and the same concentration was deposited on multiple functionalized NHA samples. Also tests with blank solution, i.e. without analyte molecules, were done and considered as very low concentration data, i.e. $10^{-15}M$. The EOT peak analysis is summarized in table 6.7 where a 1.5 nm error considered for each measurement, and these shifts represent the signal output in response to the sensing events.

Figure 6.6 presents the transmittance spectra of a sample at each step and it points out how EOT peak shift during the functionalization. On this sample a $5{\cdot}10^{-7}$ M concentration is used for biosensing test. In the table 6.5

	x_0 (nm)	Centroid (nm)
as deposited	875	1047
NHA+thiols	885	1054
NHA+thiols+Biotin	903	1060
NHA+thiols+Biotin+Strept. $5 \cdot 10^{-7}$ M	925	1075

Table 6.5: Peak analysis of transmittance at each step of the protocol.

The two data sets of shifts from table 6.7 are presented in log-scaled graphics in figure 6.7 as a function of the streptavidin concentration [SA]. The data have been then fitted with the model of Langmuir isotherm [64] from equation 6.8

$$\Delta\lambda_{peak} = \frac{\Delta\lambda_{sat} \cdot K_{a_{eff}} \cdot [SA]}{1 + K_{a_{eff}} \cdot [SA]} \tag{6.8}$$

where $\Delta\lambda_{sat}$ is the saturation value of $\Delta\lambda_{peak}$, that is the maximum output signal that NHA sensor could produce, and $K_{a_{eff}}$ is the effective affinity constant. This curve is valid if a 1:1 binding of the Streptavidin to the surface-bound biotin is supposed and it is widely used to describe the adsorption process of an analyte. A high value of $K_{a_{eff}}$ stresses the high affinity between streptavidin and biotin, so their binding reaction is essentially irreversible. In figure 6.7 also fitted curves are presented, and its parameters are reported in table 6.6.

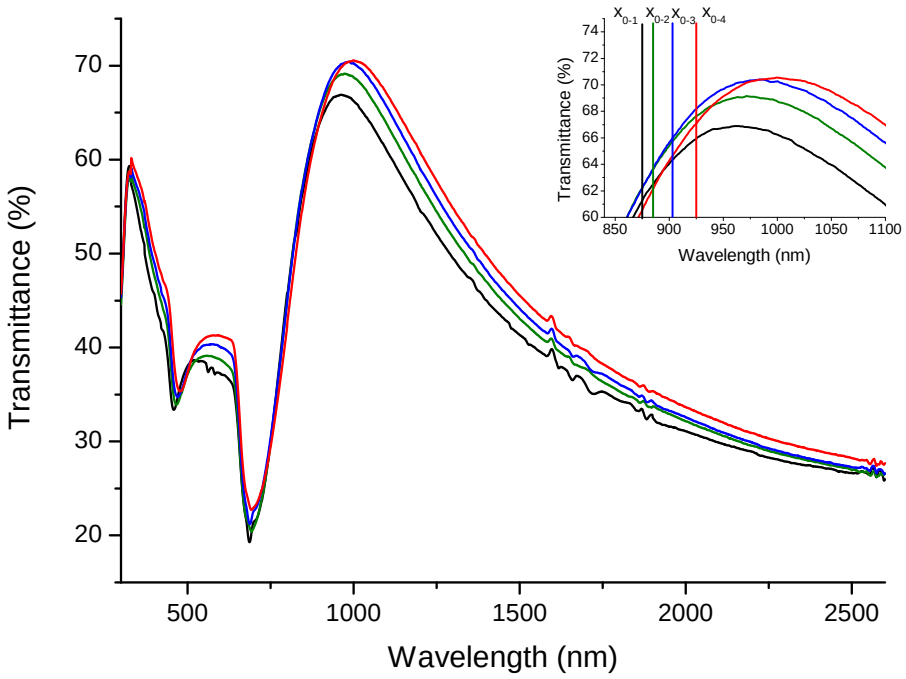

Figure 6.6: Transmittance spectrum of the NHA after each step of the functionalization protocol: NHA as dep. (black line), NHA functionalized with thiols (green), NHA functionalized with thiols and Biotin (blue), NHA after exposition to $5 \cdot 10^{-7}$ M of Streptavidin (red). Inset: Magnification of the maximum region. Besides the curves, also the centroid parameters from the Fano fit (x_0) are indicated for each step.

	Centroid analysis	Fano-peak analysis
$\Delta\lambda_{sat}$ (nm)	17 ± 2	25 ± 3
$K_{a_{eff}}$ (M^{-1})	$(5.7 \pm 3.4) \cdot 10^6$	$(9.1 \pm 6.0) \cdot 10^6$

Table 6.6: Langmuir isotherm fit for the sensing curves

To check the specificity of such a biosensor, another test was done using, instead of the streptavidin, an analyte solution with Bovine Serum Albumin (BSA) globular protein which has similar structure and molecular weight. A solution $1.67 \cdot 10^{-7}$ M of BSA in 10mM PBS was dropped on the Biotin-functionalized NHA. The transmittance spectra were acquired, and no signal output should be observed since binding events should not occur between Biotin and BSA. A negligible signal output is obtained, as the reported the peak shifts were, respectively, 2.4 ± 0.5 nm from the Fano-analisys and 2.5 ± 1.5 from the centroid method.

In order to increase specificity, during functionalization protocol, Amine-PEG11-Biotin might be used instead of Amine-PEG2-Biotin. The first one, due to its larger length (11 PEG vs 2 PEG molecules), could better protect the NHA surface from aspecific binding events.

Concentration [SA] (M)	x_0 shift $\Delta\lambda_{peak}$ (nm)	Centroid shift $\Delta\lambda_{peak}$ (nm)
1.00E-15	-1.4 ± 1.5	0.3 ± 1.5
1.00E-10	-0.3 ± 1.5	4.4 ± 1.5
1.00E-09	3.9 ± 1.5	0.3 ± 1.5
2.00E-09	3.3 ± 1.5	0.5 ± 1.5
1.00E-08	4.5 ± 1.5	2.3 ± 1.5
1.00E-07	10.0 ± 1.5	6.6 ± 1.5
2.00E-07	7.4 ± 1.5	3.8 ± 1.5
5.00E-07	28.4 ± 1.5	16.5 ± 1.5
1.00E-06	20.9 ± 1.5	13.9 ± 1.5
2.00E-06	31.7 ± 1.5	20.0 ± 1.5
1.00E-05	17.2 ± 1.5	12.4 ± 1.5
1.67E-05	21.9 ± 1.5	15.4 ± 1.5

Table 6.7: EOT peak shifts in presence of different concentrations of analyte.

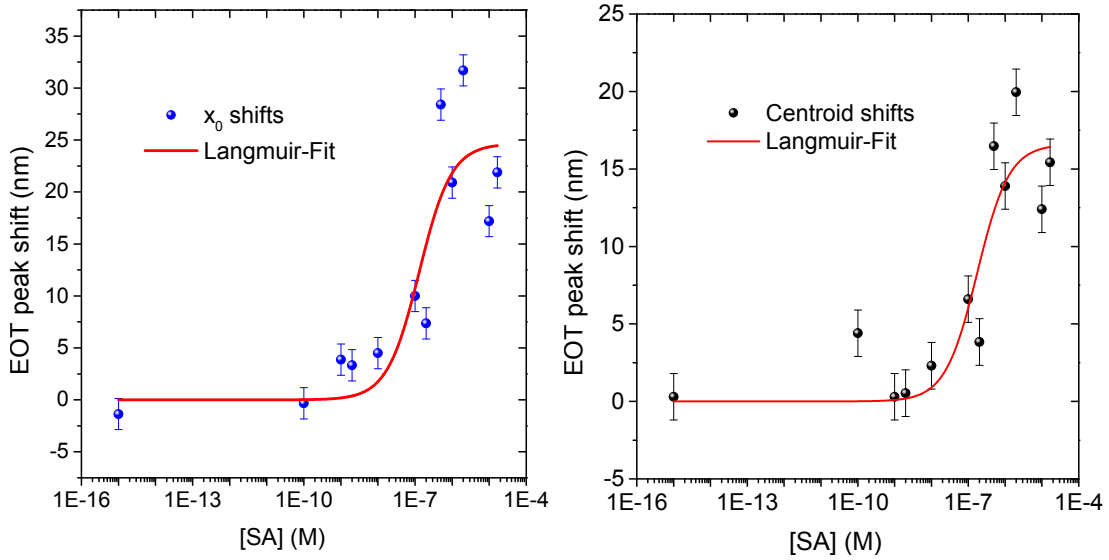

(a) Sensing curve from Fano-type resonance shifts

(b) Sensing curve from centroid method.

Figure 6.7: Sensing curves with Langmuir Isotherm fit.

Chapter 7

Conclusions

In this work an efficient protocol for the production of plasmonic Nano-Hole Arrays samples was presented and optimized. It has been shown that Nano Sphere Litography represents a powerful and reliable technique to produce well-ordered and cost-effective nanohole arrays with high throughput, by employing monolayers of polystyrene nanospheres as deposition masks. Moreover, this technique allowed to finely tune the morphology of NHA by varying technical parameters during the production process.

Optical properties of the synthesized NHA were investigated by measuring transmittance spectra of normally-incident light on the NHA surface and the extraordinary optical transmission, when plasmonic resonance occurs, was demonstrated.

Due to its plasmonic properties, the use of NHA as a transducer for a biosensing devices was investigated. Since the plasmonic resonace condition varies as the refractive index at the NHA surface changes, the NHA behaves as an optical transducer for the binding of an analyte with a receptor, previously immobilized on the NHA surface, as a wavelength red-shift of the transmission peak. To discriminate when a peak shift occurs, two different methods of analysis of an EOT peak were presented and compared, the centroid method and the Fano-type fit.

Bulk and local sensitivities of the NHA-based sensor were evaluated both experimentally and by numerical simulations and the simulated sensitivities were in good agreement with the experimental ones, which resulted similar to the ones reported in literature:

$$S_{bulk} = 262 \pm 5 \text{ nm/RIU} \qquad S_0 = 3.8 \pm 0.1 \text{ RIU}^{-1}$$

Better sensivities were obtained using the resonance wavelength from the Fano-type fit with respect to the centroid method, so Fano-type fit was chosen as the main analysis method.

Finally last, the ability to reveal the binding events between biotin, as receptor, and streptavidin, as analyte, using solution with different concentration of streptavidin was measured. Monitoring the shifts which occur at different analyte concentrations, the sensing curves of wavelength shifts as a function of the concentration were obtained. In order to test the robustness of such biosensor, a specificity test was done by using BSA protein

for which no signal output was expected. Since a small shift is observed with BSA and since the sensing curve points present a certain degree of noise, we inferred that aspecific binding occurs despite the PEGylated protection coating.

Residual polystyrene-related traces were observed by AFM microscopy on the bottom of the hole, after the mask removal, which might be responsable for the aspecific binding since they are not PEG-protected. Further tests will be done to remove the residual polystyrene using a more aggresive cleaning proces such as a further RIE process or a bath in warm toluene after metal deposition and mask removal.

Another way to prevent aspecific binding it will be to replace the Amine-PEG_2-Biotin, used to functionalize the NHA, with the Amine-PEG11-Biotin which is a larger molecule and could protect better the NHA surface providing a better anti-fouling effect.

Despite aspecificity issues, it was demonstrated that NHA represents a powerful and high-sensitivity label-free transducer for biosensing applications, and, due its long decay length of the near-field plasmonic excitation, it can be employed to reveal the presence of large molecules or bacteria.

Bibliography

[1] Masud Mansuripur. The role of nanotechnology in data storage devices and systems. In *Nonlinear Optics*, page OMA2. Optical Society of America, 2011.

[2] Surbhi Lal, Stephan Link, and Naomi J. Halas. Nano-optics from sensing to waveguiding. *Nature Photonics*, 1(11):641–648, nov 2007.

[3] J.N. Anker, W.P. Hall, O. Lyandres, N.C. Shah, J. Zhao, and R.P. Van Duyne. Biosensing with plasmonic nanosensors. *Nature materials*, 7(6):442–453, 2008.

[4] J M Pitarke, V M Silkin, E V Chulkov, and P M Echenique. Theory of surface plasmons and surface-plasmon polaritons. *Reports on Progress in Physics*, 70(1):1, 2007.

[5] T. W. Ebbesen, H. J. Lezec, H. F. Ghaemi, T. Thio, and P. A. Wolff. *Nature*, 391(6668):667–669, feb 1998.

[6] John C. Hulteen. Nanosphere lithography: A materials general fabrication process for periodic particle array surfaces. *Journal of Vacuum Science & Technology A: Vacuum, Surfaces, and Films*, 13(3):1553, may 1995.

[7] Carlos Escobedo. On-chip nanohole array based sensing: a review. *Lab on a Chip*, 13(13):2445, 2013.

[8] P.B. Johnson and R.W. Christy. Optical constants of the noble metals. *Phys. Rev. B*, 6(12):4370–4379, 1972.

[9] T. Kashiwa and I. Fukai. A treatment by the FD-TD method of the dispersive characteristics associated with electronic polarization. *Microwave and Optical Technology Letters*, 3(6):203–205, 1990.

[10] Alexandre Vial, Anne-Sophie Grimault, Demetrio Macías, Dominique Barchiesi, and Marc Lamy de la Chapelle. Improved analytical fit of gold dispersion: Application to the modeling of extinction spectra with a finite-difference time-domain method. *Phys. Rev. B*, 71:085416, Feb 2005.

[11] F. Hao and P. Nordlander. Efficient dielectric function for FDTD simulation of the optical properties of silver and gold nanoparticles. *Chemical Physics Letters*, 446:115–118, September 2007.

[12] Gustav Mie. Beiträge zur optik trüber medien, speziell kolloidaler metallösungen. *Ann. Phys.*, 330(3):377–445, 1908.

[13] E. Gazzola, L. Brigo, G. Zacco, P. Zilio, G. Ruffato, G. Brusatin, and F. Romanato. Coupled spp modes on 1d plasmonic gratings in conical mounting. *Plasmonics*, 9(4):867–876, 2014.

[14] Filippo Romanato, Lee Kwang Hong, Husen Kartasasmita Kang, Chee Cheong Wong, Zong Yun, and Wolfgang Knoll. Azimuthal dispersion and energy mode condensation of grating-coupled surface plasmon polaritons. *Phys. Rev. B*, 77:245435, Jun 2008.

[15] H. A. Bethe. Theory of diffraction by small holes. *Phys. Rev.*, 66:163–182, Oct 1944.

[16] F. J. Garcia-Vidal, T. W. Ebbesen, and L. Kuipers. Light passing through subwavelength apertures. *Rev. Mod. Phys.*, 82(1):729–787, March 2010.

[17] Shih-Hui Chang, Stephen Gray, and George Schatz. Surface plasmon generation and light transmission by isolated nanoholes and arrays of nanoholes in thin metal films. *Opt. Express*, 13(8):3150–3165, April 2005.

[18] H. F. Ghaemi, Tineke Thio, D. E. Grupp, T. W. Ebbesen, and H. J. Lezec. Surface plasmons enhance optical transmission through subwavelength holes. *Phys. Rev. B*, 58(11):6779–6782, September 1998.

[19] C. Genet and T. W. Ebbesen. Light in tiny holes. *Nature*, 445(7123):39–46, jan 2007.

[20] Hua Cao and Ajay Nahata. Influence of aperture shape on the transmission properties of a periodic array of subwavelength apertures. *Opt. Express*, 12(16):3664–3672, 2004.

[21] A Degiron and T W Ebbesen. The role of localized surface plasmon modes in the enhanced transmission of periodic subwavelength apertures. *Journal of Optics A: Pure and Applied Optics*, 7(2):S90–S96, jan 2005.

[22] G. M. Wallraff and W. D. Hinsberg. Lithographic imaging techniques for the formation of nanoscopic features. *Chemical Reviews*, 99(7):1801–1822, jul 1999.

[23] Takashi Ito and Shinji Okazaki. *Nature*, 406(6799):1027–1031, aug 2000.

[24] Henry I. Smith and M. L. Schattenburg. X-ray lithography, from 500 to 30 nm: X-ray nanolithography. *IBM J. Res. Dev.*, 37(3):319–329, May 1993.

[25] H. W. Deckman. Natural lithography. *Appl. Phys. Lett.*, 41(4):377, 1982.

[26] C. L. Haynes and R. P. Van Duyne. Nanosphere lithography: A versatile nanofabrication tool for studies of Size-Dependent nanoparticle optics. *The Journal of Physical Chemistry B*, 105(24):5599–5611, June 2001.

[27] J. Rybczynski, U. Ebels, and M. Giersig. Large-scale, 2D arrays of magnetic nanoparticles. *Colloids and Surfaces A: Physicochemical and Engineering Aspects*, 219(1-3):1–6, 2003.

[28] Günter Schatz. Self-assembled nanospheres : An exciting playground. *Acta Physica Polonica A*, 115(2):431–434, 2009.

[29] Stephen M. Rossnagel, William D. Westwood, and Jerome J. Cuomo. *Handbook of Plasma Processing Technology: Fundamental, Etching, Deposition and Surface Interactions (Materials Science and Process Technology)*. William Andrew, 1991.

[30] Peng Zheng, Scott K. Cushing, Savan Suri, and Nianqiang Wu. Tailoring plasmonic properties of gold nanohole arrays for surface-enhanced raman scattering. *Phys. Chem. Chem. Phys.*, 17(33):21211–21219, 2015.

[31] Si Hoon Lee, Kyle C. Bantz, Nathan C. Lindquist, Sang-Hyun Oh, and Christy L. Haynes. Self-assembled plasmonic nanohole arrays. *Langmuir*, 25(23):13685–13693, dec 2009.

[32] D. M. Mattox. *Handbook of physical vapor deposition (PVD) processing*. William Andrew Elsevier Science distributor, Norwich, N.Y. Oxford, 2010.

[33] Danilo Rossi. *Sensori per misure biomediche*. Pa'tron, Bologna, 2004.

[34] Ricardo F. Aroca. Plasmon enhanced spectroscopy. *Phys. Chem. Chem. Phys.*, 15:5355–5363, 2013.

[35] Heather K. Hunt and Andrea M. Armani. Label-free biological and chemical sensors. *Nanoscale*, 2(9):1544, 2010.

[36] Bo Liedberg, Claes Nylander, and Ingemar Lunström. Surface plasmon resonance for gas detection and biosensing. *Sensors and Actuators*, 4:299–304, jan 1983.

[37] Jirí Homola. Surface plasmon resonance sensors for detection of chemical and biological species. *Chemical Reviews*, 108, 2008.

[38] Jiří Homola. *Surface plasmon resonance based sensors*. Springer, Berlin New York, 2006.

[39] Edy Wijaya, Cédric Lenaerts, Sophie Maricot, Juriy Hastanin, Serge Habraken, Jean-Pierre Vilcot, Rabah Boukherroub, and Sabine Szunerits. Surface plasmon resonance-based biosensors: From the development of different SPR structures to novel surface functionalization strategies. *Current Opinion in Solid State and Materials Science*, 15(5):208–224, oct 2011.

[40] Hoang Nguyen, Jeho Park, Sebyung Kang, and Moonil Kim. Surface plasmon resonance: A versatile technique for biosensor applications. *Sensors*, 15(5):10481–10510, may 2015.

[41] www.biacore.com. *Biacore T100 Instrument Handbook*. 2005.

[42] Marek Piliarik and Jiří Homola. Surface plasmon resonance (SPR) sensors: approaching their limits? *Opt. Express*, 17(19):16505, 2009.

[43] Jose Melendez, Richard Carr, Dwight U Bartholomew, Kari Kukanskis, Jerry Elkind, Sinclair Yee, Clement Furlong, and Rick Woodbury. A commercial solution for surface plasmon sensing. *Sensors and Actuators B: Chemical*, 35(1-3):212–216, sep 1996.

[44] Alexei N. Naimushin, Scott D. Soelberg, Dwight U. Bartholomew, Jerry L. Elkind, and Clement E. Furlong. A portable surface plasmon resonance (spr) sensor system with temperature regulation. *Sensors and Actuators B: Chemical*, 96(12):253 – 260, 2003.

[45] Andreas B. Dahlin. Sensing applications based on plasmonic nanopores: The hole story. *Analyst*, 140:4748–4759, 2015.

[46] Reuven Gordon, David Sinton, Karen L. Kavanagh, and Alexandre G. Brolo. A new generation of sensors based on extraordinary optical transmission. *Accounts of Chemical Research*, 41(8):1049–1057, 2008. PMID: 18605739.

[47] Alexandre G. Brolo, Reuven Gordon, Brian Leathem, and Karen L. Kavanagh. Surface plasmon sensor based on the enhanced light transmission through arrays of nanoholes in gold films. *Langmuir*, 20(12):4813–4815, jun 2004.

[48] Angela De Leebeeck, L. K. Swaroop Kumar, Victoria de Lange, David Sinton, Reuven Gordon, and Alexandre G. Brolo. On-chip surface-based detection with nanohole arrays. *Analytical Chemistry*, 79(11):4094–4100, jun 2007.

[49] Sang-Yeon Cho, J.L. Briscoe, I.A. Hansen, J.K. Smith, Yoomi Chang, and I. Brener. Label-free plasmonic immunosensing for plasmodium in a whole blood lysate. *Sensors Journal, IEEE*, 14(5):1399–1404, May 2014.

[50] Yen-Liang Yeh, Cheng. Chi. Wang, Ming-Jyi Jang, Chia-Hsun Chen, Shih-Ming Tzeng, Yen-Pin Lin, and Kuang. Sheng Chen. Real-time measurement of glucose concentration using position sensing detector. 2008.

[51] Jayson L. Briscoe, Sang-Yeon Cho, and Igal Brener. Part-per-trillion level detection of microcystin-LR using a periodic nanostructure. *IEEE Sensors J.*, 15(3):1366–1371, mar 2015.

[52] Sonia Herranz, Markéta Bocková, María Dolores Marazuela, Jiří Homola, and María Cruz Moreno-Bondi. An SPR biosensor for the detection of microcystins in drinking water. *Anal Bioanal Chem*, 398(6):2625–2634, jun 2010.

[53] Ahmet Ali Yanik, Min Huang, Alp Artar, Tsung-Yao Chang, and Hatice Altug. Integrated nanoplasmonic-nanofluidic biosensors with targeted delivery of analytes. *Appl. Phys. Lett.*, 96(2):021101, 2010.

[54] Fatemeh Eftekhari, Carlos Escobedo, Jacqueline Ferreira, Xiaobo Duan, Emerson M. Girotto, Alexandre G. Brolo, Reuven Gordon, and David Sinton. Nanoholes as nanochannels: Flow-through plasmonic sensing. *Analytical Chemistry*, 81(11):4308–4311, jun 2009.

[55] Chanda Ranjit Yonzon, Douglas A. Stuart, Xiaoyu Zhang, Adam D. McFarland, Christy L. Haynes, and Richard P. Van Duyne. Towards advanced chemical and biological nanosensorsan overview. *Talanta*, 67(3):438 – 448, 2005. Nanoscience and Nanotechnology.

[56] Alexandre G. Brolo Erin Arctander Reuven Gordon Brian Leathem and Karen L. Kavanagh. Nanohole-enhanced raman scattering. *Nano Letters*, 4(10):2015–2018, 2004.

[57] Bhavya Sharma, Renee R. Frontiera, Anne-Isabelle Henry, Emilie Ringe, and Richard P. Van Duyne. Sers: Materials, applications, and the future. *Materials Today*, 15(12):16 – 25, 2012.

[58] Anna Meneghello, Agnese Antognoli, Agnese Sonato, Gabriele Zacco, Gianluca Ruffato, Erica Cretaio, and Filippo Romanato. Label-free efficient and accurate detection of cystic fibrosis causing mutations using an azimuthally rotated gc-spr platform. *Analytical Chemistry*, 86(23):11773–11781, 2014. PMID: 25359284.

[59] M. Perino, E. Pasqualotto, A. De Toni, D. Garoli, M. Scaramuzza, P. Zilio, T. Ongarello, A. Paccagnella, and F. Romanato. Development of a complete plasmonic grating-based sensor and its application for self-assembled monolayer detection. *Appl. Opt.*, 53(26):5969–5976, Sep 2014.

[60] Michaël Sarrazin, Jean-Pol Vigneron, and Jean-Marie Vigoureux. Role of wood anomalies in optical properties of thin metallic films with a bidimensional array of subwavelength holes. *Phys. Rev. B*, 67:085415, Feb 2003.

[61] C Genet, M.P van Exter, and J.P Woerdman. Fano-type interpretation of red shifts and red tails in hole array transmission spectra. *Optics Communications*, 225(4-6):331–336, oct 2003.

[62] Michael J. Hostetler, Julia E. Wingate, Chuan-Jian Zhong, Jay E. Harris, Richard W. Vachet, Michael R. Clark, J. David Londono, Stephen J. Green, Jennifer J. Stokes, George D. Wignall, Gary L. Glish, Marc D. Porter, Neal D. Evans, and Royce W. Murray. Alkanethiolate gold cluster molecules with core diameters from 1.5 to 5.2 nm: core and monolayer properties as a function of core size. *Langmuir*, 14(1):17–30, jan 1998.

[63] Niccolò Michieli, Boris Kalinic, Carlo Scian, Tiziana Cesca, and Giovanni Mattei. Optimal geometric parameters of ordered arrays of nanoprisms for enhanced sensitivity

in localized plasmon based sensors. *Biosensors and Bioelectronics*, 65:346–353, mar 2015.

[64] Amanda J. Haes, , and Richard P. Van Duyne*. A nanoscale optical biosensor:? sensitivity and selectivity of an approach based on the localized surface plasmon resonance spectroscopy of triangular silver nanoparticles. *Journal of the American Chemical Society*, 124(35):10596–10604, 2002. PMID: 12197762.

List of Figures

List of Tables